This work is protected by copyright and other intellectual property rights and duplication or sale of all or part is not permitted, except that material may be duplicated by you for research, private study, criticism/review or educational purposes. Electronic or print copies are for your own personal, non-commercial use and shall not be passed to any other individual. No quotation may be published without proper acknowledgement. For any other use, or to quote extensively from the work, permission must be obtained from the copyright holder/s.

The thermo-acoustic Fant equation

Patrick R. Murray

Submitted in partial fulfillment of the requirements of the degree of

Doctor of Philosophy in Applied Mathematics

School of Computing and Mathematics

Keele University

June 2012

Abstract

A theoretical analysis is made of combustion instabilities of three combustor configurations. The equations governing aeroacoustics and combustion are derived, arriving at an acoustic analogy in terms of the pressure and total enthalpy. A solution for the acoustic analogy is determined in terms of a Green's function and initial instability results are presented for the pressure Green's function. These predictions are limited by assumptions made about the combustion zone. Finally a 'reduced complexity' equation is derived accounting for a generalised combustion zone. The equation is nonlinear and furnishes limit cycle solutions for finite amplitude burner modes. It is a generalisation to combustion flows of the Fant equation used to investigate the production of voiced speech (G Fant. *Acoustic Theory of Speech Production.* Mouton, The Hague, 1960). The Fant equation governs the unsteady volume flow past the flame holder which, in turn, determines the acoustics of the entire system. The equation includes a fully determinate part that depends on the geometry of the flame-holder and the thermo-acoustic system, and terms defined by integrals involving thermo-aerodynamic sources, such as the flame and vortex sound sources. Illustrative numerical results are presented for both the linearised equation and the full nonlinear equation. The linearised equation governs the growth rate of the natural acoustic modes, which are excited into instability by unsteady heat release from the flame and damped by large scale vorticity production and radiation losses. The full nonlinear equation, however, governs the 'limit cycle' formation when absorption of sound by vortex shedding at trailing edges equally opposes sound generation by the flame. Limit cycle modes are of particular interest because they cannot be captured in linear predictions and are the primary source of combustor instabilities.

Contents

1 Introduction **1**

2 Aeroacoustics and thermal sources **6**

2.1 The equations of fluid dynamics 6

2.1.1 The continuity equation 7

2.1.2 The momentum equation 7

2.1.3 The energy equation 10

2.1.4 Vorticity and Crocco's momentum equation 10

2.2 Lighthill's acoustic analogy 11

2.2.1 Equations of linear acoustics 12

2.2.2 Lighthill's equations 14

2.2.3 Monopoles, dipoles, and quadrupoles 17

2.3 Thermal sources 18

2.3.1 Combustion models 22

3 Models of a generic combustor **24**

3.1 The Limousine combustor 25

3.2 The idealised duct combustor 27

4 The Green's function **29**

4.1 The pressure Green's function 30

4.1.1 Eigenfrequencies 31

4.1.2 Green's function modal amplitudes 33

4.1.3 Burner stability 37

4.2 The total enthalpy Green's function 40

5 The burner blockage length **42**

5.1 The blockage integral 43

5.2 The blockage length by solution to Laplace's equation 44

5.2.1 Finite-difference methods 45

5.3 The effect of splitter plates 48

5.4 The Schwarz-Christoffel transformation 52

5.4.1 An example with one unknown 54

5.5 The blockage length by transformation 55

5.5.1 Gauss-Jacobi quadrature 57

5.5.2 Minimising the error 59

5.5.3 Streamlines of a hydrodynamic source flow 60

5.5.4 Arbitrary source locations 62

5.6 The blockage length for the idealised combustor 71

6 The thermo-acoustic Fant equation **74**

6.1 The direct method 76

6.2 The adjoint-equation method 83

7 Application of the linear Fant equation **87**

7.1 The effect of mean flow 89

7.2 The effect of unsteady heat release 90

8 Application of the nonlinear Fant equation **97**

8.1 The nonlinear heat source 97

8.2 The solution of the nonlinear thermo-acoustic Fant equation 100

9 Application to the Limousine burner **115**

9.1 The modified Green's function 116

9.2 The modified Fant equation 118

9.3 Thermo-acoustic Fant equation predictions for the Limousine burner 121

10 Conclusion **126**

References **128**

List of Figures

3.1 Schematic section of the first Limousine combustor Configuration I. 26

3.2 Schematic secction of the second Limousine combustor Configuration II. 27

3.3 Schematic section of the idealised duct combustor Configuration III. 28

4.1 Eigenfrequencies of modes $n = 1, 2, 3$ for burner Configurations I and II plotted against non-dimensionalised burner length L/X_2. 38

4.2 Modes $n = 1, 2, 3$ of the Green's function amplitude spatial derivative for burner Configuration I, plotted against non-dimensionalised burner length L/X_2 with observer position $x_1 = L_2$ and source position $y_1 = X_2$. 39

4.3 Modes $n = 1, 2, 3$ of the Green's function amplitude spatial derivative for burner Configuration II, plotted against non-dimensionalised burner length L/X_2 with observer position $x_1 = L_2$ and source position $y_1 = X_2$. 39

5.1 Schematic of a generic computational mesh. 45

5.2 Illustration of the hydrodynamic streamlines in burner Configuration I. 48

5.3 Schematic of the flat plate used to calculate the circulation around the splitter plates. 49

5.4 Illustration of the hydrodynamic streamlines in burner Configuration I with splitter plates. 50

5.5 Illustration of the integration paths used for calculating $\bar{\ell}$ in burner Configuration I with splitter plates. 51
5.6 Illustration of a polygon and the corresponding Schwarz-Christoffel transformation. . 53
5.7 Illustration of a duct of varying cross-sectional area and the corresponding Schwarz-Christoffel transformation. 54
5.8 Illustration of the upper-half Configuration I burner and the corresponding Schwarz-Christoffel transformation. 56
5.9 Illustration of the upper-half Configuration II burner and the corresponding Schwarz-Christoffel transformation. 56
5.10 Illustration of a point source and its image about ξ-axis. 61
5.11 Illustration of geometries similar to those of burner Configuration I. Part A: geometry having similar upper half; Part B: geometry having similar lower half. 64
5.12 Illustration of two simplexes: Part A: in one-dimensional space; Part B: in two-dimensional space. 66
5.13 Illustration of hydrodynamic streamlines in burner Configuration I originating from a source located at $(-\infty, 0)$. 67
5.14 Illustration of hydrodynamic streamlines in burner Configuration II originating from a source located at $(-\infty, 0)$. 67
5.15 Illustration of the integration paths used to calculate hydrodynamic streamlines in burner Configurations I and II. 69
5.16 Illustration of hydrodynamic streamlines in burner Configuration I originating from sources located at $(-\infty, 0)$ and $(0.006, \pm 0.011)$. All three sources are of equal strength. 70

5.17 Illustration of hydrodynamic streamlines in burner Configuration I originating from sources located at $(-\infty, 0)$, $(0.017, \pm 0.006)$, and $(0.023, \pm 0.011)$, where The sources located at $(0.017, \pm 0.006)$ have three times the source strength as the other three. . . 70

5.18 Schematic of the idealised Combustor III half-plane and its image across the x_1-axis. . 71

6.1 Schematic of the idealised Combustor III depicting source configurations and control surfaces. 78

7.1 Dependence of the low order, linear theory complex resonance frequencies on the mean inlet flow speed $U_o = c_1 M_o$ for the burner of Table 7.1 when there is no unsteady heat input from the flame. 90

7.2 Dependence of the low order, linear theory complex resonance frequencies for the burner of Table 7.1 on operating power $\Pi (0 < \Pi < \Pi_{max})$ for $U_o = 2\,\mathrm{m/s}$ and $\ell_q/h = 0.8$: ———— , natural acoustic modes; - - - - - , combustion modes. 95

7.3 Dependence of the low order, linear theory complex resonance frequencies for the burner of Table 7.1 on operating power $\Pi (0 < \Pi < \Pi_{max})$ for $U_o = 4\,\mathrm{m/s}$ and $\ell_q/h = 1.6$: ———— , natural acoustic modes; - - - - - , combustion modes. 95

7.4 Dependence of the low order, linear theory complex resonance frequencies for the burner of Table 7.1 on operating power $\Pi (0 < \Pi < \Pi_{max})$ for $U_o = 6\,\mathrm{m/s}$ and $\ell_q/h = 2.4$: ———— , natural acoustic modes; - - - - - , combustion modes. 96

8.1 Mean value of the non-dimensionalised flame-source volume velocity Q_f plotted against dynamic time delay τ_1 at time $tf_o \gg 100$ for convective time delay $\tau_2 = 6\mathrm{ms}$ and power $\Pi = 30,\ 40,\ 50,\ 60\,\mathrm{kW}$. 99

8.2 Amplitude of oscillations of the non-dimensionalised flame-source volume velocity Q_f plotted against dynamic time delay τ_1 at time $tf_o \gg 100$ for convective time delay $\tau_2 = 6$ ms and power $\Pi = 30,\ 40,\ 50,\ 60$ kW. 100

8.3 Non-dimensionalised volumetric flux plotted against non-dimensionalised time showing the approach to limit cycle oscillations for Configuration III, $\Pi = 25$ kW, $\tau_1 = 18$ ms, $\tau_2 = 6$ ms. 104

8.4 Non-dimensionalised volumetric flux plotted against non-dimensionalised time during limit cycle ($tf_o \gg 100$) for Configuration III, $\Pi = 25$ kW, $\tau_1 = 18$ ms, $\tau_2 = 6$ ms. . . . 105

8.5 Limit cycle oscillations depicted in phase space for the non-dimensionalised volumetric flux during limit cycle ($tf_o \gg 100$) for Configuration III, $\Pi = 25$ kW, $\tau_1 = 18$ ms, $\tau_2 = 6$ ms. 106

8.6 Fourier transform of the volume flux plotted against frequency during limit cycle ($tf_o \gg 100$) for Configuration III, $\Pi = 25$ kW, $\tau_1 = 18$ ms, $\tau_2 = 6$ ms. 107

8.7 Non-dimensionalised volumetric flux plotted against non-dimensionalised time during limit cycle ($tf_o \gg 100$) for Configuration III, $\Pi = 50$ kW, $\tau_1 = 18$ ms, $\tau_2 = 6$ ms. . . . 108

8.8 Limit cycle oscillations depicted in phase space for the non-dimensionalised volumetric flux during limit cycle ($tf_o \gg 100$) for Configuration III, $\Pi = 50$ kW, $\tau_1 = 18$ ms, $\tau_2 = 6$ ms. 109

8.9 Fourier transform of the volume flux plotted against frequency during limit cycle ($tf_o \gg 100$) for Configuration III, $\Pi = 50$ kW, $\tau_1 = 18$ ms, $\tau_2 = 6$ ms. 109

8.10 Non-dimensionalised volumetric flux plotted against non-dimensionalised time during limit cycle ($tf_o \gg 100$) for Configuration III, $\Pi = 50$ kW, $\tau_1 = 12$ ms, $\tau_2 = 6$ ms. . . . 110

8.11 Limit cycle oscillations depicted in phase space for the non-dimensionalised volumetric flux during limit cycle ($tf_o \gg 100$) for Configuration III, $\Pi = 50$ kW, $\tau_1 = 12$ ms, $\tau_2 = 6$ ms. 110

8.12 Fourier transform of the volume flux plotted against frequency during limit cycle ($tf_o \gg 100$) for Configuration III, $\Pi = 50$ kW, $\tau_1 = 12$ ms, $\tau_2 = 6$ ms. 111

8.13 Non-dimensionalised volumetric flux plotted against non-dimensionalised time during limit cycle ($tf_o \gg 100$) for Configuration III, $\Pi = 50$ kW, $\tau_1 = 6$ ms, $\tau_2 = 6$ ms. 111

8.14 Limit cycle oscillations depicted in phase space for the non-dimensionalised volumetric flux during limit cycle ($tf_o \gg 100$) for Configuration III, $\Pi = 50$ kW, $\tau_1 = 6$ ms, $\tau_2 = 6$ ms. 112

8.15 Fourier transform of the volume flux plotted against frequency during limit cycle ($tf_o \gg 100$) for Configuration III, $\Pi = 50$ kW, $\tau_1 = 6$ ms, $\tau_2 = 6$ ms. 112

8.16 Non-dimensionalised volumetric flux plotted against non-dimensionalised time during limit cycle ($tf_o \gg 100$) for Configuration III, $\Pi = 50$ kW, $\tau_1 = 6$ ms, $\tau_2 = 12$ ms. . . . 113

8.17 Limit cycle oscillations depicted in phase space for the non-dimensionalised volumetric flux during limit cycle ($tf_o \gg 100$) for Configuration III, $\Pi = 50$ kW, $\tau_1 = 6$ ms, $\tau_2 = 12$ ms. 113

8.18 Fourier transform of the volume flux plotted against frequency during limit cycle ($tf_o \gg 100$) for Configuration III, $\Pi = 50$ kW, $\tau_1 = 6$ ms, $\tau_2 = 12$ ms. 114

8.19 Fourier transform of the volume flux plotted against frequency during limit cycle ($tf_o \gg 100$) for Configuration III, $\Pi = 50$ kW, $\tau_1 = 12$ ms, $\tau_2 = 12$ ms. 114

9.1 Schematic of the Limousine Combustor II depicting source configurations and control surfaces. 116

9.2 Non-dimensionalised volumetric flux plotted against non-dimensionalised time during limit cycle ($tf_o \gg 100$) for Configuration II, $\Pi = 50$ kW, $\tau_1 = 6$ ms, $\tau_2 = 10.5$ ms. . . . 123

9.3 Non-dimensionalised volumetric flux plotted against non-dimensionalised time during limit cycle ($tf_o \gg 100$) for Configuration II, $\Pi = 50$ kW, $\tau_1 = 12$ ms, $\tau_2 = 10.5$ ms. . . . 123

9.4 Limit cycle oscillations depicted in phase space for the non-dimensionalised volumetric flux during limit cycle ($tf_o \gg 100$) for Configuration II, $\Pi = 50$ kW, $\tau_1 = 6$ ms, $\tau_2 = 10.5$ ms. 124

9.5 Limit cycle oscillations depicted in phase space for the non-dimensionalised volumetric flux during limit cycle ($tf_o \gg 100$) for Configuration II, $\Pi = 50$ kW, $\tau_1 = 12$ ms, $\tau_2 = 10.5$ ms. 124

9.6 Fourier transform of the volume flux plotted against frequency during limit cycle ($tf_o \gg 100$) for Configuration II, $\Pi = 50$ kW, $\tau_1 = 6$ ms, $\tau_2 = 10.5$ ms. 125

9.7 Fourier transform of the volume flux plotted against frequency during limit cycle ($tf_o \gg 100$) for Configuration II, $\Pi = 50$ kW, $\tau_1 = 12$ ms, $\tau_2 = 10.5$ ms. 125

List of Tables

3.1 Limousine combustor (Configuration I and II) parameters 26

3.2 Idealised duct combustor (Configuration III) parameters 28

4.1 First three eigenfrequency modes for burner Configurations I and II 33

5.1 The burner blockage length for burner Configuration I, with and without splitter plates 52

5.2 Position of the hydrodynamic region boundaries and blockage length for burner Configurations I and II 69

7.1 Idealised duct combustor (Configuration III) parameters 88

8.1 Idealised duct combustor (Configuration III) parameters 98

9.1 Limousine combustor (Configuration II) parameters 122

Acknowledgements

I would like to acknowledge the support during the preparation of this thesis by the Marie Curie Initial Training Network LIMOUSINE, FP7 of the European Commission, Contract no. MCITN-214905. I would also like to acknowledge guidance from my supervisors Professor Graham Rogerson and Professor John Chapman, and especially technical guidance from Professor Michael Howe. This thesis would not have been possible without the thoughtful collaboration from the LIMOUSINE network partners, including Doctor Maria Heckl for supporting early numerical calculations and Doctor Jim Kok for coordinating the project.

Chapter 1

Introduction

Sound is generated by unsteady heating of a fluid. Trapped sound waves produced by a flame which are localised near the source and confined within a gas turbine, afterburner, furnace or other thermofluid device involve pressure fluctuations whose interaction with the flame modulates the heat release by changing the fuel burn rate. Large amplitude 'combustion instabilities' arise from this back-reaction when pressure and heat release are appropriately phased [1–10]. These instabilities are a significant source of structural fatigue and noise radiated into the environment.

Freely burning gas constitutes a monopole acoustic source with strength equal to the volumetric rate of expansion in the combustion zone [1, 7, 9]. There is also a secondary 'indirect' combustion dipole source producing 'entropy noise' and is due to unevenly heated combustion products accelerating unevenly within the mean flow [11–21]. Although interest in this type of source has recently revived [22–30], understanding factors governing feedback on the direct monopole flame source (i.e. aerodynamics of the oscillating mean flow, structural vibrations, flame flashback, flame-vortex interactions, burn rate fluctuations produced by flame-area oscillation, saturation of nonlinear heat release rates, etc) are probably more important for the control of the system instabilities [31–37].

Traditional vortex sources also radiate predominantly as acoustic dipoles in a confined flow because of the unsteady surface forces they induce [9, 14, 28, 38, 39]. Alternatively, in this case vorticity production by surface frictional forces caused by a large amplitude acoustic field also involve the transfer of energy between the sound and the mean flow. Vortex shedding at trailing edges is typically accompanied by the absorption of sound, and thereby opposes sound generation by the flame and possibly favours the formation of limit cycle equilibria [9].

Kok *et al.* [37, 40] have investigated limit cycle properties and acoustic spectra for a flame in a specially constructed combustor (a vertically oriented 'Rijke burner' [41]) of large aspect ratio and rectangular cross-section. Schematic outlines of two variations of the burner (Configuration I and II) are depicted in Figures 3.1 and 3.2, showing the burner rotated horizontally and viewed in the spanwise direction (out of the paper) parallel to the longer rectangular cross-sectional edge. The burner has piece-wise straight walls, and has uniform widths in the upstream and downstream sections, so that the rectangular cross-sectional area varies along the duct. Both configurations are described in detail in Chapter 3.

A full numerical treatment of the thermo-acoustics is computationally intensive and often cannot be conveniently run for more than a few characteristic operating cycles. Reduced complexity analyses that avoid a numerical treatment of the whole flow are generally based on one-dimensional acoustic models [31–33, 42–44], where upstream and downstream acoustic waves are coupled to unsteady thermal and other sources in the combustion zone by application of appropriate conservation conditions. These analyses are limited because they do not account for aeroacoustic flow properties such as vortex shedding. They also assume a planar combustion zone, where thermodynamic variables like the temperature and density 'jump' from an upstream to downstream value at one point along the duct axis. We describe one of these models in terms of its wave-equation Green's function in Chapter 4.

The Green's function is critically dependent on a burner blockage length $\bar{\ell}$ which accounts for the loss between the upstream and downstream pressure due to the constriction caused by the flame-holder. Numerical methods used to determine the burner blockage length are described in Chapter 5.

The mechanics of the combustors, as well as more complicated thermo-acoustic devices, exhibit strong superficial similarities to those governing the production of 'voiced' speech by the throttling by the glottis of the volume velocity Q_o of air expelled during contraction of the lungs. Nonlinear vibrations of the 'vocal folds' produce large and rapid variations in the glottis cross-section causing air to enter the upper section of the vocal tract as a succession of 'puffs' whose magnitudes determine the effective acoustic source strength Q of the glottis. The air flow is usually turbulent, and the environment is too geometrically and structurally complicated to permit a timely and satisfactory complete numerical analysis. But, a knowledge of the variation of Q with time t and of the corresponding mechanical state of the upper tract is sufficient to determine the principal properties of voiced speech. This can be achieved by means of a reduced complexity equation for $Q(t)$ called the *Fant* equation [45–47], a nonlinear integro-differential equation deduced with the help of an aeroacoustic Green's function [48, 49]. The equation is usually tractable, however, only when it can be assumed that the relevant acoustic frequencies are small enough for sound to propagate one-dimensionally in the vocal tract. We can formulate a thermo-acoustic Fant equation for the combustor which takes account of a generalised combustion zone, where temperature and density variations occur between two points along the duct axis, and which takes account of vortex shedding which may occur at the flame-holder. In our numerical predictions we assume a quasi-static combustion zone which is spatially fixed within the burner; however, if more information is known about the combustion zone, an even more general model can be formulated.

The general form of the Fant equation is derived from the exact equations of fluid motion. This

avoids the introduction of doubtful approximations in an analysis of a system in which sound is usually a very small by-product of the flow; simplifications and approximations are delayed until the very last stages of the acoustic calculation to avoid discarding apparently small, but nevertheless important, source terms. This is the philosophy advocated to great acclaim by Lighthill [50] in his theory of aerodynamic sound.

There is a simple analogy between the fluid-acoustic properties of the simple burner of Figure 3.3 and those of the vocal tract. The role of the glottis is played by the narrow constrictions of the flame-holder. Nonlinear throttling responsible for limit-cycle equilibria is attributed not to changes in the constriction cross-sectional area but to fluctuations in the heat release from the flame. The acoustic field downstream of the flame-holder can therefore be ascribed principally to two monopole sources of strengths corresponding respectively to the volumetric flow rate Q through the constrictions and Q_f from the flame. The mean jet shear layers downstream of the constrictions form prominent vortex sources, they are responsible principally for controlling the unsteady flow through the constrictions and the absorption of acoustic energy.

It is argued in this thesis that the methodology of the Fant equation can provide a valuable tool for investigating flow through thermo-acoustic devices like the combustors described in Chapter 3. The equation will be used to examine low frequency thermo-acoustic oscillations in the familiar approximation in which only plane waves propagate within the system. We begin with the equations governing fluid dynamics in Chapter 2 from which we derive Lighthill's acoustic analogy as well as an acoustic analogy for the total enthalpy. We also discuss various source types, including combustion sources. In Chapter 3, we discuss three combustor models used for the thermo-acoustic predictions. In Chapter 4, we derive the Green's function for both the pressure, for which we show eigenfrequency and modal amplitude results, as well as for the total enthalpy. Two methodologies for determining

the combustor blockage length are discussed in Chapter 5. The thermo-acoustic Fant equation is derived in Chapter 6 and linear and nonlinear volumetric-flow rate predictions are presented for Configuration III in Chapters 7 and 8. Nonlinear flow rate predictions for Configuration II are discussed in Chapter 9.

Chapter 2

Aeroacoustics and thermal sources

In order to formulate the problem of heat as a source of sound, it is first necessary to develop the equations which define the generation of waves, vorticity, and entropy. In the burner problem, the moving fluid contains intrinsic kinetic energy and therefore contains vorticity. The presence of the heat source indicates that there is entropy production in the fluid. The vorticity and entropy production are the ultimate source of sound production. We will review the equations governing compressible flow, as well as the formulation of Lighthill's equations and *Lighthill Acoustic's Analogy* in order to describe monopoles, dipoles and quadrupoles present in flame mixing problems. We will also formulate the acoustic analogy in terms of the total enthalpy and describe thermal sources in combustion

2.1 The equations of fluid dynamics

Five scalar equations are required to determine the motion of a fluid at time t and position $\mathbf{x} = (x_1, x_2, x_3)$ because the state of a fluid is only defined when the velocity $\mathbf{v}$ and two thermodynamic variables are

specified. The governing equations are conservation of mass, momentum, and energy.

2.1.1 The continuity equation

Consider a fixed closed surface S which encloses a volume V entirely occupied by fluid. If the density $\rho = \rho(\mathbf{x}, t)$ is defined as the mass per infinitesimal volume dV, the mass enclosed by the surface at time t is $\int \rho \, dV$ and the net rate at which mass is flowing outward across the surface is $\int \rho \mathbf{v} \cdot \mathbf{n} dS$, where $\mathbf{v}$ is the fluid velocity, $\mathbf{n}$ is the unit outward normal, and dS is the infinitesimal surface element. Mass of the fluid is conserved therefore

$$\frac{d}{dt} \int \rho \, dV = - \int \rho \, \mathbf{v} \cdot \mathbf{n} dS. \tag{2.1}$$

We differentiate under the integral sign and use the divergence theorem to yield the traditional form of the continuity equation [51]

$$\frac{\partial \rho}{\partial t} + \operatorname{div} (\rho \mathbf{v}) = 0. \tag{2.2}$$

By expanding the divergence term, the total time derivative of the density $\frac{D}{Dt} = \frac{\partial}{\partial t} + \mathbf{v} \cdot \nabla$, also known as the material derivative, of the density is formed. The continuity equation is written as

$$\frac{1}{\rho} \frac{D\rho}{Dt} + \operatorname{div} \mathbf{v} = 0. \tag{2.3}$$

2.1.2 The momentum equation

In its fundamental form, the momentum equation relates the total rate of change of momentum to the sum of forces acting on it. For convenience, a Cartesian reference frame is assumed and

subscript notation for vectors and tensors is introduced. For example, the vector $\mathbf{x}$ is written as $x_i\mathbf{e}_i$; summation over $i = 1, 2, 3$ is implied and hence the vector $x_i\mathbf{e}_i$ is equivalent to $x_1\mathbf{e}_1 + x_2\mathbf{e}_2 + x_3\mathbf{e}_3$, where $\mathbf{e}_1$, $\mathbf{e}_2$, $\mathbf{e}_3$ form an orthonormal basis with a common origin at O.

Considering a volume of fluid, the sum of the forces $\sum \mathbf{f}$ on the volume is a combination of those acting on the surface and those acting on the body. The surface forces are represented by the traction $\mathbf{t}^{(\mathbf{n})}$ per unit area. Let $\mathbf{f}_b$ be the body force per unit mass. Summing both terms and integrating over the entire body, the total forces acting on it is

$$\sum \mathbf{f} = \int_V \rho \mathbf{f}_b dV + \int_S \mathbf{t}^{(\mathbf{n})} dS, \tag{2.4}$$

which is equivalent to the convective time rate of change of momentum D/Dt. The equation of momentum conservation resolves to

$$\frac{D}{Dt}\int_V \rho \mathbf{v} dV = \int_V \rho \mathbf{f}_b dV + \int_S \mathbf{t}^{(\mathbf{n})} dS. \tag{2.5}$$

In order to resolve traction vector $\mathbf{t}^{(\mathbf{n})}$, a stress tensor is assumed σ_{ji} where $t_i^{(n)} = \sigma_{ji} n_j$. Substituting the stress tensor into Equation 2.5, using the divergence theorem and resolving the body force $\rho \mathbf{f}_b$ into one per unit volume $\mathbf{F}$, one finds

$$\frac{D}{Dt}\int_V \rho v_i dV = \int_V F_i dV + \int_V \frac{\partial \sigma_{ji}}{\partial x_j} dV. \tag{2.6}$$

The total derivative on the left-hand side can be moved within the integral by the Reynolds Transport Theorem [52]. An arbitrary function $F(t)$ is defined as the integral of $\mathcal{F}(\mathbf{x}, t)$ over the volume V, $F(t) = \int_{V(t)} \mathcal{F}(\mathbf{x}, t) dV$. The Reynolds Transport Theorem shows that the function $F(t)$ has a total

time derivative equivalent to

$$\frac{D}{Dt}F(t) = \frac{D}{Dt}\int_{V(t)} \mathcal{F}(\mathbf{x},\, t)dV = \int_{V(t)} \left(\frac{D\mathcal{F}}{Dt} + \mathcal{F}\left(\nabla \cdot \mathbf{v}\right)\right) dV. \tag{2.7}$$

Therefore for the function $\mathcal{F}(\mathbf{x},\, t) = \rho v_i$, the integral in Equation 2.6 take the form

$$\int_V \rho \frac{D}{Dt} v_i dV = \int_V F_i dV + \int_V \frac{\partial \sigma_{ji}}{\partial x_j} dV, \tag{2.8}$$

and therefore

$$\rho \frac{D}{Dt} v_i = F_i + \frac{\partial \sigma_{ji}}{\partial x_j}. \tag{2.9}$$

Conservation of angular momentum shows that the stress tensor σ_{ji} is symmetric. It has been confirmed in numerous experiments that air in thermo-acoustic problems can be considered a *Newtonian Fluid* in which the shear stress is linearly related to the shear strain by the constant η, the viscosity. The stress tensor σ_{ji} can be expressed in two terms, an isotropic term and a shear term. We can cast the momentum equation into the Navier-Stokes equation which expresses the forces acting on a fluid in terms of pressure p, viscous forces, and body forces $\mathbf{F}$. The momentum equations in its final form is [52, 53]

$$\frac{\partial \mathbf{v}}{\partial t} + \mathbf{v} \cdot \nabla \mathbf{v} = -\frac{1}{\rho}\nabla p + \frac{\eta}{\rho}\left(\nabla^2 \mathbf{v} + \frac{1}{3}\nabla(\nabla \cdot \mathbf{v})\right) + \frac{1}{\rho}\mathbf{F}. \tag{2.10}$$

2.1.3 The energy equation

The internal energy of a fluid u is defined as the difference between heat input Q and work output w such that

$$du = dQ - dw = Tds - pd\left(\frac{1}{\rho}\right), \tag{2.11}$$

where T, s, p, ρ are the respective temperature, entropy, pressure, and density of the fluid. The enthalpy $b = u + p/\rho$ is the total energy available in the system and accounts for fluid displacement. Differentiation of Equation 2.11 yields

$$db = Tds + \frac{dp}{\rho} = c_p dT, \tag{2.12}$$

where c_p is the heat capacity of the fluid at constant pressure. In aeroacoustics it is convenient to discuss the total enthalpy $B = b + \frac{1}{2}v^2$. Namely,

$$B = \int Tds + \int \frac{dp}{\rho} + \frac{1}{2}v^2 = c_p T + \frac{1}{2}v^2, \tag{2.13}$$

which is the principal thermodynamic quantity evaluated in the following aeroacoustic problem.

2.1.4 Vorticity and Crocco's momentum equation

Vorticity $\boldsymbol{\omega} = \operatorname{curl} \mathbf{v}$ is not directly imparted into the fluid from moving boundaries or any other external source; it is generated intrinsically and transported by convection and molecular diffusion. Because vorticity can make a significant contribution to noise but an infinitesimal contribution to the total fluid power, it is convenient to formulate the momentum equation into one where vorticity

is the primary source.

In the absence of body forces $\mathbf{F}$, we recast the viscous term of the momentum equation 2.10 using the vector identity $\operatorname{curl}\operatorname{curl}\mathbf{A} = \operatorname{grad}\operatorname{div}\mathbf{A} - \nabla^2\mathbf{A}$ to form

$$\frac{\partial \mathbf{v}}{\partial t} + (\mathbf{v}\cdot\nabla)\mathbf{v} + \nabla\left(\int \frac{dp}{\rho}\right) = -\nu\left(\operatorname{curl}\boldsymbol{\omega} - \frac{4}{3}\nabla(\operatorname{div}\mathbf{v})\right), \tag{2.14}$$

where $\nu = \eta/\rho$ is the kinematic coefficient of viscosity. Using the vector identity $(\mathbf{v}\cdot\nabla)\mathbf{v} = \boldsymbol{\omega}\wedge\mathbf{v} + \nabla(\frac{1}{2}v^2)$ and the expression for total enthalpy B in Equation 2.13, we cast the momentum equation in Crocco's form

$$\frac{\partial \mathbf{v}}{\partial t} + \nabla B = -\boldsymbol{\omega}\wedge\mathbf{v} + T\nabla s - \nu\left(\operatorname{curl}\boldsymbol{\omega} - \frac{4}{3}\nabla(\operatorname{div}\mathbf{v})\right), \tag{2.15}$$

where the first, second, and third terms on the right-hand side respectively correspond to vorticity from vortex shedding, from so called 'entropy waves' due to entropy variations (discussed in Section 2.3), and from viscous dissipation principally in the shear layer near a fixed boundary or wall.

2.2 Lighthill's acoustic analogy

In order to find an equation governing sound generation we refer to Lighthill who developed an acoustic analogy because he was interested in the sound generated by turbulent nozzle flows. He realised that in an ideal acoustic medium, sound propagates linearly as a wave and so he manipulated the continuity and momentum equations into one where the wave operator $\left(\frac{1}{c^2}\frac{\partial}{\partial t} - \nabla^2\right)$ is the principal one. On the left-hand side of his combined equation the wave operator would act on a thermodynamic variable, say pressure p or density ρ or total enthalpy B, and on the right-hand side

there would be a source term called the Lighthill stress tensor which describes sound productions by turbulent fluctuations.

2.2.1 Equations of linear acoustics

The equations of linear acoustics are obtained by assuming that pressure and density are each composed of a mean value, which is constant, and an acoustic perturbation value, namely $p = p_0 + p'$ and $\rho = \rho_0 + \rho'$. In an ideal acoustic field, the perturbation pressures and densities are much smaller than their respective mean values,

$$\frac{p'}{p_0} \ll 1 \quad \text{and} \quad \frac{\rho'}{\rho_0} \ll 1. \tag{2.16}$$

It is apparent in the continuity equation 2.3 that in the generalised case a volume source could be placed in the fluid, say, a pulsating body. The expression describing this configuration would has the form [54]

$$\frac{1}{\rho}\frac{D\rho}{Dt} + \nabla \cdot \mathbf{v} = q(\mathbf{x},\, t). \tag{2.17}$$

The linearised form of this equation is formed by expanding the material derivative and discarding nonlinear terms, yielding

$$\frac{1}{\rho_0}\frac{\partial \rho'}{\partial t} + \nabla \cdot \mathbf{v} = q(\mathbf{x},\, t). \tag{2.18}$$

Like the volume source generalising the continuity equation, an artificial force can generalise the Navier-Stokes equation to represent say a vibrating body; however, the force introduced can be cast with the already present body forces, not altering the momentum equation. In the absence of mean

flow, Equation 2.10 is linearised to become

$$\rho_0 \frac{\partial \mathbf{v}}{\partial t} + \nabla p' = \mathbf{F}. \tag{2.19}$$

The velocity $\mathbf{v}$ is eliminated between Equations 2.18 and 2.19 by subtracting the divergence of Equation 2.19 from the time derivative of Equation 2.18, yielding

$$\frac{\partial^2 \rho'}{\partial t^2} - \nabla^2 p' = \rho_0 \frac{\partial q}{\partial t} - \nabla \cdot \mathbf{F}. \tag{2.20}$$

The homentropic ratio of the perturbation pressure and density p'/ρ' defines the square of the speed of sound

$$c^2 \equiv \frac{p'}{\rho'} = \left(\frac{\partial p}{\partial \rho} \right)_s, \tag{2.21}$$

where the s subscript indicates that entropy is held fixed, and that homentropic and adiabatic flow is assumed, neglecting losses due to heat transfer between neighboring particles by viscous and thermal diffusion.

Substituting Equation 2.21, in the form $\rho' = p'/c_o^2$ (c_o being the mean value of c), into Equation 2.20 yields

$$\left(\frac{1}{c_o^2} \frac{\partial^2}{\partial t^2} - \nabla^2 \right) p' = \rho_0 \frac{\partial q}{\partial t} - \nabla \cdot \mathbf{F}, \tag{2.22}$$

which governs the production of sound waves by the volume source $q(\mathbf{x}, t)$ and body force $\mathbf{F}$.

As described in [55], it can be shown that small errors in specifying the source $q(\mathbf{x}, t)$ and the body force $\mathbf{F}$ in a fluid can lead to very large errors in predicting the sound; this is due to only a tiny fraction of the total available kinetic energy in a fluid radiating as sound waves, proportional to

M^5. Therefore $q(\mathbf{x}, t)$ and $\mathbf{F}$ are only introduced when it is known how they relate to real sources; rarely do they ever appear in a complete description of the sound generated in a fluid.

In order to complete the discussion of linear acoustics, we assume body forces are negligible. Equation 2.19 then implies the existence of a velocity potential φ in an incompressible and irrotational flow, where $\mathbf{v} = \nabla\varphi$. In terms of the velocity potential, the perturbation pressure is given by

$$p' = -\rho_0 \frac{\partial \varphi}{\partial t}. \tag{2.23}$$

Substituting the perturbation pressure written in this form into Equation 2.22, one obtains the equation of classical acoustics

$$\left(\frac{1}{c_0^2}\frac{\partial^2}{\partial t^2} - \nabla^2\right)\varphi = -\frac{\partial q}{\partial t}. \tag{2.24}$$

Several types of sources can be represented by $q(t)$ and those are discussed in Section 2.2.3; however, first we show Lighthill's generalisation of the source.

2.2.2 Lighthill's equations

It was Lighthill's goal to develop a wave equation having the same form as Equation 2.24 which accounted for acoustic perturbations generated by regions of turbulence in a real flow. We begin writing the momentum equation 2.9 in subscript form

$$\rho\frac{\partial v_i}{\partial t} + \rho v_j \frac{\partial v_i}{\partial x_j} = -\frac{\partial p}{\partial x_i} + \frac{\partial \tilde{\sigma}_{ij}}{\partial x_j} \equiv -\frac{\partial}{\partial x_j}\left(p\delta_{ij} - \tilde{\sigma}_{ij}\right), \tag{2.25}$$

where $\tilde{\sigma}_{ij}$ is the viscous stress tensor, $\sigma_{ij} = -p\delta_{ij} + \tilde{\sigma}_{ij}$, and δ_{ij} is the Kronecker delta function ($= 1$ for $i = j$ and 0 for $i \neq j$). $\tilde{\sigma}_{ij}$ is the antisymmetric part of the velocity gradient and vanishes

for the case of rigid motion, where there is no deformation. For a Newtonian fluid,

$$\tilde{\sigma}_{ij} = 2\eta \left(e_{ij} - \frac{1}{3} e_{kk} \delta_{ij} \right), \tag{2.26}$$

where $e_{ij} = \frac{1}{2}\left(\frac{\partial v_i}{\partial x_j} + \frac{\partial v_j}{\partial x_i}\right)$ is the rate of strain tensor. The continuity equation 2.2 is multiplied by the velocity component v_i and summed with Equation 2.25 to obtain the Reynolds form of the momentum equation

$$\frac{\partial \rho v_i}{\partial t} = -\frac{\partial \pi_{ij}}{\partial x_j}, \tag{2.27}$$

where $\pi_{ij} = \rho v_i v_j + p\delta_{ij} - \tilde{\sigma}_{ij}$ is the momentum flux tensor. The pressure term p is replaced by the perturbation pressure $p - p_0$. In an ideal, linear acoustic medium, the momentum flux tensor contains only the pressure

$$\pi^0_{ij} = (p - p_0)\delta_{ij} \equiv c_0^2(\rho - \rho_0)\delta_{ij}, \tag{2.28}$$

and the momentum equation then reduces to

$$\frac{\partial(\rho v_i)}{\partial t} + \frac{\partial}{\partial x_i}\left[c_0^2(\rho - \rho_0)\right] = 0. \tag{2.29}$$

Writing the continuity equation 2.2 as

$$\frac{\partial}{\partial t}(\rho - \rho_0) + \frac{\partial(\rho v_i)}{\partial x_i} = 0, \tag{2.30}$$

the momentum density ρv_i can be eliminated between Equations 2.29 and 2.30 to yield the equation of linear acoustics satisfied by the perturbation density $\rho - \rho_0$

$$\left(\frac{1}{c_0^2}\frac{\partial^2}{\partial t^2} - \nabla^2\right)\left[c_0^2(\rho - \rho_0)\right] = 0. \tag{2.31}$$

In this approximation, it is assumed that the fluid is at rest at infinity and unbounded. Additionally, turbulence, externally applied forces, and moving boundaries are neglected. We assert that the sound generated by turbulence in a real fluid is equivalent to that produced by an ideal, stationary acoustic medium forced by the stress distribution

$$\begin{aligned} T_{ij} &= \pi_{ij} - \pi_{ij}^0 \\ &= \rho v_i v_j + \left((p - p_0) - c_0^2(\rho - \rho_0)\right)\delta_{ij} - \tilde{\sigma}_{ij}, \end{aligned} \tag{2.32}$$

where T_{ij} is the Lighthill stress tensor, which is comprised of three terms. The first term $\rho v_i v_j$ is called the Reynolds stress; it is a nonlinear quantity due to random turbulent fluctuations in fluid momentum and can be neglected in the absence of turbulence. The second term represents the excess of momentum transfer by the pressure over that in the ideal, linear fluid of density ρ_0 and speed of sound c_0. This is produced by wave amplitude nonlinearity, and by mean density variations in the source flow. The third term $\tilde{\sigma}_{ij}$ is due to the viscous stress; it is linear in the perturbation quantities and accounts for the attenuation of sound. $\tilde{\sigma}_{ij}$ can be neglected in source regions of very high Reynolds number.

The Reynolds form of the momentum equation, written for an ideal, stationary acoustic medium

of mean density ρ_0 and speed of sound c_0 subject to the externally applied stress T_{ij}, takes the form

$$\frac{\partial \rho v_i}{\partial t} + \frac{\partial \pi_{ij}^0}{\partial x_j} = -\frac{\partial}{\partial x_j}\left(\pi_{ij} - \pi_{ij}^0\right). \tag{2.33}$$

Rewriting the momentum flux for an ideal, linear acoustic medium and resolving the difference in momentum flux to the Lighthill stress tensor, Equation 2.33 can be rewritten as

$$\frac{\partial \rho v_i}{\partial t} + \frac{\partial}{\partial x_j}\left[c_0^2(\rho - \rho_0)\right] = -\frac{\partial T_{ij}}{\partial x_j}. \tag{2.34}$$

The momentum density term can be eliminated using the continuity equation 2.2 using the procedure used in the formulation of Equation 2.31, yielding the Lighthill equation:

$$\left(\frac{1}{c_0^2}\frac{\partial^2}{\partial t^2} - \frac{\partial^2}{\partial x_j x_j}\right)\left[c_0^2(\rho - \rho_0)\right] = \frac{\partial^2 T_{ij}}{\partial x_i x_j}. \tag{2.35}$$

2.2.3 Monopoles, dipoles, and quadrupoles

The most significant type of source in heat-generated noise is the 'monopole' type source which can be attributed to the volume flux from the flame. The strength of a flame source is defined by the rate of entropy production where $q(t)$ in Equation 2.24 is

$$q(t) = \frac{1}{c_p}\frac{\partial s}{\partial t}. \tag{2.36}$$

The second type of source is the 'dipole' and can be thought of as two sources of opposite strength, $q(t)$ and $-q(t)$, separated by a distance ℓ [56], where $\ell \ll \lambda$ (λ being the sound wavelength) in order

to ensure the source is acoustically *compact*. Due to their counter-acting nature, they have a much smaller effect in the *far-field* than the monopole, where the far-field is the area at distance $r \gg c/f$ ($f = \omega/2\pi$ being the sound frequency) away from the source. In thermo-acoustic problems, the dipole-type sources consist of three types: (i) vorticity due to vortex shedding $\boldsymbol{\omega} \wedge \mathbf{v}$; (ii) entropy gradient perturbations $\partial(T\nabla s)/\partial t$; and (iii) and vorticity due to viscosity in the shear layer near the duct wall $\nu \operatorname{curl} \boldsymbol{\omega}$.

The third type of source is the 'quadrupole' and can be visualised as a nearby pair of equal and opposite dipoles. A compact quadrupole has a smaller effect in the far-field perturbation pressure than either the monopole or dipole. In the thermo-acoustic problems, the quadrupoles consist of vorticity and entropy sources downstream of the flame, and are typically ignored.

2.3 Thermal sources

We consider two types of thermal sources: the first type is a simple heat source, such as say a wire gauze within a duct, and generates waves strictly due to entropy production; the second is more complex, such as say a flame, and involves not only waves generated by entropy production but also so called *entropy waves* caused by entropy gradients and mixing due to vorticity.

A heat source which strictly generates entropy can be formulated in terms of the perturbation pressure from Equation 2.22. Neglecting surface forces, we have

$$\left(\frac{1}{c_0^2}\frac{\partial^2}{\partial t^2} - \nabla^2\right) p = \rho_0 \frac{\partial q}{\partial t},$$

where p here and henceforth designates the perturbation pressure, and c_o and ρ_o respectively designate

the mean speed of sound and density. We consider a heated uniform duct of cross-sectional area $\mathcal{A}$ having respective upstream and downstream temperatures T_1 and T_2, densities ρ_1 and ρ_2, and speeds of sound c_1 and c_2. The heat source q_h would typically be defined in terms of heat release per unit length of the duct and the pressure wave equation would take the form (from [9])

$$\left(\frac{1}{c_0^2}\frac{\partial^2}{\partial t^2} - \nabla^2\right) p = \frac{\rho_2}{\mathcal{A} c_p \rho_1 T_1}\frac{\partial q_h}{\partial t}, \tag{2.37}$$

where c_p is the fluid specific heat capacity. The pressure can be directly determined in terms of a *Green's function* which is discussed in detail in Chapter 4.

For more complicated sources where the entropy gradients and vorticity are significant, we formulate a wave equation in terms of the total enthalpy $B = c_p + \frac{1}{2}v^2$. Taking Crocco's formulation of the momentum equation assuming compressible effects are uniform

$$\frac{\partial \mathbf{v}}{\partial t} + \nabla B = -\boldsymbol{\omega} \wedge \mathbf{v} + T\nabla s - \nu \operatorname{curl} \boldsymbol{\omega}, \tag{2.38}$$

we multiply it by the density ρ and take the divergence to obtain

$$\operatorname{div}\left(\rho\frac{\partial \mathbf{v}}{\partial t}\right) + \operatorname{div}\left(\rho\nabla B\right) = -\operatorname{div}\left(\rho\boldsymbol{\omega} \wedge \mathbf{v} - \rho T\nabla s + \rho\nu \operatorname{curl} \boldsymbol{\omega}\right), \tag{2.39}$$

assuming ν is constant. The equation of continuity 2.3 allows us to write the first term on the left

side in the form

$$\begin{aligned}
\text{div}\left(\rho\frac{\partial \mathbf{v}}{\partial t}\right) &= \nabla\rho\cdot\frac{\partial \mathbf{v}}{\partial t} + \rho\frac{\partial}{\partial t}\text{div}\,\mathbf{v} \\
&= \nabla\rho\cdot\frac{\partial \mathbf{v}}{\partial t} - \rho\frac{\partial}{\partial t}\left(\frac{1}{\rho}\frac{D\rho}{Dt}\right) \\
&= \nabla\rho\cdot\frac{\partial \mathbf{v}}{\partial t} - \rho\frac{\partial}{\partial t}\left(\frac{1}{\rho}\frac{\partial\rho}{\partial t}\right) - \frac{\partial \mathbf{v}}{\partial t}\cdot\nabla\rho - \rho\mathbf{v}\cdot\nabla\left(\frac{1}{\rho}\frac{\partial\rho}{\partial t}\right) \\
&= -\rho\frac{D}{Dt}\left(\frac{1}{\rho}\frac{\partial\rho}{\partial t}\right).
\end{aligned} \tag{2.40}$$

We can substitute the relation

$$d\rho = \left(\frac{\partial\rho}{\partial p}\right)_s dp + \left(\frac{\partial\rho}{\partial T}\right)_p\left(\frac{\partial T}{\partial s}\right)_p ds = \frac{1}{c^2}dp - \frac{\beta\rho T}{c_p}ds,$$

$\beta = (-1/\rho)(\partial\rho/\partial T)_p$ being the constant-pressure expansion coefficient, into the last term of Equation 2.40 so that we can recast the the first term of Equation 2.39 as

$$\text{div}\left(\rho\frac{\partial \mathbf{v}}{\partial t}\right) = -\rho\frac{D}{Dt}\left(\frac{1}{\rho}\frac{\partial\rho}{\partial t}\right) = -\rho\frac{D}{Dt}\left(\frac{1}{\rho c^2}\frac{\partial p}{\partial t}\right) + \rho\frac{D}{Dt}\left(\frac{\beta T}{c_p}\frac{\partial s}{\partial t}\right). \tag{2.41}$$

The scalar product of the velocity $\mathbf{v}$ and the momentum equation 2.38 supplies the relation

$$\frac{1}{\rho}\frac{\partial p}{\partial t} = \frac{DB}{Dt} - T\frac{Ds}{Dt} + \frac{\nu}{2}\mathbf{v}\cdot\text{curl}\,\boldsymbol{\omega}, \tag{2.42}$$

which allows us to replace the pressure term on the right side of Equation 2.41, and again recast the initial velocity term on the left of Equation 2.39 into the form

$$\text{div}\left(\rho\frac{\partial \mathbf{v}}{\partial t}\right) = -\rho\frac{D}{Dt}\left(\frac{1}{c^2}\frac{DB}{Dt}\right) + \rho\frac{D}{Dt}\left(\frac{1}{c^2}\left(T\frac{Ds}{Dt} - \frac{\nu}{2}\mathbf{v}\cdot\text{curl}\,\boldsymbol{\omega}\right)\right) + \rho\frac{D}{Dt}\left(\frac{\beta T}{c_p}\frac{\partial s}{\partial t}\right). \tag{2.43}$$

Substitution of Equation 2.43 into 2.39 yields the acoustic analogy in terms of the total enthalpy

$$\left(\rho\frac{D}{Dt}\left(\frac{1}{c^2}\frac{D}{Dt}\right)-\frac{\partial}{\partial x_j}\left(\rho\frac{\partial}{\partial x_j}\right)\right)B$$
$$=\operatorname{div}\left(\rho\boldsymbol{\omega}\wedge\mathbf{v}-\rho T\nabla s+\rho\nu\operatorname{curl}\boldsymbol{\omega}\right)+\rho\frac{D}{Dt}\left(\frac{\beta T}{c_p}\frac{\partial s}{\partial t}\right) \tag{2.44}$$
$$+\rho\frac{D}{Dt}\left(\frac{1}{c^2}\left(T\frac{Ds}{Dt}-\frac{\nu}{2}\mathbf{v}\cdot\operatorname{curl}\boldsymbol{\omega}\right)\right).$$

The term on the left is very similar to the wave operator acting on the enthalpy. The first two terms on the right are principally due to scattering with the three terms within the first accounting for (i) vortex shedding, (ii) entropy waves, and (iii) viscous dissipation near walls, and the second term due to entropy production near the flame. The third term on the right principally accounts for dissipation and typically makes only a negligible contribution to the sound and will be ignored [9].

For problems considered henceforth we can assume Mach numbers $M = v/c \ll 1$ and an ideal gas where $\beta = 1/T$. We also assume density variations are small and can take momentous derivatives D/Dt as scalar time differentials $\partial/\partial t$. We have the final form of the acoustic analogy equation for the total enthalpy

$$\left(\frac{1}{c^2}\frac{\partial}{\partial t^2}-\frac{\partial^2}{\partial x_j x_j}\right)B=\operatorname{div}\left(\boldsymbol{\omega}\wedge\mathbf{v}-(T\nabla s)'+\nu\operatorname{curl}\boldsymbol{\omega}\right)+\frac{\partial}{\partial t}\left(\frac{1}{c_p}\frac{\partial s}{\partial t}\right), \tag{2.45}$$

where here and henceforth B denotes the perturbation value of the total enthalpy relative to its local value in the absence of flow and sound, and $(T\nabla s)'$ denotes the corresponding perturbation value. In Chapter 4 we discuss the method of solution for Equation 2.45, the *Green's function*.

2.3.1 Combustion models

The source term on the right side of Equation 2.45 is dependent on the unsteady heat release from the flame Q'_f (having steady release $\bar{Q}_f$). The combustion models which define the relationship between the heat release and other variables, such as the say flow speed, is often determined empirically. It is not our goal to review combustion models; however, the calculations in Chapters 7-9 depend on these so we will briefly explore a few types of models. Lieuwen [35] have written a thorough review of combustion, especially related to thermo-acoustics; this will be the basis of this discussion.

Acoustic wave-flame dynamics involve the simultaneous interactions between kinetic, fluid mechanic, and acoustic processes over a large range of timescales. Different physical processes may dominate these interactions at different regions of the relevant parameter space [42, 57, 58]. We can define four different flame regimes [59]: 'wrinkled flamelets', 'corrugated flamelets', 'well-stirred reactor', 'distributed reaction zone'. Flame regimes described as wrinkled or corrugated flamelets correspond to situations where the reactions occur in thin sheets that retain their laminar structure. These sheets become increasingly wrinkled and multiconnected with increasing unsteady flow flux Q', relative to the laminar flame flux $\bar{Q}_f$. Flame regimes described as well-stirred reactor correspond to the limit where mixing occurs much more rapidly than chemical kinetics and reactions occur homogeneously over a distributed volume. Our applications will be confined to the wrinkled flamelets.

Heat release from combustion is typically governed by a flame transfer function which has the form

$$F(\omega) = \frac{\hat{Q}_f/\bar{Q}_f}{\hat{Q}/\bar{Q}}, \tag{2.46}$$

where $\hat{Q}_f$ and $\bar{Q}_f$ are the frequency domain and steady components of the heat release, and $\hat{Q}$

and $\bar{Q}$ are the frequency domain and steady components of the volumetric flux from the mean flow surrounding the flame. The transfer function $F(\omega)$ depends on several factors including the geometry of the combustion zone, the method of fuel injection, as well as thermodynamic parameters within and surrounding the combustion.

Bloxsidge [60] describes an experimental afterburner used for measuring a flame transfer function. The afterburner is modeled as a duct with circular cross-section. Premixed fuel and air enter upstream through a chocked nozzle and continue downstream until encountering a conical 'gutter' acting as a flame-holder, after which the fuel and air burn until finally reaching the duct exit. Several measurements are taken from the experimental afterburner. Bloxsidge and Dowling empirically derive a flame transfer function for this configuration [31, 42], having the form

$$F(\omega) = \frac{1}{1 + i\omega\tau_1} \mathrm{e}^{-i\omega\tau_2}, \tag{2.47}$$

where ω is the complex disturbance frequency, and τ_1 and τ_2 are the respective dynamic and convective time delay. τ_1 is not physically very well understood; however, τ_2 can be thought to be the time taken for the mean flow to convect across the combustion zone.

The combustor models used in our analysis, which are described in Chapter 3, are very similar to those used in [31, 42, 60] so we will use flame transfer function 2.47 in Chapters 7-9.

Chapter 3

Models of a generic combustor

In our analysis we study three different combustor configurations. The aspect ratio of each is sufficiently large to permit flow and combustion characteristics to be regarded as uniform across the span and modeled by two-dimensional analytical and numerical methods [37, 40, 61–63]. In each case, air enters the upstream duct through a perforated end-wall; the downstream is open. The flame is in the upstream section of the combustor. The first two configurations are very similar and only vary in the combustor outside wall geometry in the area around the 'flame-holder'; they are the same designs used in the Limousine project. The Limousine project (LIMOUSINE *Limit cycles of thermo-acoustic oscillations in gas turbine combustors*) supports this research and is a Marie Curie Initial Training Network consisting of seven academic and five industrial partners. Below we describe all three combustor configurations in detail using two-dimensional analytical and numerical methods [37, 40, 61–63]. In each case, air enters the upstream duct through a perforated end-wall; the downstream is open. The flame is in the upstream section of the combustor. The first two configurations are very similar and only vary in the combustor outside wall geometry in the area around the 'flame-holder'; they are the same designs used in the Limousine project. The third configuration

varies significantly from the other two. It is a uniform duct a thin constriction, which produces a shear layer similar to that of the flame holder. Below we describe all three combustor configurations in detail.

3.1 The Limousine combustor

Both Limousine combustors are modeled as a Rijke burner [40] having a closed upstream end and open downstream end from which air exits. The air is heated by a flame fueled by a flame-holder. Rotating the burner so that it rests horizontally, the axial coordinate is x_1 and is measured from the downstream edge of the flame-holder where $x_1 = 0$; the burner has length L and cross-sectional span ℓ_s. A plane is cut at arbitrary depth because of the aforementioned two-dimensional assumption due to the large aspect ratio. The lateral coordinate is x_2 and is measured from the centerline of the plane, parallel to the x_1-axis, where $x_2 = 0$; the upper boundary of the burner is defined by the function $h(x_1)$. The wall of the burner is height h_1 above the centerline at the entrance and h_2 at the exit. The upstream and downstream regions of the burner have respective cross-sectional areas $\mathcal{A}_1$ and $\mathcal{A}_2$, mean temperatures T_1 and T_2, perturbation pressures p_1' and p_2', mean densities ρ_1 and ρ_2, and sound speeds c_1 and c_2. The initial burner configuration (Configuration I) is depicted in Figure 3.1. In this configuration, the duct walls and flame-holder are parallel so that the cross-sectional area inclusive of the constriction caused by the flame-holder remains unchanged aft of the downstream edge of the flame-holder.

The second burner configuration (Configuration II) is depicted in Figure 3.2. This configuration varies from the first in that the duct cross-sectional area, inclusive of the flame-holder constriction, decreases from $\mathcal{A}_1$ starting at the upstream edge of the flame-holder and then increases at the

Table 3.1: Limousine combustor (Configuration I and II) parameters

Description	Value
Upstream duct cross-sectional area $\mathcal{A}_1$	0.011 m^2
Downstream duct cross-sectional area $\mathcal{A}_2$	0.006 m^2
Distance from flame-holder edge to duct entrance L_1	0.322 m
Distance from flame-holder edge to effective duct exit $\bar{L}_2$	1.142 m
Upstream mean temperature T_1	288 K
Downstream mean temperature T_2	1200 K
Upstream mean density ρ_1	1.214 kg/m^3
Downstream mean density ρ_2	0.292 kg/m^3

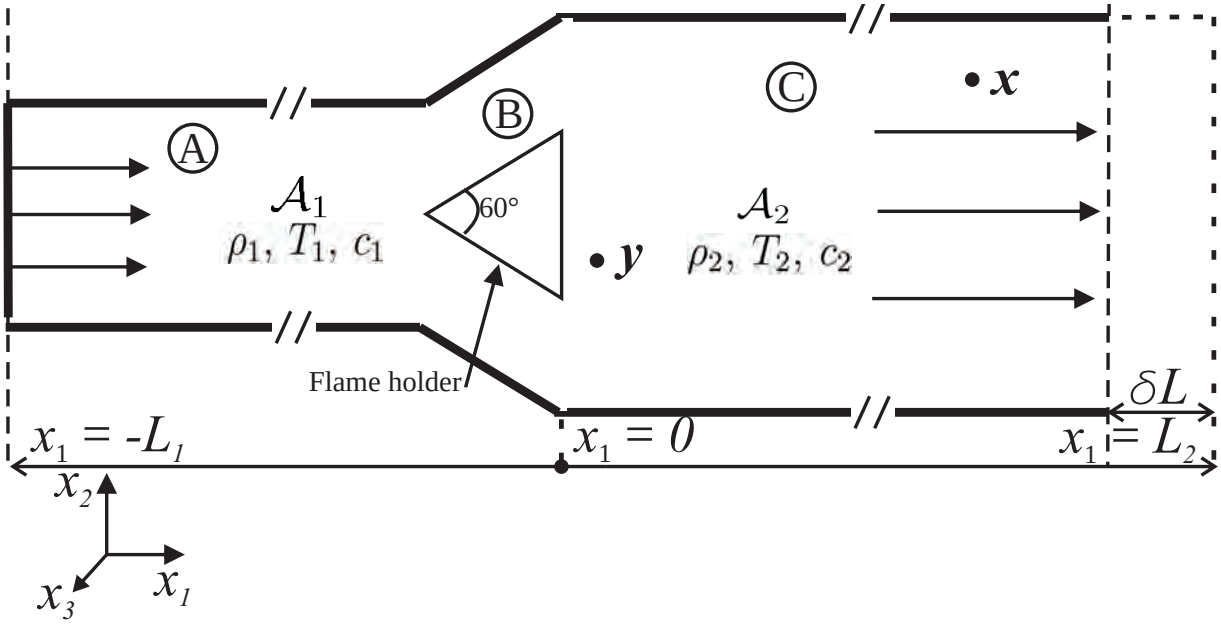

Figure 3.1: Schematic section of the first Limousine combustor Configuration I.

downstream edge to $\mathcal{A}_2$. This change was made in order to increase the source flow speed near the downstream edge of the flame-holder in order to increase mixing with the flame.

In both configurations described above the burners are divided into three regions: A, B, and C. The air enters into A (the cold acoustic region) $-L_1 < x_1 < X_1$ where the flow is one-dimensional. The air is then heated in B (the hydrodynamic region) $X_1 < x_1 < X_2$ where the flow is two-dimensional, transitioning in area from $\mathcal{A}_1$ to $\mathcal{A}_2$. Finally, the air passes into the hot acoustic region $X_2 < x_1 < L_2$ where the flow is again one-dimensional. The heat released from the flame is

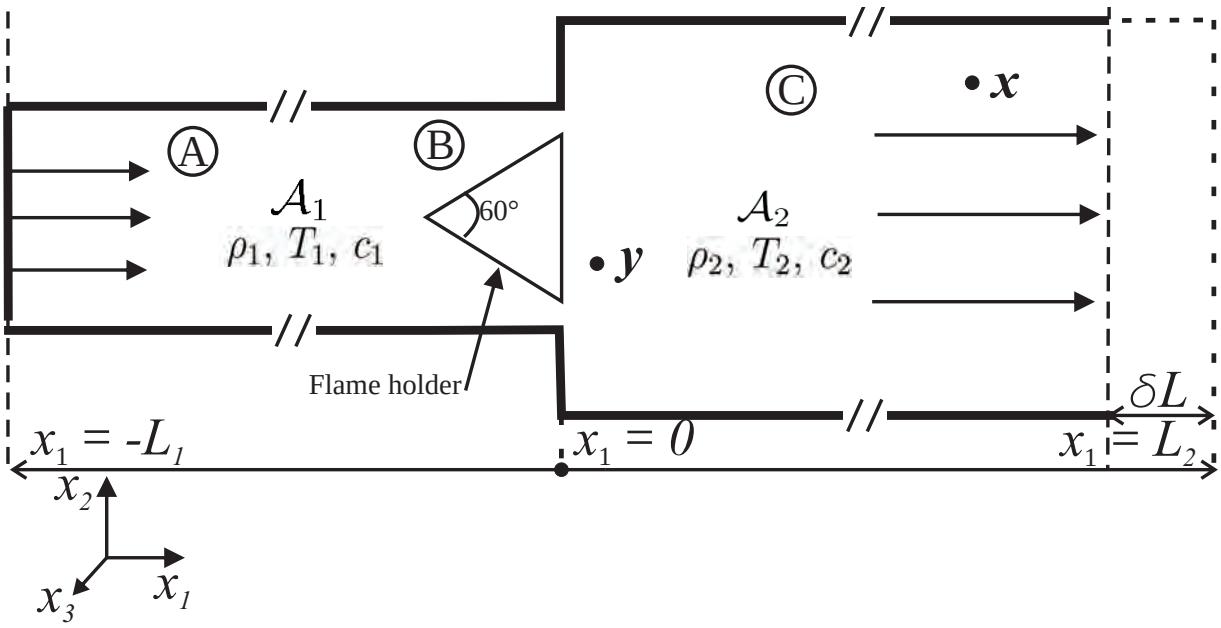

Figure 3.2: Schematic secction of the second Limousine combustor Configuration II.

$Q_f = \bar{Q}_f + Q'_f$, where $\bar{Q}_f$ is mean part and leads to the increase in mean temperature, and Q'_f is the fluctuating part and acts as a source of the acoustic waves. A pressure node is located at the entrance plane $x_1 = -L_1$ due to it being a closed and another located just outside burner exit of the burner $x_1 = L_2 + \delta L = \bar{L}_2$, in order to account for its open end.

3.2 The idealised duct combustor

The third and idealised combustor configuration (Configuration III) is devised in order to formulate the Fant equation approach to the problem in Chapters 6-8. The configuration varies significantly in geometry but captures similar flow features present in the Limousine combustor configurations.

The combustor is modeled as a duct of uniform cross-sectional area $\mathcal{A}$. In place of the flame-holder there is a thin constriction which produces a similar shear layer and thus similar vortex shedding. The point at which the constriction coincides with the centerline of the duct is defined as the origin.

Table 3.2: Idealised duct combustor (Configuration III) parameters

Description	Value
Duct cross-sectional area $\mathcal{A}$	0.011 m^2
Distance from aperture to duct entrance L_1	0.322 m
Distance from aperture to effective duct exit $\bar{L}_2$	1.142 m
Upstream mean temperature T_1	288 K
Downstream mean temperature T_2	1200 K
Upstream mean density ρ_1	1.214 kg/m^3
Downstream mean density ρ_2	0.292 kg/m^3

The positive x_1-axis is measured along the centerline toward the downstream end. The positive x_2-axis is measured along the constriction toward the upper-duct wall. The flame is just downstream of the constriction. The upstream and downstream ends of the duct are respectively modeled as closed (at $x_1 = -L_1$) and open (at $x_1 = \bar{L}_2$). The upstream and downstream regions have respective mean temperatures T_1 and T_2, mean densities ρ_1 and ρ_2, and sound speeds c_1 and c_2, which is identical to that of the other configurations. The duct is depicted in Figure 3.3 and its parameters are specified in Table 3.2.

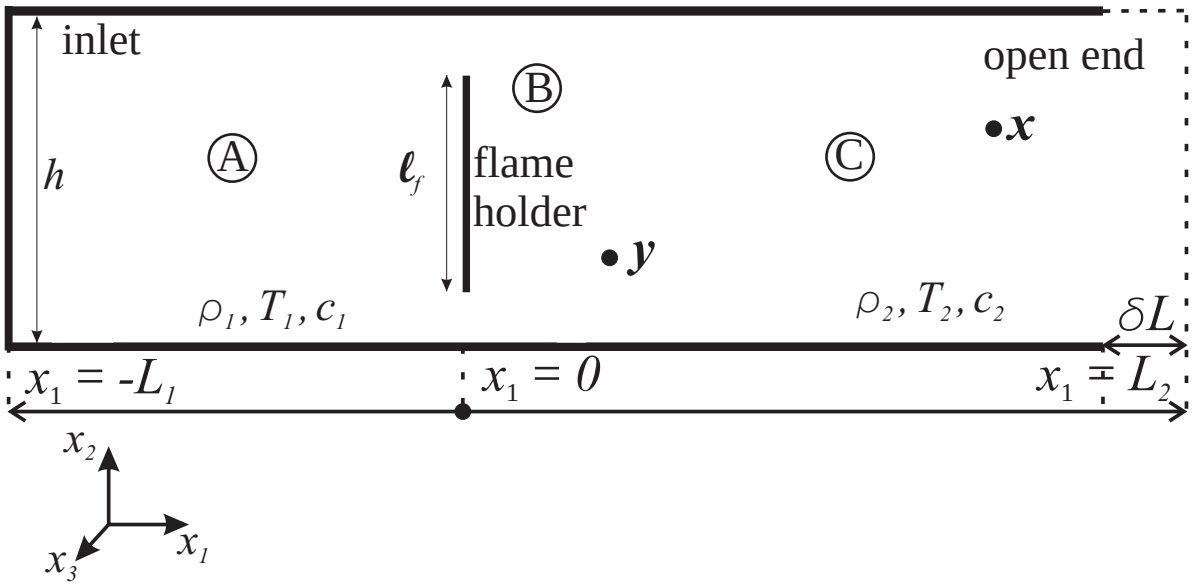

Figure 3.3: Schematic section of the idealised duct combustor Configuration III.

Chapter 4

The Green's function

The Green's function is the solution to the wave equation generated by an impulse point source at location $\mathbf{x} = \mathbf{y}$ at time $t = \tau$. Explicitly,

$$\left(\frac{1}{c^2}\frac{\partial^2}{\partial t^2} - \nabla^2\right) G = \delta(\mathbf{x} - \mathbf{y})\delta(t - \tau) \quad \text{where } G = 0 \text{ for } t < \tau, \tag{4.1}$$

where the Green's function $G = G(\mathbf{x}, \mathbf{y}, t, \tau)$ and c is the local speed of sound. The Green's function is unique to any geometric and thermodynamic configuration and has the property that its convolution with an arbitrary source, say $q(\mathbf{x}, t)$, yields the wave response due to that source. Namely,

$$\mathcal{F}(\mathbf{x}, t) = \int \int_{-\infty}^{\infty} q(\mathbf{y}, \tau) G(\mathbf{x}, \mathbf{y}, t, \tau) d^3\mathbf{y} d\tau, \tag{4.2}$$

where

$$\left(\frac{1}{c^2}\frac{\partial^2}{\partial t^2} - \nabla^2\right) \mathcal{F} = q(\mathbf{x}, t). \tag{4.3}$$

In the present problem, for each of the combustor configurations described in Chapter 3, the walls of the combustor are sufficiently rigid to assume $\partial G/\partial x_n = 0$ on the burner walls, where x_n is directed outward from the wall.

We examine two Green's function for the combustor configurations discussed in Chapter 3. The first is the pressure Green's function and is applied strictly to the Limousine combustor Configurations I and II discussed in Section 3.1 and assumes an abrupt temperature jump due to the flame between the upstream and downstream sections. The time-domain Green's function is calculated from its time-harmonic Green's function; an example is shown determining the ideal combustor length from the Green's function modal amplitudes for both Configurations I and II. The second Green's function is the total enthalpy Green's function and is applied to combustor Configuration III discussed in Section 3.2 and is determined by matching between the two acoustic (A and C) and hydrodynamic (C) regions. This Green's function is used to formulate the Fant equation in Chapters 6-8. In both calculations, the Green's function is dependent on the 'blockage length' $\bar{\ell}$ due to the flame-holder in Configurations I and II and constriction in Configuration III; a detailed discussion on its calculation is in Chapter 5.

4.1 The pressure Green's function

The pressure Green's function satisfies Equation 4.1 and when convoluted with a simple source, which describes only volume entropy production such as on the right of Equation 2.37, yields the pressure response from that source. In this section we examine the pressure Green's function calculated from the burner eigenfrequencies and its time-harmonic Green's function. We analyse burner stability using the Green's function modal amplitudes as the stability criterion.

4.1.1 Eigenfrequencies

An infinite number of eigenfrequencies exist in the Limousine combustor; however, experimental results show that instabilities are caused by only the first few [29]. Therefore, in an effort to be concise, we confine the discussion to the first three.

Derivation of the equation satisfied by the eigenfrequencies involves first imposing a form of the velocity potential ϕ in the acoustic regions A and C where a sinusoidal potential is assumed, and also in hydrodynamic region B where a linear dependence on x_1 is assumed due to the region being acoustically compact. The velocity potential has the form

$$\phi = \begin{cases} a \sin \frac{\omega}{c_1}(x_1 - L_1) & \text{acoustic region A} & x_1 < X_1, \\ \alpha + \beta \frac{\mathcal{A}_2}{\mathcal{A}_1}(x_1 - (X_1 - L_l)) & \text{hydrodynamic region B} & x_1 \approx X_1, \\ \alpha + \beta(x_1 - (X_2 - \bar{L}_2)) & \text{hydrodynamic region B} & x_1 \approx X_2, \\ b \sin \frac{\omega}{c_2}(x_1 - \bar{L}_2) & \text{acoustic region C} & x_1 > X_2, \end{cases} \tag{4.4}$$

where $a = a(y_1, \omega)$, $b = b(y_1, \omega)$, $\alpha = \alpha(y_1, \omega)$, and $\beta = \beta(y_1, \omega)$ are constants to be determined.

The velocity potentials above must provide continuity of volume flux and pressure across the boundaries at $x_1 = X_1$ and $x_1 = X_2$ and therefore must satisfy the conditions below on the left, yielding the equations below on the right:

$$\begin{aligned} &\text{Volume flux at } X_1\text{:} && \mathcal{A}_1 \left.\tfrac{\partial \phi}{\partial x}\right|_{X_{1-}} = \mathcal{A}_1 \left.\tfrac{\partial \phi}{\partial x}\right|_{X_{1+}} && : && a\tfrac{\omega}{c_1} \cos \tfrac{\omega}{c_1}(X_1 - L_1) = \beta \tfrac{\mathcal{A}_2}{\mathcal{A}_1}, \\ &\text{Pressure at } X_1\text{:} && \rho_1 \phi|_{X_{1-}} = \rho_1 \phi|_{X_{1+}} && : && a \sin \tfrac{\omega}{c_1}(X_1 - L_1) = \alpha + \beta \tfrac{\mathcal{A}_2}{\mathcal{A}_1} L_1, \\ &\text{Volume flux at } X_2\text{:} && \mathcal{A}_2 \left.\tfrac{\partial \phi}{\partial x}\right|_{X_{2-}} = \mathcal{A}_2 \left.\tfrac{\partial \phi}{\partial x}\right|_{X_{2+}} && : && \beta = b\tfrac{\omega}{c_2} \cos \tfrac{\omega}{c_2}(X_2 - \bar{L}_2), \\ &\text{Pressure at } X_2\text{:} && \rho_1 \phi|_{X_{2-}} = \rho_2 \phi|_{X_{2+}} && : && \alpha + \beta \bar{L}_2 = b\tfrac{\rho_2}{\rho_1} \sin \tfrac{\omega}{c_2}(X_2 - \bar{L}_2), \end{aligned} \tag{4.5}$$

where subscript $\mp$ respectively designate upstream and downstream of the respective boundary. Equation 4.5 is transformed into a 4×4 system of equations. The determinant yields the equation satisfied by the eigenfrequencies. Namely,

$$f_\omega(\omega_n) = \frac{\rho_2}{\rho_1} \cos\omega_n\tau_{L1} \sin\omega_n\tau_{L2} + \cos\omega_n\tau_{L2} \left[\frac{\mathcal{A}_2}{\mathcal{A}_1} \frac{c_1}{c_2} \sin\omega_n\tau_{L1} + \bar{\ell}\, \frac{\omega_n}{c_2} \cos\omega_n\tau_{L1} \right] = 0, \tag{4.6}$$

where $\tau_{L1} = (X_1 - L_1)/c_1$ and $\tau_{L2} = (\bar{L}_2 - X_2)/c_2$ are the times for sound to travel from one of the two pressure nodes at $x_1 = -L_1$ and $x_1 = \bar{L}_2$ to the respective nearest hydrodynamic-region boundary at $x_1 = X_1$ and $x_1 = X_2$. The burner blockage length $\bar{\ell}$ is derived in Section 5.1 and defined in terms of the velocity potential φ^*; it has the form

$$\bar{\ell} = \int_{X_2}^{\infty} \left(\frac{\partial\varphi^*}{\partial\xi} - 1 \right) d\xi + \int_{-\infty}^{X_2} \left(\frac{\partial\varphi^*}{\partial\xi} - \frac{\mathcal{A}_2}{\mathcal{A}_1} \right) d\xi + \frac{\mathcal{A}_2}{\mathcal{A}_1}(X_2 - X_1).$$

Substituting the blockage length $\bar{\ell}$ into Equation 4.5, we obtain a more concise form of the equations governing conservation of volume flux and momentum

$$\begin{aligned} &\text{Volume flux:} && \mathcal{A}_1 \tfrac{\partial\phi_1}{\partial x} - \mathcal{A}_2 \tfrac{\partial\phi_{2+}}{\partial x} = 0, \\ &\text{Momentum:} && p_{2-} - p_1 = \rho_1 \tfrac{\partial\phi_{2+}}{\partial t} - \rho_1 \tfrac{\partial\phi_1}{\partial t} = \rho_1 \bar{\ell}\, \tfrac{\partial\phi_{2-}}{\partial x}. \end{aligned} \tag{4.7}$$

Equation 4.6 is solved numerically using the Newton-Raphson method with starting estimate $\omega_n^{(0)} = n\pi c_2/(\bar{L}_2 - L_1)$. Each consecutive estimate varies from the present estimate by the ratio of the function's value and the function's derivative at that estimate, namely

$$\omega_n^{(k+1)} = \omega_n^{(k)} - f_\omega(\omega_n^{(k)}) / f'_\omega(\omega_n^{(k)}),$$

where $f_\omega(\omega)$ is the function defined by Equation 4.6.

We determine eigenfrequencies for Configuration I and II described in Table 3.1. The boundaries of the hydrodynamic region B and the blockage length are determined for both configurations in Section 5.2. For Configuration I and II, these values are respectively found to be $X_1 = -0.038$ m, $X_2 = 0.015$ m, $\bar{\ell} = 0.095$ m, and $X_1 = -0.038$ m, $X_2 = 0.021$ m, $\bar{\ell} = 0.138$ m. The blockage lengths are respectively 80% and 130% longer than the hydrodynamic region. Table 4.1 lists the first three eigenfrequency modes $f = \omega/2\pi$ for Configurations I and II.

Table 4.1: First three eigenfrequency modes for burner Configurations I and II

Eigenfrequency mode n	1	2	3
Eigenfrequency, Configuration I	172.6 Hz	429.9 Hz	544.9 Hz
Eigenfrequency, Configuration II	172.5 Hz	426.3 Hz	528.2 Hz

4.1.2 Green's function modal amplitudes

We can define the Green's function in terms of a sum of modal amplitudes g_n such that

$$G(\mathbf{x}, \mathbf{y}, t, \tau) \equiv H(t-\tau) \sum_{n=1}^{\infty} g_n(\mathbf{x}, \mathbf{y}) \sin \omega_n (t-\tau), \tag{4.8}$$

where n corresponds to an eigenfrequency mode ω_n and the spatial derivative $\partial g_n/\partial x$ is the approximate criterion for evaluating the stability of a combustor configuration [44]. In this section we determine these modal amplitudes.

The time-harmonic Green's function $\hat{G} = \hat{G}(\mathbf{x}, \mathbf{y}, \omega)$ exists in spatial and frequency space. Fourier transformation of the time-domain Green's function $G = G(\mathbf{x}, \mathbf{y}, t, \tau)$ yields the time-harmonic Green's function

$$\hat{G}(\mathbf{x}, \mathbf{y}, \omega) = \frac{1}{2\pi} \int_{-\infty}^{\infty} G(\mathbf{x}, \mathbf{y}, t, \tau) e^{i\omega(t-\tau)} d(t-\tau). \tag{4.9}$$

Similarly, transformation of Equation 4.1 shows that $\hat{G}$ satisfies

$$\left(\nabla^2 + \frac{\omega^2}{c^2}\right)\hat{G} = -\delta(\mathbf{x}-\mathbf{y}), \tag{4.10}$$

in both of the acoustic regions A and C.

Confining the time-harmonic Green's function to one-dimension $\hat{G} = \hat{G}(x_1, y_1, \omega)$ and dividing the hot acoustic region is divided into two parts by a source having position $x_1 = y_1$ from which waves travel forward and backward. Noting the division, the time-harmonic Green's function has the form

$$\hat{G}(x_1, y_1, \omega) = \begin{cases} \hat{G}_{\mathrm{A}} = a \sin k_1(x_1 - L_1) & \text{for } -L_1 < x_1 < X_1 \quad \text{region A} \\ \hat{G}_{\mathrm{C1}} = ce^{ik_2(x_1 - X_2)} + de^{ik_2(x_1 - X_2)} & \text{for } X_2 < x_1 < y_1 \quad \text{region C} \\ \hat{G}_{\mathrm{C2}} = b \sin k_2(x_1 - \bar{L}_2) & \text{for } y_1 < x_1 < \bar{L}_2 \quad \text{region C,} \end{cases} \tag{4.11}$$

where $a = a(y_1, \omega)$, $b = b(y_1, \omega)$, $c = c(y_1, \omega)$, and $d = d(y_1, \omega)$ are constants to be determined, and $k_1 = \omega/c_1$ and $k_2 = \omega/c_2$ are the respective acoustic wave numbers in regions A and C. Replacing ϕ_1 and ϕ_{2+} in Equation 4.7 with Equations 4.11a and 4.11b evaluated at X_1 and X_2, respectively, yields the following two equations

$$\begin{aligned} ic - id &= a\frac{\mathcal{A}_1}{\mathcal{A}_1}\frac{k_1}{k_2}\cos k_1(X_1 - L_1) \\ c + d &= a\frac{\bar{\rho}_1}{\bar{\rho}_2}\left[\sin k_1(X_1 - L_1) - \bar{\ell}\,\frac{\mathcal{A}_1}{\mathcal{A}_1}k_1 \cos k_1(X_1 - L_1)\right]. \end{aligned} \tag{4.12}$$

We can thus express c and d in terms of a,

$$\begin{aligned} c &= a\gamma \\ d &= a\gamma^*, \end{aligned} \tag{4.13}$$

where

$$\gamma = \frac{1}{2}\left[\frac{\rho_1}{\rho_2}\sin\omega\tau_1 + \frac{\rho_1}{\rho_2}\frac{\mathcal{A}_1}{\mathcal{A}_2}\,\bar{\ell}\,k_1\cos\omega\tau_1 - i\frac{\mathcal{A}_1}{\mathcal{A}_2}\frac{k_1}{k_2}\cos\omega\tau_1\right], \tag{4.14}$$

γ^* being the complex conjugate of γ. Expressing Equation 4.11b in terms of γ

$$\hat{G}_{\mathrm{C1}}(x_1, y_1, \omega) = 2a\left[(\mathrm{Re}\,\gamma)\cos k_2(x_1 - X_2) - (\mathrm{Im}\,\gamma)\sin k_2(x_1 - X_2)\right]. \tag{4.15}$$

Constants a and b are determined from conservation of pressure and volume flux across the source position. Namely,

$$\begin{aligned} \hat{G}_{\mathrm{C1}}(y_1, y_1, \omega) - \hat{G}_{\mathrm{C2}}(y_1, y_1, \omega) &= 0 \\ \tfrac{\partial \hat{G}_{\mathrm{C1}}}{\partial x_1}(y_1, y_1, \omega) - \tfrac{\partial \hat{G}_{\mathrm{C2}}}{\partial x_1}(y_1, y_1, \omega) &= 1. \end{aligned}$$

These constants are found to be

$$a(y_1, \omega) = \frac{1}{\omega f_\omega(\omega)}\left[\sin\frac{\omega}{c_2}(x_1 - \bar{L}_2)\right],$$

$$b(y_1, \omega) = \frac{-1}{\omega f_\omega(\omega)}\left[\frac{\rho_1}{\rho_2}\left(\sin\omega\tau_{L1} + \frac{\mathcal{A}_1}{\mathcal{A}_2}\bar{\ell}\,k_1\cos\omega\tau_{L1}\right)\cos k_2(x_1 - X_2) + \frac{\mathcal{A}_1}{\mathcal{A}_2}\frac{c_2}{c_1}\cos\omega\tau_{L1}\sin\frac{\omega}{c_2}(x_1 - X_2)\right].$$

where $f_\omega(\omega)$ is defined in Equation 4.6. Substituting a and b into Equation 4.11, $\hat{G}(x_1, y_1, \omega)$ assumes the form

$$\hat{G}(x_1, y_1, \omega) = \frac{\hat{g}(x_1, y_1, \omega)}{2\omega f_\omega(\omega)}, \tag{4.16}$$

where

$$\hat{g}(x_1, y_1, \omega) = \begin{cases} A(x_1, \omega)C(y_1, \omega) & -L_1 < x_1 < X_1 \\ D(x_1, \omega)C(y_1, \omega) & X_2 < x_1 < y_1 \\ C(x_1, \omega)D(y_1, \omega) & y_1 < x_1 < \bar{L}_2, \end{cases} \tag{4.17}$$

where

$$A(x_1, \omega) = \sin \frac{\omega}{c_1}(x_1 - L_1),$$

$$C(x_1, \omega) = \sin \frac{\omega}{c_2}(x_1 - \bar{L}_2),$$

and

$$\begin{aligned} D(x_1, \omega) =& \frac{\rho_1}{\rho_2}\left(\sin \omega\tau_{L1} + \frac{\mathcal{A}_1}{\mathcal{A}_2}\frac{\bar{\ell}}{c_1}\omega \cos \omega\tau_{L1}\right)\cos \frac{\omega}{c_2}(x_1 - X_2) \\ &+ \frac{\mathcal{A}_1}{\mathcal{A}_2}\frac{c_2}{c_1}\cos \omega\tau_{L1} \sin \frac{\omega}{c_2}(x_1 - X_2). \end{aligned}$$

The time-domain Green's function is obtained by the inverse Fourier transform

$$G(x_1, y_1, t, \tau) = \frac{1}{2\pi}\int_{-\infty}^{\infty} \hat{G}(x_1, y_1, \omega)e^{-i\omega(t-\tau)}d\omega. \tag{4.18}$$

Because the function $f_\omega(\omega)$ is identically zero at the eigenfrequencies of interest, there are singularities at $\omega = \omega_n$ so Cauchy's integral theorem is used to calculate the transform. Before the source time $t = \tau$, the Green's function is, in satisfying causality, zero. After time $t = \tau$, the Green's function is determined by defining a contour in the upper-half plane; the contour begins as $\omega \to -\infty$ and continues along the real axis around each of the the singular frequencies ω_n until approaching $\omega \to +\infty$ where it extends upward in the imaginary axis before returning toward $\omega \to -\infty$. Employing the residue theorem and the symmetry of the frequencies $\omega_{-n} = -\omega_n$, the integral in Equation 4.18 is

restated as

$$G(x_1, y_1, t, \tau) = 2H(t-\tau)\sum_{n=1}^{\infty}\frac{\hat{g}(x_1, y_1, \omega_n)}{\omega_n f'(\omega_n)}\sin\omega_n(t-\tau), \tag{4.19}$$

and by equating this with Equation 4.8, we cast the pressure Green's function modal amplitude g_n in its final form

$$g_n(x_1, y_1) = 2\frac{\hat{g}(x_1, y_1, \omega_n)}{\omega_n f'(\omega_n)}. \tag{4.20}$$

In the following section we evaluate burner stability by numerical calculation of $\partial g_n/\partial x_1$ for varying burner length L.

4.1.3 Burner stability

One of the Limousine burner (Configuration I and II) parameters which we can easily modify to improve stability is the length of region C, the downstream hot acoustic region. In the burner configurations described in Section 3.1, small extensions can be added to its downstream end to change its length; we examine the effect of length on the instabilities.

Figure 4.1 depicts the eigenfrequencies of the first and second mode for Configurations I and II, plotted against the non-dimensionalised burner length L/X_2. We note that each eigenfrequency decreases as the burner length increases, as would be expected in a duct, such as an organ pipe. The spatial derivative (with respect to x_1) of the Green's function modal amplitude is often considered an approximate criteria for evaluating burner stability [44, 64]. Figures 4.2 and 4.3 respective depict the spatial derivative of the Green's function modal amplitude of the first and second mode for Configurations I and II, plotted against the non-dimensionalised burner length L/X_2.

The optimal burner has negative or zero Green's function modal amplitude derivative for all detectable modes ($n = 1, 2, 3$ in this case). Figure 4.2 shows Configuration I has optimal non-

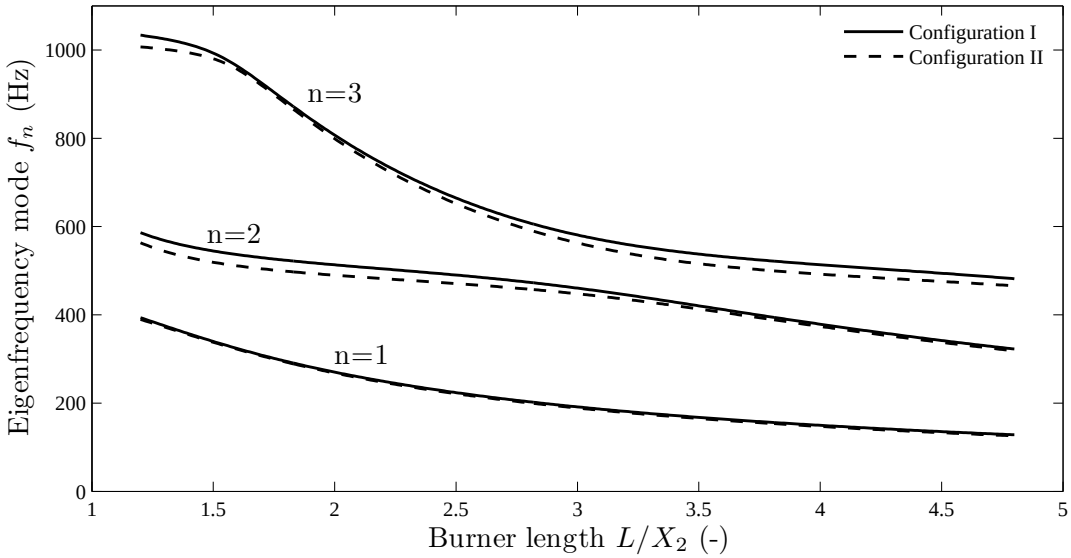

Figure 4.1: Eigenfrequencies of modes $n = 1, 2, 3$ for burner Configurations I and II plotted against non-dimensionalised burner length L/X_2.

dimensionalised length $L/X_2 = 1.75$, where $L = 0.59$ m, because both the first and third mode are zero, while the second is negative. The burner is unstable at all other lengths principally because the first mode is positive. Figure 4.3 shows Configuration II has similar optimal non-dimensionalised length $L/X_2 = 1.76$, where in this configuration $L = 0.60$ m, for the same reason as in Configuration I.

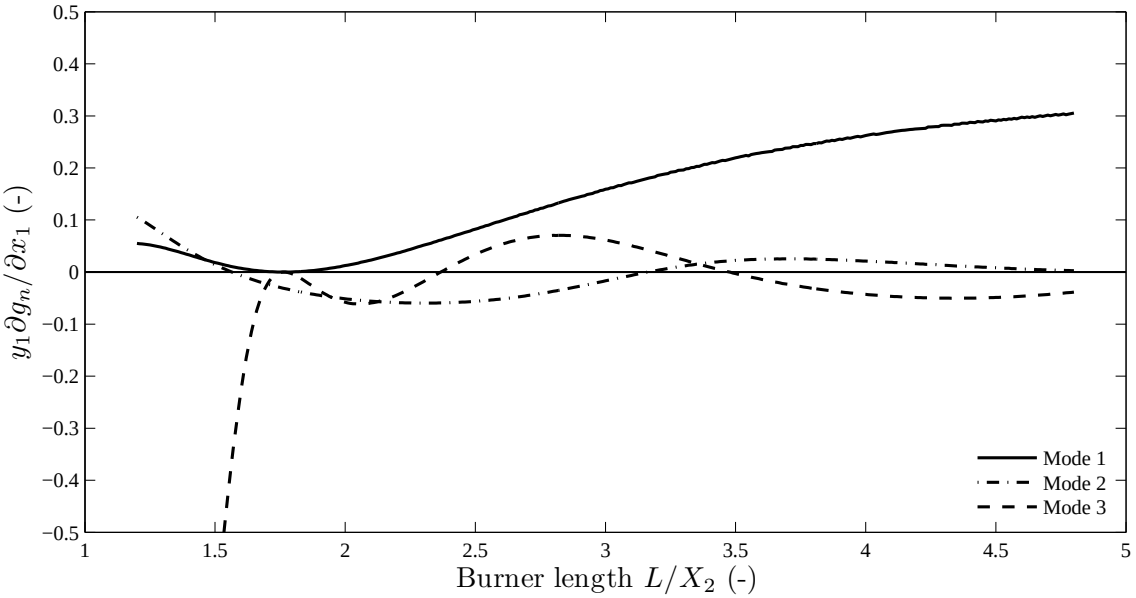

Figure 4.2: Modes $n = 1, 2, 3$ of the Green's function amplitude spatial derivative for burner Configuration I, plotted against non-dimensionalised burner length L/X_2 with observer position $x_1 = L_2$ and source position $y_1 = X_2$.

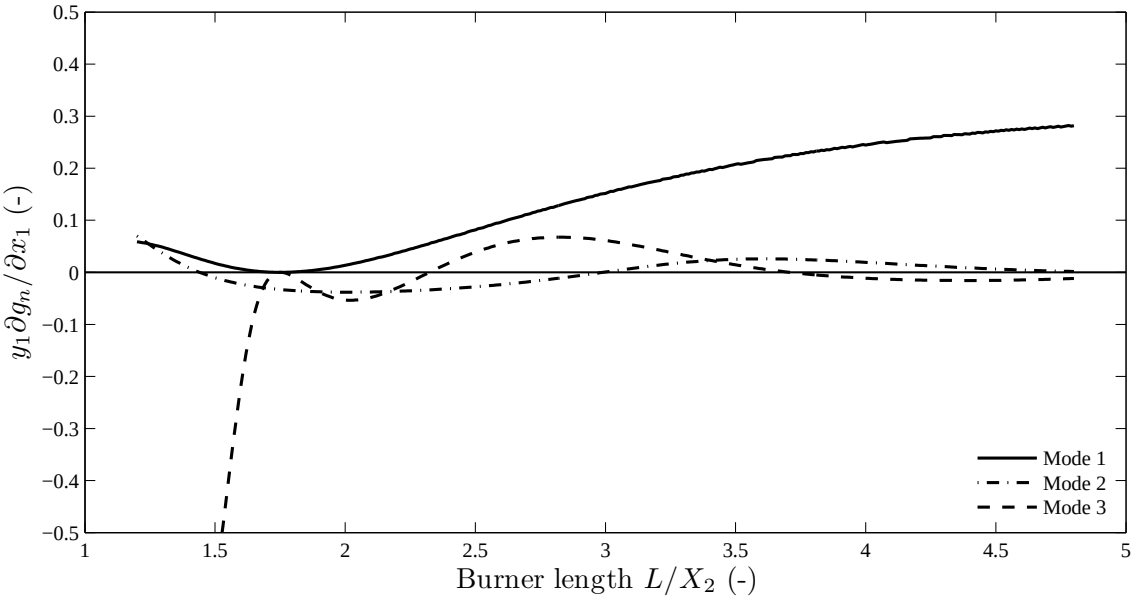

Figure 4.3: Modes $n = 1, 2, 3$ of the Green's function amplitude spatial derivative for burner Configuration II, plotted against non-dimensionalised burner length L/X_2 with observer position $x_1 = L_2$ and source position $y_1 = X_2$.

4.2 The total enthalpy Green's function

The total enthalpy Green's function satisfies Equation 4.1 but determines the solution of the total enthalpy acoustic analogy 2.45. When convolved with source terms involving say vorticity, entropy production, or entropy gradients, we yield the expression for the total enthalpy. In this section we derive the total enthalpy Green's function, in order to formulate an expression for the total enthalpy and subsequently derive the Fant equation in Chapter 6.

The Green's function is solved in the compact approximation, where only plane waves can propagate in regions A and C. Within the compact transition region B, the Green's function reduces to a solution of Laplace's equation

$$G(\mathbf{x}, \mathbf{y}, t, \tau) = \alpha(\tau, x_1, t) + \beta(\tau, x_1, t) Y(\mathbf{y}), \tag{4.21}$$

where $\alpha(\tau, x_1, t)$, $\beta(\tau, x_1, t)$ are constants to be determined and $Y(\mathbf{y})$ is the Kirchoff vector and denotes a velocity potential normalised to have unit speed in region C. $\partial Y/\partial y_n = 0$ on the duct walls and flame-holder, and assumed to satisfy

$$Y(\mathbf{y}) \sim \begin{cases} y_1, & y_1 > \sqrt{\mathcal{A}} \ \text{ in C}, \\ y_1 - \bar{\ell}, & y_1 < -\sqrt{\mathcal{A}} \ \text{ in A}, \end{cases} \tag{4.22}$$

where $\bar{\ell}$ is the constriction 'blockage' length, given by [65, 66]

$$\bar{\ell} = \frac{4h}{\pi} \ln \left[\cos \left(\frac{\pi \ell_f}{2h} \right) \right].$$

Equations 4.21 and 4.22 imply the Green's function $G \equiv G(x_1, y_1, t, \tau)$ must satisfy the following

conditions when $\mathbf{y}$ is in regions A and C

$$\left.\begin{array}{lll} G=\alpha-\bar{\ell}, & \partial G/\partial y_1=\beta, & y_1\to -0 \\ G=\alpha, & \partial G/\partial y_1=\beta, & y_1\to +0 \end{array}\right\}. \tag{4.23}$$

Therefore, we can put

$$\begin{array}{ll} G(x_1,y_1,t,\tau)=-\frac{1}{2\pi}\int\int_{\infty}^{\infty}\frac{\beta(\xi,x_1,t)\cos[k_1(y_1+L_1)]}{k_1\sin(k_1L_1)}\mathrm{e}^{i\omega(\tau-\xi)}d\omega d\xi & \text{for } \mathbf{y} \text{ in A,} \\ G(x_1,y_1,t,\tau)=G_o(x_1,y_1,t,\tau)+\frac{1}{2\pi}\int\int_{\infty}^{\infty}\frac{\beta(\xi,x_1,t)\sin[k_2(y_1+L_2)]}{k_2\sin(k_2L_2)}\mathrm{e}^{i\omega(\tau-\xi)}d\omega d\xi & \text{for } \mathbf{y} \text{ in C,} \end{array} \tag{4.24}$$

where

$$\begin{aligned} G_o(x_1,y_1,t,\tau)= & -\frac{1}{2\pi\mathcal{A}}\int_{-\infty}^{\infty}\{H(x_1-y_1)\cos(k_2y_1)\sin[k_2(x_1-L_2)] \\ & +H(y_1-x_1)\cos(k_2x_1)\sin[k_2(y_1-L_2)]\}\frac{\mathrm{e}^{-i\omega(t-\tau)}}{k_2\cos(k_2L_2)}d\omega, \end{aligned} \tag{4.25}$$

which is the Green's function corresponding to a source located at the flame-holder with the constriction assumed to be closed. The implied Green's function conditions above, $G\to\alpha-\bar{\ell}$, α respectively as $y_1\to\mp 0$, yield consistency conditions which can be used to determine the following functional forms of α and β:

$$\alpha(\tau,x_1,t)=\bar{\ell}\,\beta(\tau,x_1,t)-\frac{1}{2\pi}\int\int_{\infty}^{\infty}\beta(\tau,x_1,t)\frac{\cos(k_1L_1)}{k_1\sin(k_1L_1)}\mathrm{e}^{-i\omega(\xi-\tau)}d\omega d\xi \tag{4.26}$$

$$\begin{aligned} & \bar{\ell}\,\beta(\tau,x_1,t)-\frac{1}{2\pi}\int\int_{\infty}^{\infty}\beta(\tau,x_1,t)\left(\frac{\cos(k_1L_1)}{k_1\sin(k_1L_1)}-\frac{\sin(k_2L_2)}{k_2\cos(k_2L_2)}\right)\mathrm{e}^{-i\omega(\xi-\tau)}d\omega d\xi \\ & \quad =G_o(x_1,0,t,\tau)\equiv-\frac{1}{2\pi\mathcal{A}}\int_{-\infty}^{\infty}\frac{\sin[k_2(x_1-L_2)]}{k_2\cos(k_2L_2)}\mathrm{e}^{-i\omega(\xi-\tau)}d\omega \end{aligned} \tag{4.27}$$

Chapter 5

The burner blockage length

The blockage length quantifies the momentum loss in the Green's function between the upstream and downstream boundaries of the hydrodynamic region (B) in the burner, as in Equation 4.17 and 4.23. The hydrodynamic region can be thought of as a airplug oscillating between the two acoustic regions, having effective length $\bar{\ell}$.

The blockage length $\bar{\ell}$ is defined in terms of a blockage integral, which is derived in Section 5.1 and is dependent on the hydrodynamic flow solution in the respective burner configuration. We propose two different methods of determining this hydrodynamic flow solution. Both methods are applicable to the combustor Configurations I and II described in Section 3.1. The first method (Method I) determines the hydrodynamic flow solution from Laplace's equation using a computational mesh defined within a plane of the combustor geometries. Additionally, using this methodology, we quantify the effect of flow splitters on aeroacoustic calculations. Method I applied to Configuration I is described in Sections 5.2, 5.3. The second method (Method II) is more sophisticated and determines the hydrodynamic flow solution by transformation of the burner geometry into a simple flat plate for which the hydrodynamic flow solution is known analytically. Method II is applied to Configurations I

and II because Method II is more sophisticated and developed later in the project; it also coincided with the change in the burner used in experiments. Method II is also applied to the idealised geometry of Section 3.2; however, the transformation is determined analytically. Method II applied to Configuration III is described in Section 5.6.

5.1 The blockage integral

The blockage integral is determined for Configurations I and II from the velocity potential of the hydrodynamic flow solution in the burner configuration. The blockage integral defining $\bar{\ell}$ is derived starting with pressure momentum-loss equation 4.7

$$p_2 - p_1 = \rho_1 \frac{\partial \phi_{2-}}{\partial t} - \rho_1 \frac{\partial \phi_1}{\partial t} = \rho_1 \bar{\ell} \frac{\partial \phi_{2-}}{\partial x_1}. \tag{5.1}$$

Velocity potentials ϕ near the hydrodynamic region are defined in Equation 4.4 where

$$\begin{aligned} \phi(x_1) &= \alpha + \beta \tfrac{\mathcal{A}_2}{\mathcal{A}_1}(x_1 - (X_1 - L_1)) \text{ for } x_1 \approx X_1, \\ \phi(x_1) &= \alpha + \beta(x_1 - (X_2 - \bar{L}_2)) \text{ for } x_1 \approx X_2, \end{aligned} \tag{5.2}$$

where $x_1 = -L_1$ is the position of the closed duct entrance plane, and $x_1 = \bar{L}_2$ is just beyond the open duct exit, accounting for a small acoustic end correction. Substitution of Equation 5.1 into ϕ yields

$$\bar{\ell} = L_1 - \frac{\mathcal{A}_2}{\mathcal{A}_1} \bar{L}_2. \tag{5.3}$$

Considering the limits of the velocity potential φ^* as $x_1 \to \pm\infty$, we have from the ϕ definition 5.2

as $x_1 \to +\infty$

$$\varphi^*(x_1) \to \begin{cases} \int_{X_2}^{\infty} \frac{\partial \varphi^*}{\partial \xi} d\xi + \varphi^*(X_2) & \text{(Identity)}, \\ \int_{X_2}^{x_1} d\xi + \bar{L}_2 & \text{(From Equation 4.4b)}. \end{cases} \tag{5.4}$$

Similarly, as $x_1 \to -\infty$

$$\varphi^*(x_1) \to \begin{cases} -\int_{-\infty}^{X_2} \frac{\partial \varphi^*}{\partial \xi} d\xi + \varphi^*(X_2) & \text{(Identity)}, \\ \frac{\mathcal{A}_2}{\mathcal{A}_1} \int_{X_2}^{x_1} d\xi + \frac{\mathcal{A}_2}{\mathcal{A}_1}(X_2 - X_1 + L_1) & \text{(From Equation 4.4c)}. \end{cases} \tag{5.5}$$

Matching formulations 5.4 and 5.5 at each respective limit $x_1 \to \pm\infty$ yields the following two equations

$$\begin{aligned} \bar{L}_2 &= \int_{X_2}^{\infty} \left(\frac{\partial \varphi^*}{\partial \xi} - 1 \right) d\xi + \varphi^*(X_2), \\ \frac{\mathcal{A}_2}{\mathcal{A}_1}(X_2 - X_1 + L_1) &= \int_{-\infty}^{X_2} \left(\frac{\partial \varphi^*}{\partial \xi} - \frac{\mathcal{A}_2}{\mathcal{A}_1} \right) d\xi + \varphi^*(X_2). \end{aligned} \tag{5.6}$$

The substitution of the difference of these equations into Equation 5.3 yields the blockage integral

$$\bar{\ell} = \int_{X_2}^{\infty} \left(\frac{\partial \varphi^*}{\partial \xi} - 1 \right) d\xi + \int_{-\infty}^{X_2} \left(\frac{\partial \varphi^*}{\partial \xi} - \frac{\mathcal{A}_2}{\mathcal{A}_1} \right) d\xi + \frac{\mathcal{A}_2}{\mathcal{A}_1}(X_2 - X_1). \tag{5.7}$$

5.2 The blockage length by solution to Laplace's equation

The expression for the blockage integral 5.7 is initially evaluated numerically in Method I from the velocity potential of the hydrodynamic flow determined by the relation between the velocity potential φ^* and stream function ψ^*, given by

$$\frac{\partial \varphi^*}{\partial x_1} = \frac{\partial \psi^*}{\partial x_2}. \tag{5.8}$$

Stream-function values are determined assuming the flow is incompressible and irrotational. The

velocity potential and the stream function satisfy Laplace's equation for the respective incompressible or irrotational flow. The stream function is solved numerically using finite difference methods.

5.2.1 Finite-difference methods

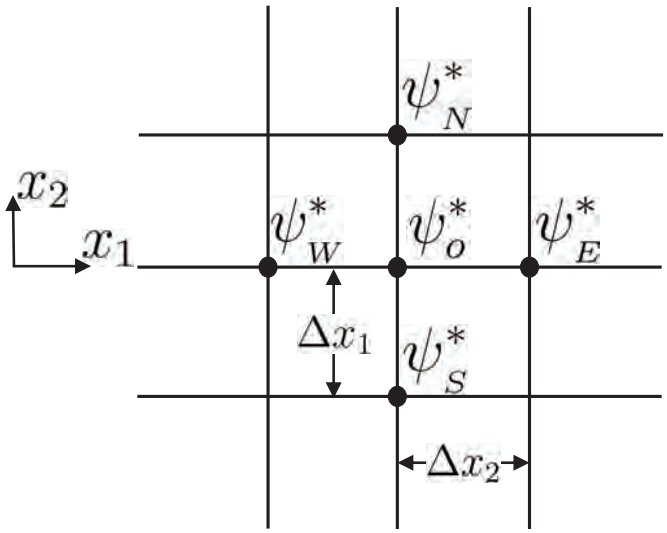

Figure 5.1: Schematic of a generic computational mesh.

Laplace's equation for the stream function $\nabla^2\psi^* = 0$ in two-dimensions is simply

$$\frac{\partial^2\psi^*}{\partial x_1^2} + \frac{\partial^2\psi^*}{\partial x_2^2} = 0, \tag{5.9}$$

for which we devise a finite difference scheme in order to solve. In this scheme, the continuous geometry of the burner walls is divided into a discrete set of points collectively called a mesh: the distance between neighboring points is Δx_1 in the x_1-direction and Δx_2 in the x_2-direction. This discrete scenario is depicted in Figure 5.1.The discrete formulation of Laplace's equation 5.11 is determined using well-known, finite-difference equations. For example, the first and second derivatives of the

function $g(\xi)$ have the respective finite-difference approximations.

$$\begin{aligned} \frac{dg(\xi)}{d\xi} &\approx \frac{g(\xi+\Delta\xi)-g(\xi-\Delta\xi)}{2\Delta\xi}, \\ \frac{d^2g(\xi)}{d\xi^2} &\approx \frac{g(\xi+\Delta\xi)-2g(\xi)+g(\xi-\Delta\xi)}{\Delta^2\xi}, \end{aligned} \tag{5.10}$$

where $\Delta\xi$ is the distance between neighboring points in the ξ-direction. $\psi^*_{_N}$, $\psi^*_{_S}$, $\psi^*_{_W}$, $\psi^*_{_E}$ respectively define mesh points above, below, left, and right (North, South, West, and East) of the central point ψ^*_o. The solution of Laplace's equation is numerically determined by performing several hundred iterations of the numerical formulation of Laplace's equation. The point ψ^*_o is determined in successive iterations by the formula:

$$\psi^*_o = C_{_\Delta}\left[\frac{1}{\Delta x_1^2}(\psi^*_{_E}+\psi^*_{_W})+\frac{1}{\Delta x_2^2}(\psi^*_{_N}+\psi^*_{_S})\right], \tag{5.11}$$

where $C_{_\Delta} \equiv \frac{1}{2}\frac{1}{\frac{1}{\Delta x_1^2}+\frac{1}{\Delta x_2^2}}$. Employing the symmetry, the mesh is defined between the centerline $x_2 = 0$ and the upper wall $x_2 = h(x_1)$. The mesh is not bounded at either side at the true ends of the burner; it is, rather, bounded such that its ends are sufficiently far from the hydrodynamic region that the flow can be regarded as one-dimensional at say L_1^* and L_2^* for the entrance and exit respectively; this in order to reduce computing time. Streamline boundary conditions are initially defined on the four boundaries of the mesh: the centerline, the wall of the burner, and the sides at L_1^* and L_2^*. These boundary conditions must satisfy the following two conditions:

$$\begin{aligned} \frac{\partial\varphi^*}{\partial x_1} &\rightarrow 1 \text{ as } x_1 \rightarrow \infty, \\ \frac{\partial\varphi^*}{\partial x_1} &\rightarrow \frac{\mathcal{A}_2}{\mathcal{A}_1} \text{ as } x_1 \rightarrow -\infty, \end{aligned} \tag{5.12}$$

for normalisation and mass conservation respectively. The numerical approximation of the stream-

function value at the burner exit is determined from Equation 5.8, 5.10, and 5.12 and is

$$\frac{\partial \psi^*}{\partial x_2} \approx \frac{\psi^*(x_1, x_2 + \Delta x_2) - \psi^*(x_1, x_2 - \Delta x_2)}{2\Delta x_2} = 1.$$

The stream function is linear so the finite difference derivative can then be expanded to extend between the stream-function values at the burner wall and the centerline,

$$\psi^*(x_1, 0 + k\Delta x_2) - \psi^*(x_1, 0) = k\Delta x_2,$$

where $k = h(L_2^*)/\Delta x_2$ is the number of cells between the centerline and upper boundary of the burner. Defining the stream-function value at the lower boundary as $\psi^*(x, 0) \equiv 0$, the upper boundary is constant $\psi^*(x_1, h(x_1)) = h(L_2^*) = h_2$. At L_1^* and L_2^*, the stream-function values transition linearly between the value at the centerline 0 and the value at the upper boundary h_2. The initial conditions are irrelevant to the solution of the problem provided sufficient iterations are performed; the stream-function values within the boundaries were arbitrarily chosen to have initial value $\psi^*(x_1, x_2) = 0$.

The boundary conditions are defined as above and remain fixed during all iterations. The values ψ_o^* at each non-boundary point in the mesh is determined for each successive iteration. Iterations stop once values of ψ_o^* converge and do not sufficiently change between successive iterations. Specifically, letting $\psi_{i,j}^n$ denote the value of ψ^* at $(i = x_1/\Delta x_1, j = x_2/\Delta x_2)$ after n iterations, and ϵ being a prescribed threshold value, the computation stops when

$$\sum_i \left(\sum_j \left(\psi_{i,j}^n - \psi_{i,j}^{n-1} \right)^2 \right) \leq \epsilon. \tag{5.13}$$

Figure 5.2 depicts the burner hydrodynamic streamlines in Configuration I, where the prescribed

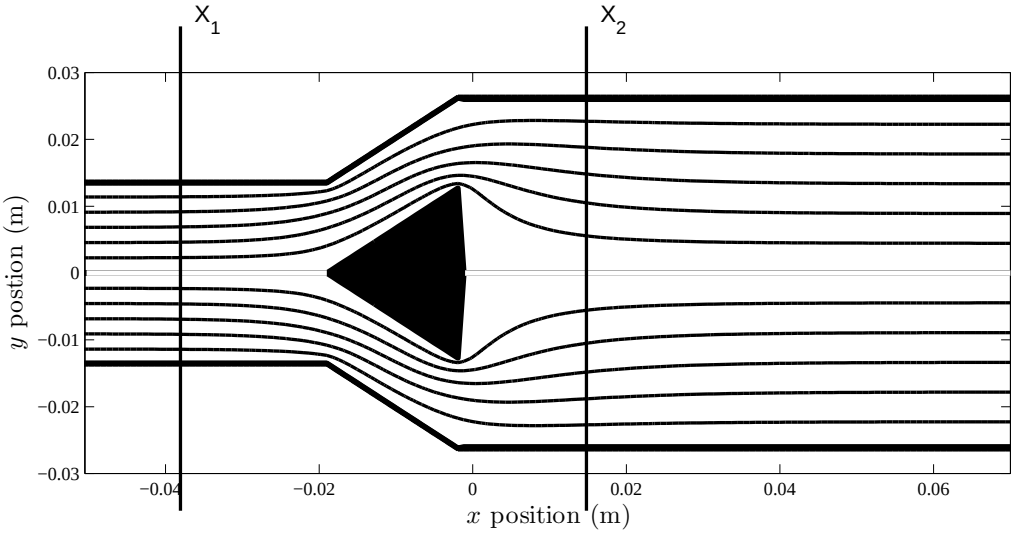

Figure 5.2: Illustration of the hydrodynamic streamlines in burner Configuration I.

threshold is $\epsilon = 10^{-8}$.

5.3 The effect of splitter plates

In past experimental combustor configurations, it has been the practice to place splitter plates half-way between the flame-holder and the burner wall. It is thought that these have the effect of preventing the sides of the burner from over-heating by splitting the flow into one which encounters the flame and one which does not. We examine the effect of splitter plates, predicting how its values changes in their presence.

We first determine the value of the hydrodynamic streamlines in the absence of splitter plates, as in Section 5.2. The splitter plates are then assigned a specific stream-function value determined by the condition that there is zero circulation $\Gamma = \oint_C \mathbf{v} \cdot d\mathbf{x}$ around them. This methodology is illustrated using the example of a horizontal flat plate.

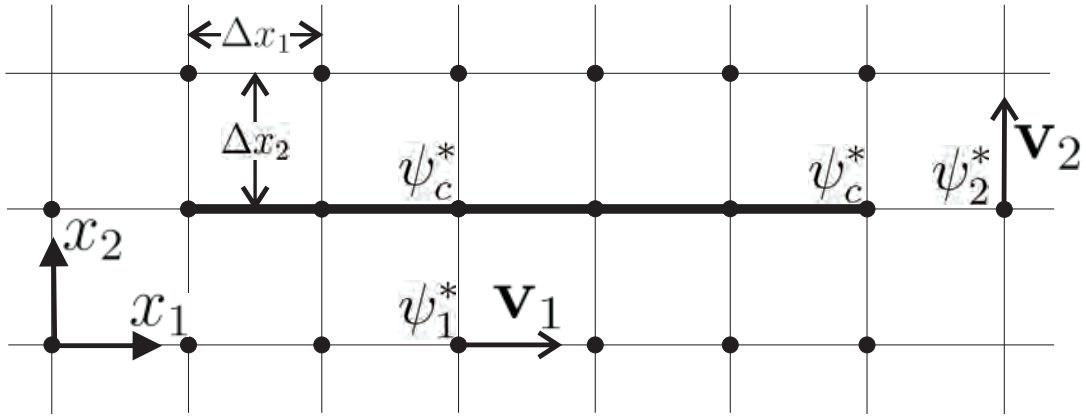

Figure 5.3: Schematic of the flat plate used to calculate the circulation around the splitter plates.

We choose to illustrate the calculation of the stream-function value using a flat plate rather than the angled splitter plates due to the simplicity of the nomenclature involved in defining the normal direction. The flat plate depicted in Figure 5.3 is within a uniform square mesh having node-spacing Δx_1 in the x_1 direction and Δx_2 in the x_2 direction. The flat plate, like the splitter plates, has a single stream-function value ψ_c which is determined by the zero-circulation condition. All of the nodes surrounding the flat plate have stream-function value determined by the numerical solution to Laplace's equation in the plate's absence, for example ψ_1 and ψ_2. From the stream-function definition, velocity $\mathbf{v}_1 = v_{1,x_1} = \partial\psi/\partial x_2 \approx (\psi_1 - \psi_c)/\Delta x_2$, and similarly, velocity $\mathbf{v}_2 = v_{2,x_2} = \partial\psi/\partial x_1 \approx (\psi_2 - \psi_c)/\Delta x_1$. The numerically-determined circulation is the sum of these velocities along the top, bottom, and sides of the flat plate. Defining $\Delta = \Delta x_1 = \Delta x_2$, the circulation,

$$\Gamma = \oint_C \mathbf{v} \cdot d\mathbf{x} \approx \sum_{i=1}^{N} \frac{\psi_i - \psi_c}{\Delta} \equiv 0, \tag{5.14}$$

is defined as zero and where N is the number of nodes surrounding the plate. The flat plate therefore

has the stream-function value

$$\psi_c = \frac{1}{N}\sum_{i=1}^{N}\psi_i. \tag{5.15}$$

The identical method is easily applied to the burner splitter plates by simply rotating the chosen coordinate axis. Stream-function values are finally determined in the presence of the splitter plates by fixing the stream-function values at mesh points coincident with the splitter plates to those obtained from Equation 5.15.

Hydrodynamic streamlines are depicted in Figures 5.2 and 5.4 for respective burner Configuration I without and with splitter plates. Both figures show that the flow converges to one-dimensional in each case at identical X_1 and X_2 positions. For Configuration I, in all numerical simulations $X_1 = -0.038\,\mathrm{m}$ and $X_2 = 0.015\,\mathrm{m}$.

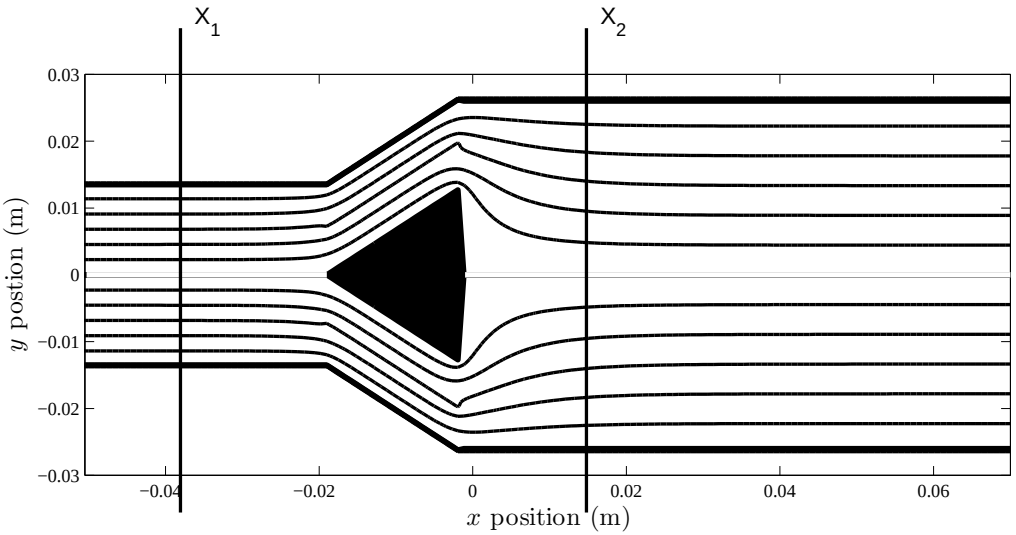

Figure 5.4: Illustration of the hydrodynamic streamlines in burner Configuration I with splitter plates.

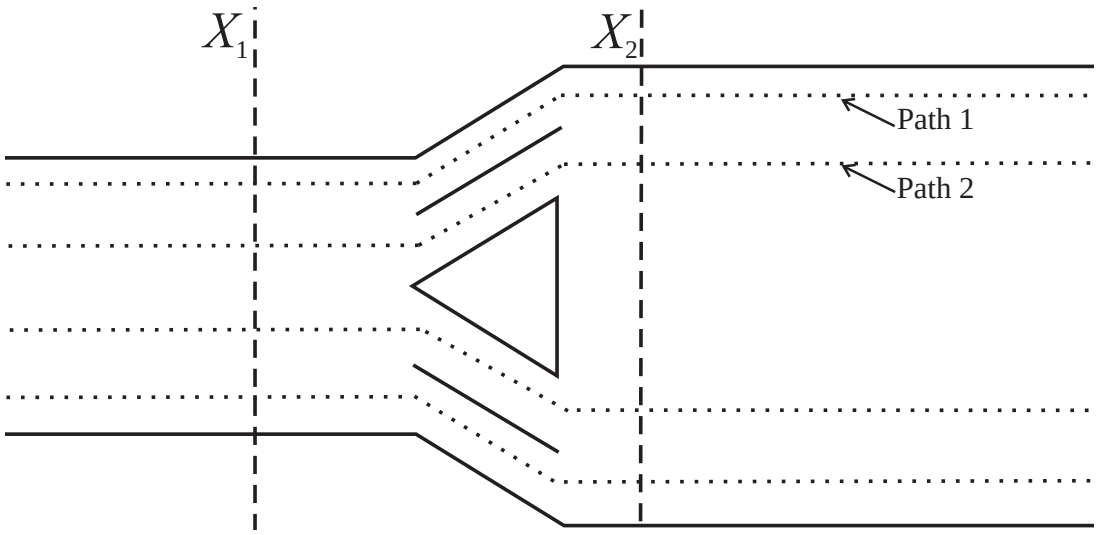

Figure 5.5: Illustration of the integration paths used for calculating $\bar{\ell}$ in burner Configuration I with splitter plates.

In application to the splitter plates, formula 5.7 for the blockage length,

$$\bar{\ell} = \int_{X_2}^{\infty} \left(\frac{\partial \varphi^*}{\partial \xi} - 1 \right) d\xi + \int_{-\infty}^{X_2} \left(\frac{\partial \varphi^*}{\partial \xi} - \frac{\mathcal{A}_2}{\mathcal{A}_1} \right) d\xi + \frac{\mathcal{A}_2}{\mathcal{A}_1} (X_2 - X_1) ,$$

is limited only by the integration path which must be a straight line. In burner Configuration I with the splitter plates, there are no straight paths between each end of the burner and therefore a straight line cannot be used. We therefore must reformulate the blockage integral to allow for a two-dimensional path. The generalised blockage integral is

$$\bar{\ell} = \int_{X_2}^{\infty} \nabla (\varphi^* - x) \cdot d\mathbf{s} + \int_{-\infty}^{X_2} \nabla \left(\varphi^* - \frac{\mathcal{A}_2}{\mathcal{A}_1} x \right) \cdot d\mathbf{s} + \frac{\mathcal{A}_2}{\mathcal{A}_1} (X_2 - X_1) . \tag{5.16}$$

The two paths are chosen for integration in order to verify the accuracy of the method; they are depicted in Figure 5.5. Path 1 is located half-way between the splitter plate and the burner wall.

Table 5.1: The burner blockage length for burner Configuration I, with and without splitter plates

Configuration I	Blockage length $\bar{\ell}$
Without splitter plates	0.095 m
With splitter plates	0.101 m

From the ends of the splitter plate, it extends as a straight line in the upstream and downstream region. Path 2 is very similar to Path 1 except it is located half-way between the burner and the splitter plate. The blockage integral values obtained by integration along each of the two paths are identical.

The effective blockage length $\bar{\ell}$ in each case is calculated using numerical integration of Equation 5.7 having Legendre quadrature. Blockage length values for Configuration I, without and with splitter plates, are shown in Table 5.1. For the Configuration I burner without splitter plates, $\bar{\ell} = 0.095$ m, which is identical to the result obtained using the one-dimensional integral equation 5.3. In the burner with splitter plates, $\bar{\ell} = 0.101$ m, which is only 6% larger than that without the splitter plates. We can therefore conclude that the addition of splitter plates does not sufficiently affect the analytic model of the two-dimensional burner and they can be neglected in analytic models.

5.4 The Schwarz-Christoffel transformation

A straight-sided polygon in the z-plane can be mapped into the transformed space on the upper half ζ-plane, such that the sides of the polygon are transformed into the real ζ-axis ξ by means of the formula [67–69]:

$$\frac{dz}{d\zeta} = K \prod_{n=1}^{N} (\zeta - \xi_n)^{\alpha_n/\pi - 1} \tag{5.17}$$

for a polygon with N angular points, where α_n and ξ_n ($\xi_n < \xi_{n+1}$) are the respective internal angles and points on the real ζ-axis ($\zeta_n = \xi_n + \eta i$) corresponding to the ordered angular points $z_n = x_{1,n} + x_{2,n} i$ in the z-plane. K is a complex constant and determines orientation and size. A transformation containing four angular points is depicted in Figure 5.6. The perimeter of the polygon maps onto the real ζ-axis so that one of the points ξ_n has location $\zeta = \infty$; in this case, the factor $(\zeta - \xi_n)^{\alpha_n/\pi - 1}$ is omitted from the right-hand side of Equation 5.17.

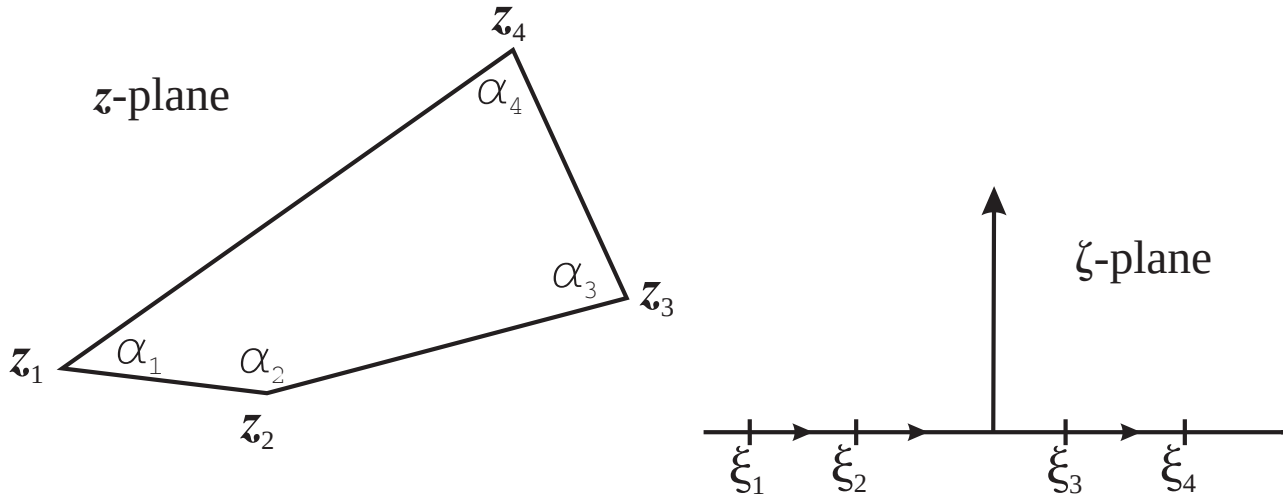

Figure 5.6: Illustration of a polygon and the corresponding Schwarz-Christoffel transformation.

The integral form of Equation 5.17,

$$z(\zeta) = K \int_{\zeta=\xi} \prod_{n=1}^{N} (\zeta' - \xi_n)^{\alpha_n/\pi - 1} d\zeta' + L, \tag{5.18}$$

introduces an integration constant L, which determines the position of the polygon in the z-plane. In any transformation, three ξ_n parameters may be prescribed arbitrarily, obeying the condition $\xi_i < \xi_{i+1}$.

5.4.1 An example with one unknown

Consider the duct depicted in the z-plane of Figure 5.7: it has height h which jumps from h_1 to h_2. It contains the respective corners $z_1 = +\infty + ih_2$, $z_2 = ih_2$, $z_3 = ih_1$, $z_4 = -\infty + ih_1$, $z_{4'} = -\infty$, and $z_5 = +\infty$. In this geometry, Equation 5.17 takes the form

$$\frac{dz}{d\zeta} = K\frac{(\zeta - \xi_3)^{1/2}}{(\zeta - \xi_4)(\zeta - \xi_2)^{1/2}}. \tag{5.19}$$

The constants ξ_3 and ξ_4 are chosen to coincide with $\zeta = -1$ and $\zeta = 0$, respectively. The constant

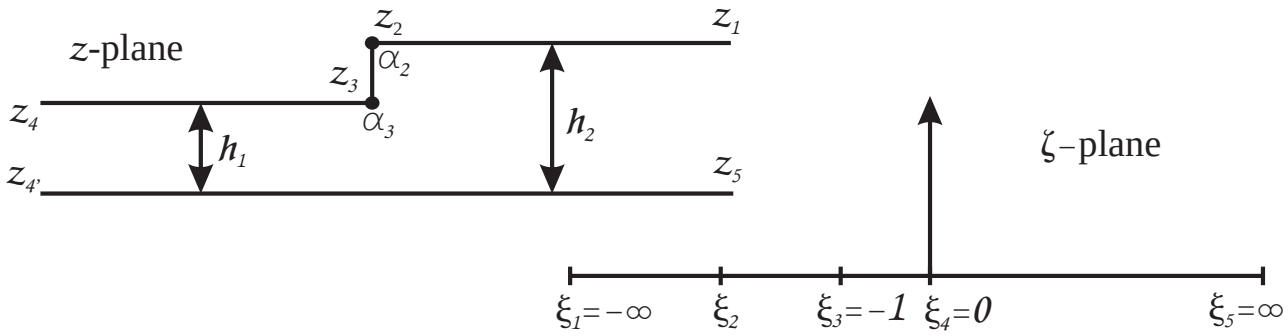

Figure 5.7: Illustration of a duct of varying cross-sectional area and the corresponding Schwarz-Christoffel transformation.

K is determined by integrating around the singularity at $\zeta = \xi_4$ found in the integral form of Equation 5.19. Using residue methods discussed in [70], we evaluate the integral between $\xi_{4'}$ and ξ_4 and equated to the corresponding displacement in the z-plane, namely,

$$z_4 - z_{4'} = h_1 i = K\int_{\zeta=\xi_4} \frac{(\zeta' + 1)^{1/2}}{\zeta'(\zeta' - \xi_2)^{1/2}} d\zeta' = K\frac{\pi}{\sqrt{\xi_2}}, \tag{5.20}$$

yielding $K = \frac{h_1 i}{\pi}\sqrt{\xi_2}$. The constant ξ_2 is determined similarly; however, the integral is evaluated between ξ_2 and ξ_3, and equate it to the corresponding displacement in the z-plane, explicitly,

$$z_3 - z_2 = (h_1 - h_2)i = K \int_{\xi_2}^{\xi_3=-1} \frac{(\zeta' + 1)^{1/2}}{\zeta'(\zeta' - \xi_2)^{1/2}} d\zeta' = h_1(i + \sqrt{\xi_2}), \tag{5.21}$$

resulting in $\xi_2 = -\left(\frac{h_2}{h_1}\right)^2$. The results from Equations 5.20 and 5.21 lead to the final form of the Schwarz-Christoffel transformation for the duct:

$$\frac{dz}{d\zeta} = \frac{h_2}{\pi} \frac{\sqrt{\zeta + 1}}{\zeta\sqrt{\zeta + \left(\frac{h_2}{h_1}\right)^2}}. \tag{5.22}$$

This method is applied to the more complicated geometry of burner Configurations I and II in order to derive the corresponding Schwarz-Christoffel transformation.

5.5 The blockage length by transformation

Blockage-length calculation Method II consists of mapping Configurations I and II burners (in the z-plane) onto the upper half ζ-plane Formula 5.17. The burner and its transformation into the ζ-plane are depicted in Figure 5.8.

Equation 5.17 for Configurations I and II respectively takes the form

$$\frac{dz}{d\zeta} = K \frac{(\zeta - \xi_3)^{1/6}(\zeta - \xi_6)^{2/3}}{(\zeta - \xi_2)^{1/6}(\zeta - \xi_4)(\zeta - \xi_5)^{1/6}(\zeta - \xi_7)^{1/2}}. \tag{5.23}$$

$$\frac{dz}{d\zeta} = K \frac{(\zeta - \xi_3)^{1/2}(\zeta - \xi_6)^{2/3}}{(\zeta - \xi_2)^{1/2}(\zeta - \xi_4)(\zeta - \xi_5)^{1/6}(\zeta - \xi_7)^{1/2}}. \tag{5.24}$$

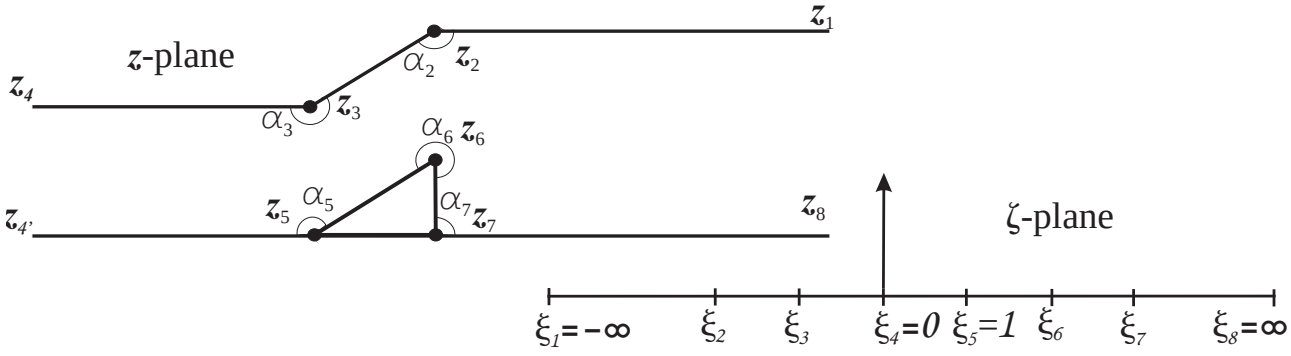

Figure 5.8: Illustration of the upper-half Configuration I burner and the corresponding Schwarz-Christoffel transformation.

The constants in each configuration ξ_4 and ξ_5 are chosen to coincide with $\zeta = 0$ and $\zeta = 1$, respectively. The integral form of Equations 5.23 and 5.24 is respectively

$$z(\zeta) = K \int_{\zeta} F(\zeta')d\zeta' = K \int_{\zeta} \frac{(\zeta' - \xi_3)^{1/6}(\zeta' - \xi_6)^{2/3}}{\zeta'(\zeta' - \xi_2)^{1/6}(\zeta' - 1)^{1/6}(\zeta' - \xi_7)^{1/2}} d\zeta', \tag{5.25}$$

$$z(\zeta) = K \int_{\zeta} F(\zeta')d\zeta' = K \int_{\zeta} \frac{(\zeta' - \xi_3)^{1/2}(\zeta' - \xi_6)^{2/3}}{\zeta'(\zeta' - \xi_2)^{1/2}(\zeta' - 1)^{1/6}(\zeta' - \xi_7)^{1/2}} d\zeta', \tag{5.26}$$

where the integrand on the right-hand side of Equations 5.25 and 5.26 is defined as $F(\zeta)$. The four unknowns in Equations 5.25 and 5.26 present a problem that cannot be solved analytically due to the

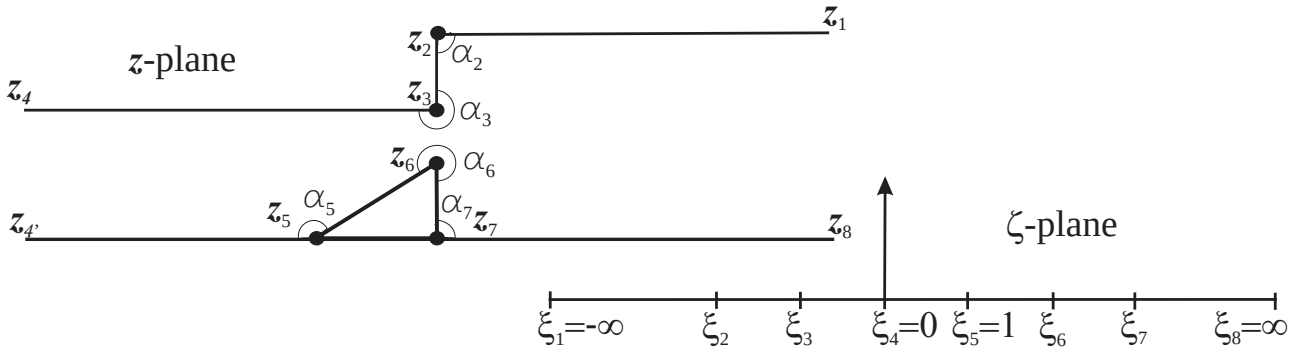

Figure 5.9: Illustration of the upper-half Configuration II burner and the corresponding Schwarz-Christoffel transformation.

number of parameters ξ_i involved. [71, 72] present a numerical method for calculating the constants in the Schwarz-Christoffel transformation of a polygon. The method consists of defining an error S as the sum of the squares of the difference between the ζ-plane integral and the z-plane displacement for two consecutive points. Specifically,

$$S = \sum_{n=1}^{N-1} \left| K \int_{\zeta=\xi_n}^{\zeta=t_{\xi+1}} F(\zeta')d\zeta' - (z_{n+1} - z_n) \right|^2, \tag{5.27}$$

for all n corresponding to ξ_n having finite position in the ζ-plane, where N is the total number of points. In the example with only one unknown, described in Section 5.4.1, the error is exactly zero because the displacement in the z-plane is identical as the integral in the ζ-plane; however, when there is more than one unknown, the error cannot be exactly zero so we search for an error $S < 10^{-6}$.

5.5.1 Gauss-Jacobi quadrature

It is essential when evaluating integrals like 5.25 to devise a well-behaved numerical integration scheme due to the singular nature of $F(\zeta)$. For example, if integrating between ξ_3 and ξ_4 in Equation 5.25, a zero would be encountered at ξ_3 and a first-order pole would be encountered at ξ_4. Given the Schwarz-Christoffel transformation is defined such that $\xi_i < \xi_{i+1}$, singularities and zeros exist only at the limits of integration, not between them.

The Gauss-Jacobi quadrature addresses this problem; [73, 74] approximate an integral having a singular integrand using Gaussian integration, namely,

$$\int_{-1}^{1} (1+x)^\beta (1-x)^\gamma f(x)dx \simeq \sum_{j=1}^{M} W_j f(x_j), \tag{5.28}$$

where M is the chosen number of abscissae x_i and weights W_i. The segment $\{\xi_i, \xi_{i+1}\} \in \xi$ is transformed to the segment $\{-1, 1\} \in x$ using the linear transformation

$$\xi = \frac{1}{2}\left[\xi_i + \xi_{i+1} + x(\xi_{i+1} - \xi_i)\right]. \tag{5.29}$$

Rewriting the integrand function 5.25 and 5.26,

$$\int_{\zeta=\xi_i}^{\zeta=\xi_{i+1}} F(\zeta')d\zeta' = \int_{\zeta=\xi_i}^{\zeta=\xi_{i+1}} \prod_{k=i}^{i+1} (\zeta' - \xi_k)^{\alpha_k/\pi - 1} G(\zeta')d\zeta', \tag{5.30}$$

the formula is separated into a function which is well-behaved within the segment $\{\xi_i, \xi_{i+1}\}$, $G(\zeta)$, and a function which is either singular or zero at the limits. We write the Gauss-Jacobi formulation of the integral as

$$\int_{\zeta=\xi_i}^{\zeta=\xi_{i+1}} F(\zeta')d\zeta' = C\int_{-1}^{1} (1+x)^{\beta}(1-x)^{\gamma} G(x)dx \simeq C\sum_{j=1}^{M} W_j G(x_j), \tag{5.31}$$

where $\beta = \frac{\alpha_i}{\pi} - 1$, $\gamma = \frac{\alpha_{i+1}}{\pi} - 1$, and $C = (-1)^{\gamma}\left[\frac{1}{2}(\xi_{i+1} - \xi_i)\right]^{\beta+\gamma+1}$.

The abscissae x_j are estimated using the recursion relation

$$x_j \simeq 3x_{j+1} - 3x_{j+2} + x_{j+3}.$$

Values for x_M, x_{M-1}, x_{M-2} are required in order to initiate this recursive method; they are estimated using known formulae which are functions of M, β, and γ. All estimates, whether initially obtained using a formula (i.e. x_M, x_{M-1}, x_{M-2}) or using the recursive relation above, are then refined using the Newton-Raphson method to converge upon the exact zero of the Jacobi polynomial $P_M^{\beta,\gamma}(x_j)$.

Once a precise value is obtained for an abscissa x_j, the corresponding weight W_j is calculated using the formula

$$W_j = \frac{2M+\beta+\gamma+2}{M+\beta+\gamma+1}\frac{\Gamma(M+\beta+1)\Gamma(M+\gamma+1)}{\Gamma(M+\beta+\gamma)\Gamma(M+2)}\frac{2^{\beta+\gamma}}{P_M'^{\beta,\gamma}(x_j)P_{M+1}^{\beta,\gamma}(x_j)},$$

where $P'(\cdot)$ denotes the derivative of $P(\cdot)$ with respect to x_j, and $\Gamma(\cdot)$ is the *Gamma function*. The quadrature method has proven resilient and is used to determine all unknown ξ_i values.

5.5.2 Minimising the error

When a function is continuous, smooth and non-singular, one typically minimises an error or converges upon an unknown value using a gradient-dependent method such as Newton-Raphson. However, when calculating the Schwarz-Christoffel transformation, gradient methods are not practical because the gradients are either highly singular or zero at the points of interest by definition of the Schwarz-Christoffel transformation. It is therefore essential to employ a convergence scheme in which knowledge of the gradients is not necessary.

The chosen method of convergence is called the *simplex* method [75–79]. A simplex is the N-dimensional analogue to a triangle containing $N+1$ independent points in euclidean space. The simplex must contain $N+1$ points, N being the number of dimensions in the function. It is most-easily described and depicted using one or two-dimensional functions. Figure 5.12 illustrates a simplex for two numerical examples described in Section 5.5.3.

For the Rijke burner transformation, the simplex is initiated at step $P=1$ with $N+1$ arbitrary points at $\{\mathbf{X}_{n=n_1}, \mathbf{X}_{n=n_2}, ..., \mathbf{X}_{n=N+1}\}$, it then replaces the point having the largest error $S\left(\mathbf{X}_{n=n_j}^{P=1}\right)$ with the dimensionally-*opposite* point. If in the following step $P=2$, the dimensionally-opposite

point $\mathbf{X}_{n=n_j}^{P=2}$ corresponds to an error S which is smaller than in the previous step, the procedure will do either one of the following. If the error at a different point in the simplex $S\left(\mathbf{X}_{n\neq n_j}^{P=2}\right)$ is greater than $S\left(\mathbf{X}_{n=n_j}^{P=2}\right)$, $\mathbf{X}_{n\neq n_j}^{P=2}$ is replaced with the dimensionally-opposite point $\mathbf{X}_{n\neq n_j}^{P=3}$ in the following step; however, if $S\left(\mathbf{X}_{n=n_j}^{P=2}\right)$ is still greater than the error at any other point, the simplex expands in the direction between $\mathbf{X}_{n=n_j}^{P=1}$ and $\mathbf{X}_{n=n_j}^{P=2}$. If replacement leads to an error which is smaller than any other, the simplex contracts. This procedure continues for several iterations until converging upon the chosen threshold, in this case $S < 10^{-6}$.

5.5.3 Streamlines of a hydrodynamic source flow

In order to validate any calculated Schwarz-Christoffel transformation or determine the blockage length $\bar{\ell}$, we evaluate the streamlines of the potential flow originating from a source at negative infinity in the z-plane. In burner Configuration I and II the source has strength $q = h_1 U_1$, where h_1 and U_1 are the respective height and velocity in the upstream region. The source is translated into the ζ-plane and chosen to coincide with $\zeta^- = 0$ in all examples discussed. By definition of the Schwarz-Christoffel transformation, we restrict our interest to the upper-half ζ-plane. The complex potential w is defined as $\varphi + i\psi$, where φ is the velocity potential and ψ is the streamline value. In general, we formulate the complex potential for M sources as

$$w = w(\zeta) = \sum_{m=1}^{M} \frac{q_m}{\pi} \left[\ln(\zeta - \zeta_m) + \ln(\zeta - \zeta_m^*)\right], \tag{5.32}$$

where ζ_m^* is the image of the original source ζ_m across the real axis, as depicted in Figure 5.10.

Transformation into the z-plane is performed by integrating the function $dz/d\zeta$ between the ζ value chosen to correspond to $z = 0$, $\zeta_{z=0}$ and ζ. Defining all sources to have equal and constant

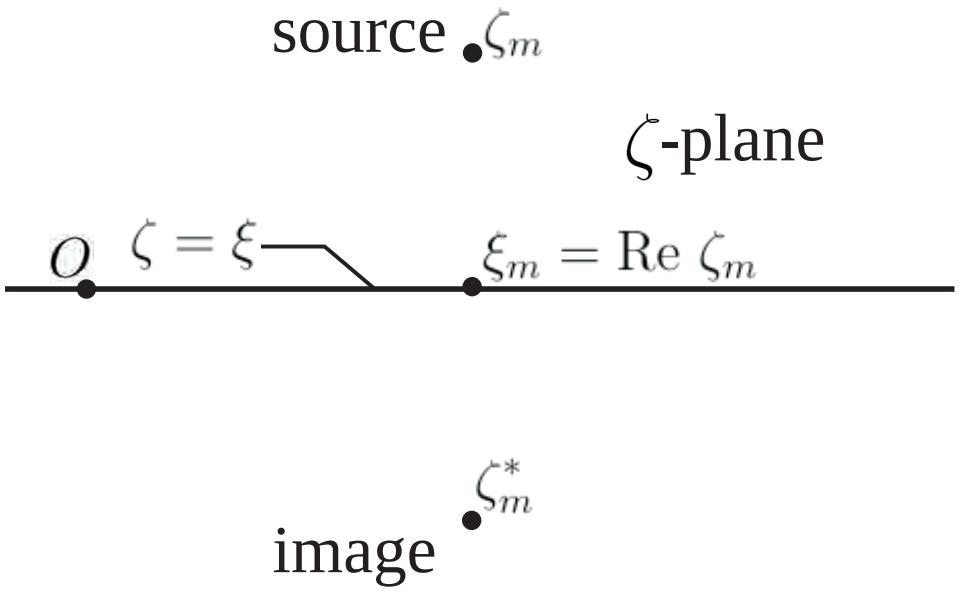

Figure 5.10: Illustration of a point source and its image about ξ-axis.

source strength $q_m \equiv q_o$, Equation 5.32 is simplified to

$$\prod_{m=1}^{M} (\zeta - \zeta_m)(\zeta - \zeta_m^*) = \mathrm{e}^{\pi w/q_o} = \mathrm{e}^{\pi\varphi/q_o}\left(\cos\left(\frac{\pi\psi}{q_o}\right) + i\sin\left(\frac{\pi\psi}{q_o}\right)\right), \tag{5.33}$$

If we restrict interest to the uniform flow originating at $-\infty$, $M \equiv 1$, $\zeta_1 \equiv 0$, we obtain

$$\zeta = \pm\sqrt{\mathrm{e}^{\pi\varphi/q_o}\left(\cos\left(\frac{\pi\psi}{q_o}\right) + i\sin\left(\frac{\pi\psi}{q_o}\right)\right)}. \tag{5.34}$$

The streamlines are depicted allowing φ/h_1 to vary over the range $(-\infty, \infty)$ for fixed values of ψ in the range $0 \leq \psi/h_1 \leq 1$, where $\psi/h_1 = 0$ and $\psi/h_1 = 1$ respectively correspond to the lower boundary (centerline for the burner) and upper boundary of the burner.

A change of variables is required in order to integrate between $\zeta_{z=0} \equiv a$ and ζ, prescribed by Equation 5.34. We choose a straight line path where $\zeta' = a + \lambda(\zeta - a)$, $0 < \lambda < 1$, allowing us to

reformulate the function $z(\zeta) = \int_a^\zeta \frac{G(\zeta')}{(\zeta'-a)^\beta} d\zeta'$ in to the form

$$z(\zeta) = (\zeta - a)^{1-\beta} \int_0^1 \frac{G(a + \lambda(\zeta - a))d\lambda}{\lambda^\beta}, \tag{5.35}$$

where $G(\zeta)$ is defined as the regular part of the function $\frac{dz}{d\zeta} = F(\zeta)$, which is not singular at $\zeta = a$. The Jacobi quadrature, described in Section 5.5.1, is used to numerically integrate Equation 5.35.

5.5.4 Arbitrary source locations

In addition to the streamlines originating from a source at $z \to -\infty$, we are also interested in the the streamlines originating from an arbitrary source configuration. In order to formulate the source problem, we rewrite Equation 5.32 assuming that there are M sources and that each source strength $q_m = \kappa_m q_o$ is an integer multiple κ_m of the constant source strength q_o, namely,

$$w = \sum_{m=1}^{M} \frac{\kappa_m q_o}{\pi} \left[\ln(\zeta - \zeta_m) + \ln(\zeta - \zeta_m^*)\right], \tag{5.36}$$

where ζ_m and ζ_m^* are still the respective ζ-plane source location and its image across the real axis. The exponential of Equation 5.36 simplifies to

$$\prod_{m=1}^{M} (\zeta - \zeta_m)^{\kappa_m} (\zeta - \zeta_m^*)^{\kappa_m} - \mathrm{e}^{\pi w/q_o} = 0, \tag{5.37}$$

which is a polynomial of order $2\sum\kappa_m$. The roots of this polynomial are calculated using a NAG [80] subroutine. The subroutine assumes an N^{th}-order polynomial equation of x of the form

$$\sum_{n=0}^{N} a_n x^n = 0,$$

where a_n is the constant complex coefficient corresponding to x^n. For large M in Equation 5.37, it can be quite time-consuming to manually calculate the coefficients a_n, so we present an example which suggests a method of automating the process. For $M = 1$ and $\kappa_m = 1$, Equation 5.37 simplifies to

$$\zeta^2 - (\zeta_1 + \zeta_1^*)\zeta + (\zeta_1\zeta_1^*) - \mathrm{e}^{\pi w/q_o} = 0.$$

For convenience we define $\hat{\zeta}_n$ where $\hat{\zeta}_{2n-1} \equiv \zeta_n$ and $\hat{\zeta}_{2n} \equiv \zeta_n^*$ (i.e. $\hat{\zeta}_1 = \zeta_1$, $\hat{\zeta}_2 = \zeta_1^*$, etc.). The coefficient a_n corresponding to ζ^n is the sum of the products of sets of length $N - n$, namely

$$a_{N-n} = (-1)^n \sum_{i=1}^{{}_N C_n} \left\{ \prod_{j=1}^{n} \hat{\zeta}_{C_{(N,n)}(i,j)} \right\},$$

where ${}_N C_n$ is the number of n-combinations in the set of N elements. $C_{(N,n)}(i,j)$ is the j^{th} term of the i^{th} combinatic containing n-combinations of N elements. The combinatics are obtained using a method described in [81].

The values of a_n are input into the NAG subroutine, returning $2\sum\kappa_m$ roots $\hat{\zeta}$. Several roots exist on the positive ζ half-plane; we evaluate Equation 5.35 for each of these positive roots ζ in order to obtain the complete source solution.

The values ζ_m need not be arbitrary and can be chosen to correspond to the desired source location in the z-plane. The method of calculating the source location in the ζ-plane involves inverting

Equation 5.17 and integrating, namely,

$$\zeta(z_1) - \zeta(z_0) = K \int_{z_0}^{z_1} \frac{1}{F(z)} dz, \tag{5.38}$$

where $F(\cdot)$ is the function describing the transformation $\frac{dz}{d\zeta}$.

We have numerically obtained results for several configurations, two of which are similar to burner Configuration I: the first is a duct having the same upper-half geometry (Part A) and the second having the same lower-half plane geometry (Part B). These geometries are depicted in Figure 5.11, Parts A and B, respectively. Part A has one unknown parameter ξ_2 and Part B has two unknown parameters ξ_4 and ξ_5.

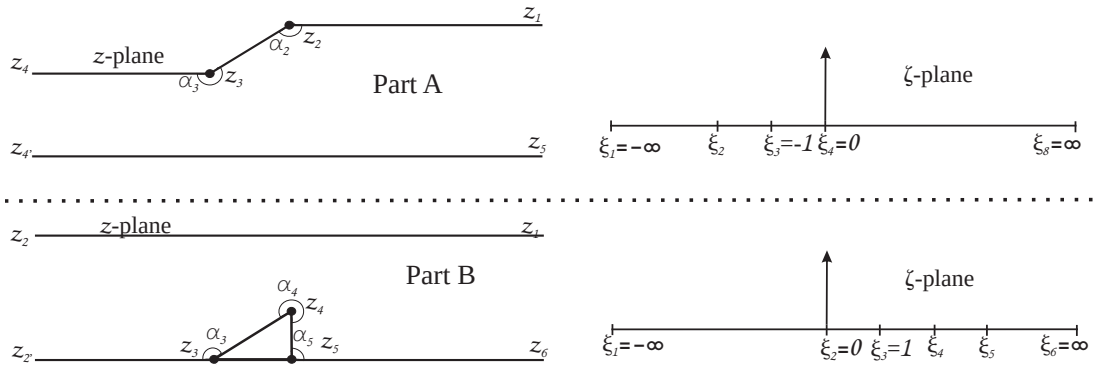

Figure 5.11: Illustration of geometries similar to those of burner Configuration I. Part A: geometry having similar upper half; Part B: geometry having similar lower half.

The numerical method described in Section 5.5 is used to calculate the Schwarz-Christoffel transformations. The dimensions used are identical to those for burner Configuration I described in Section 3.1. Fig. 5.12, Part A depicts the error S for several values ξ_2. The simplex used to converge upon the minimum value S is also illustrated. The first simplex (————) contains $N + 1 = 2$ arbitrary points. The following simplex (- - - - -) replaces the point $\mathbf{X}_{n=n_j}^{P=P_o}$ having the larger error

$S\left(\mathbf{X}_{n=n_j}^{P=P_o}\right)$ with the reflection about the line which is parallel to the ξ_2-axis and intersecting the point $\mathbf{X}_{n\neq n_j}^{P=P_o}$, with the smaller of the two errors $S\left(\mathbf{X}_{n\neq n_j}^{P=P_o}\right)$. $\mathbf{X}_{n=n_j}^{P=P_o}$ is replaced with $\mathbf{X}_{n=n_j}^{P=P_o+1}$ of the two points. This process continues until $S \ll 10^{-6}$. We determine $\xi_2 = -52.3$ where $S \sim 10^{-7}$, which is found after $P \sim 300$ simplex steps. The formula for the transformation is

$$z(\zeta) = K \int_a^{\zeta} \frac{(\zeta'+1)^{1/6}}{\zeta'(\zeta'+52.3)^{1/6}} d\zeta' + h_1, \text{ where } K = 8.31,\ a = -1. \tag{5.39}$$

Calculating the Schwarz-Christoffel transformation for the geometry depicted in Figure 5.11, Part B is slightly more complicated because there are two unknown parameters. Figure 5.12, Part B illustrates the contour of the calculated error S for numerous values of ξ_4 and ξ_5. The lower-right half is shaded because the results in this area are invalid because they violate the condition $\xi_i < \xi_{i+1}$. The figure also illustrates the three-point (triangular) simplex used to converge upon the optimum value. In this case, the first simplex (————) contains three points. In the following simplex ( ), the point $\mathbf{X}_{n=n_j}^{P=P_o}$, corresponding to the value having the largest error $S\left(\mathbf{X}_{n=n_j}^{P=P_o}\right)$, is replaced with its reflection about the line connecting the other two points. Again, this process is continued until the error $S \ll 10^{-6}$. We determine $\xi_4 = 82.0$ and $\xi_5 = 356.5$, where $S \sim 10^{-6}$ found after $P \sim 400$ steps. The formula for the transformation is

$$z(\zeta) = K \int_a^{\zeta} = \frac{(\zeta'-82.0)^{2/3}}{\zeta'(\zeta'-1)^{1/6}(\zeta'-356.5)^{1/2}} d\zeta', \text{ where } K = 8.28, a = 1. \tag{5.40}$$

The numerical method for calculating the Schwarz-Christoffel transformation exemplified above is extended to the full geometric complexity of burner Configurations I and II. The constants in

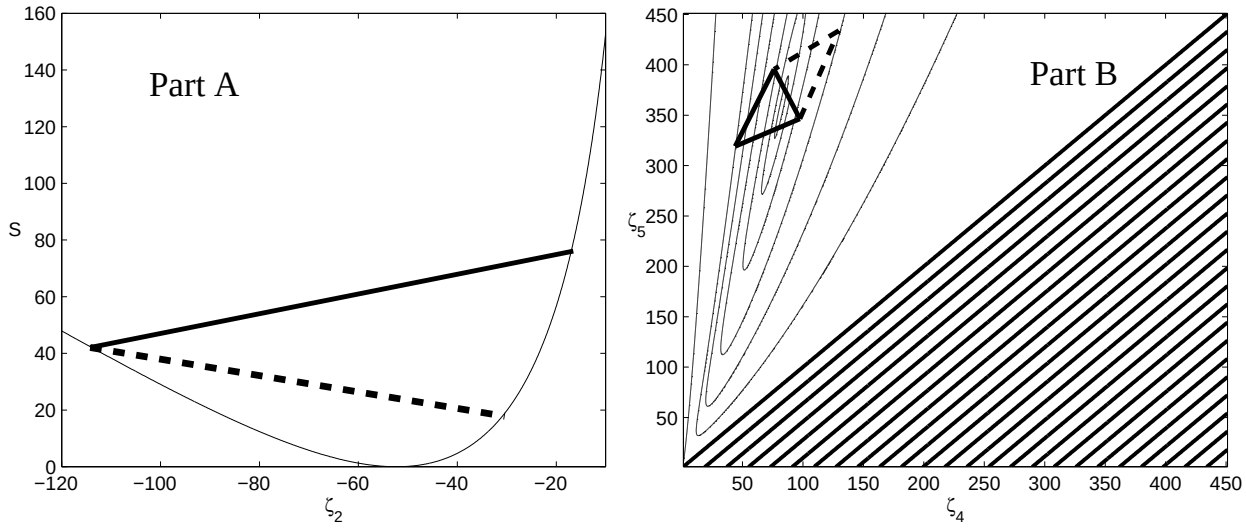

Figure 5.12: Illustration of two simplexes: Part A: in one-dimensional space; Part B: in two-dimensional space.

Equation 5.23 have been determined. The minimization procedure for each configuration requires $P \sim 500$ steps. The formula for the transformation of Configurations I and II is respectively

$$z(\zeta) = K \int_a^{\zeta} \frac{(\zeta' + 1.309)^{1/6}(\zeta' - 586.4)^{2/3}}{\zeta'(\zeta' + 393.1)^{1/6}(\zeta' - 1)^{1/6}(\zeta' - 2720)^{1/2}} d\zeta', \text{ where } K = 8.04, a = 1. \tag{5.41}$$

$$z(\zeta) = K \int_a^{\zeta} \frac{(\zeta' + 1.816)^{1/2}(\zeta' - 742.3)^{2/3}}{\zeta'(\zeta' + 327.2)^{1/2}(\zeta' - 1)^{1/6}(\zeta' - 3018)^{1/2}} d\zeta', \text{ where } K = 8.04, a = 1. \tag{5.42}$$

We depict streamlines of the hydrodynamic flow originating from a source at $\zeta = -\infty$ in Figures 5.13 and 5.14 for respective Configurations I and II. In Section 5.5.3 we describe the method used to calculate the response from arbitrary source configurations. In practice, we had to employ three integral paths before obtaining the correct streamlines, which are identical to those obtained with the numerical approximation of Laplace's equation in Section 5.2. The first method (a), depicted in Figure 5.15, is a straight line path between a and ζ. This method fails because the Jacobi distribution is not sufficiently distributed as $\zeta \to \infty$.

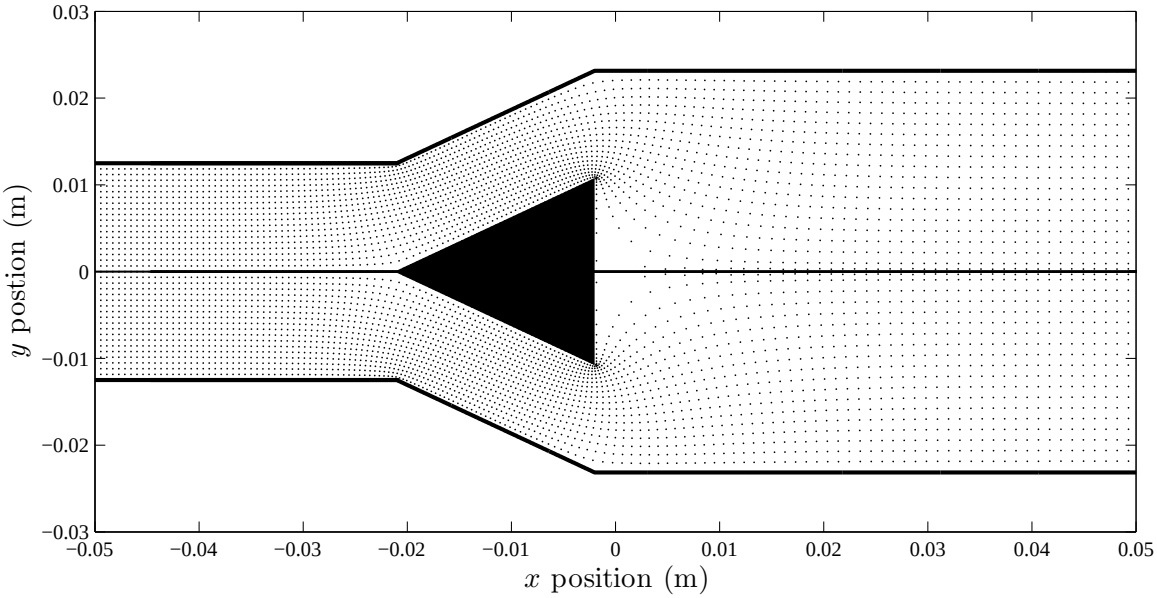

Figure 5.13: Illustration of hydrodynamic streamlines in burner Configuration I originating from a source located at $(-\infty, 0)$.

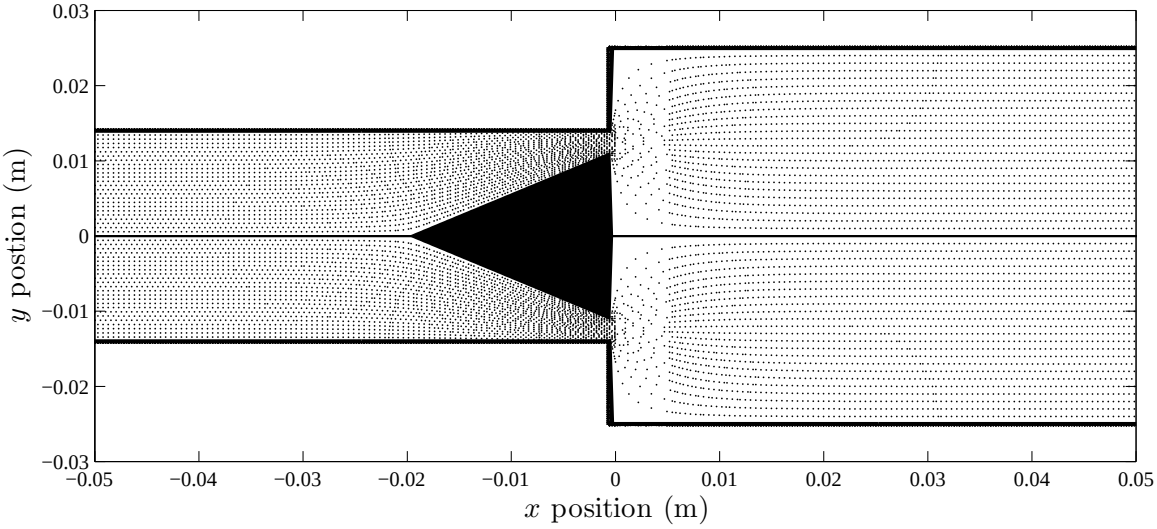

Figure 5.14: Illustration of hydrodynamic streamlines in burner Configuration II originating from a source located at $(-\infty, 0)$.

The second method (b) employs the definition $z(\xi_a) - z(\xi_b) \equiv K \int_{\xi_b}^{\xi_a} \frac{dz}{d\zeta'} d\zeta'$ and follows the real axis starting at a and ending at the singularity which is closest to the value ζ, say ξ_c. The path to ζ from ξ_c is a straight line. The equation describing the integral path is

$$\int_a^\zeta \frac{dz}{d\zeta'} d\zeta' = z(\xi_c) - z(a) + \int_{\xi_c}^\zeta \frac{dz}{d\zeta'} d\zeta',$$

where the quantity $z(\xi_c) - z(a)$ is defined by the transformation. The method failed because the desired numerical precision could not be reconciled with the first-order pole at the origin.

The third method (c) successfully determines the streamlines of the potential flow. It first integrates between a and a point on the imaginary ζ-axis, say $\tilde{\eta}$. This method is the parallel to method (b) except it follows the imaginary rather than the real axis; it ensures stability of the integral as $\zeta \to \infty$ by refining the number of abscissae near ζ. The imaginary axis point is determined by the formula:

$$\tilde{\eta} = \exp(k_0 + k_1 \log(|\zeta|)/\log(V_{max}))i,$$

where k_0 and k_1 are positive, fixed constants, and $V_{max} \sim 10^{300}$ is the largest number recognized by the chosen numerical precision.

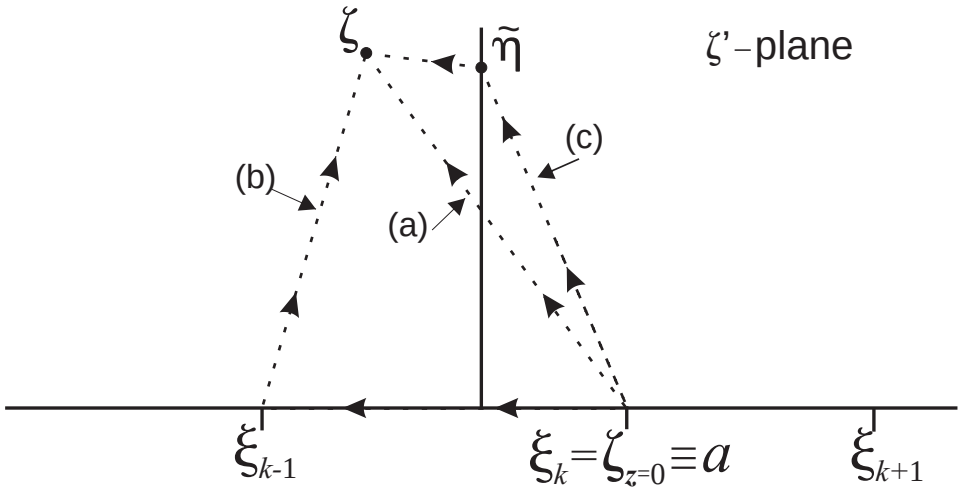

Figure 5.15: Illustration of the integration paths used to calculate hydrodynamic streamlines in burner Configurations I and II.

Figures 5.13 and 5.14 illustrates the hydrodynamic streamlines originating from a source at $\zeta \to -\infty$ for the burner Configurations I and II, respectively. Figures 5.16 and 5.17 illustrate the hydrodynamic streamlines originating from two arbitrary source configuration for burner Configuration I. In each case, there still exists a source at $\zeta \to -\infty$.

Table 5.2: Position of the hydrodynamic region boundaries and blockage length for burner Configurations I and II

Burner configuration	X_1	X_2	$\bar{\ell}$
Configuration I	-0.038 m	0.015 m	0.095 m
Configuration II	-0.038 m	0.021 m	0.138 m

We determine the blockage length using Equation 5.7 from the the streamlines depicted in Figures 5.13 and 5.14. In Table 5.2 we compare the position of the hydrodynamic region boundaries X_1 and X_2 and the value of the blockage length $\bar{\ell}$ for both Configurations I and II. These results are also presented in [61, 63].

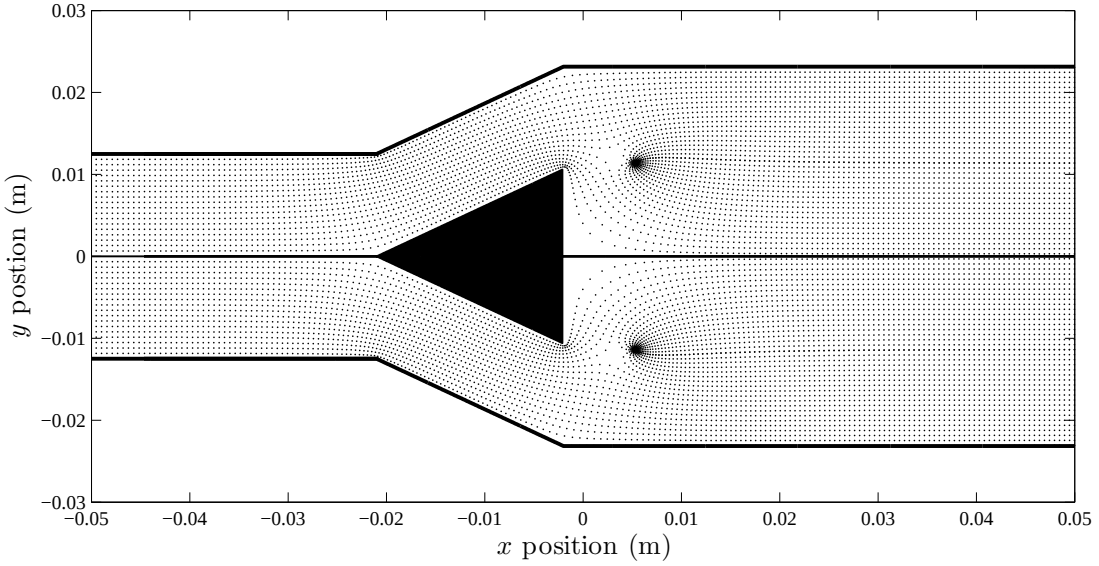

Figure 5.16: Illustration of hydrodynamic streamlines in burner Configuration I originating from sources located at $(-\infty, 0)$ and $(0.006, \pm 0.011)$. All three sources are of equal strength.

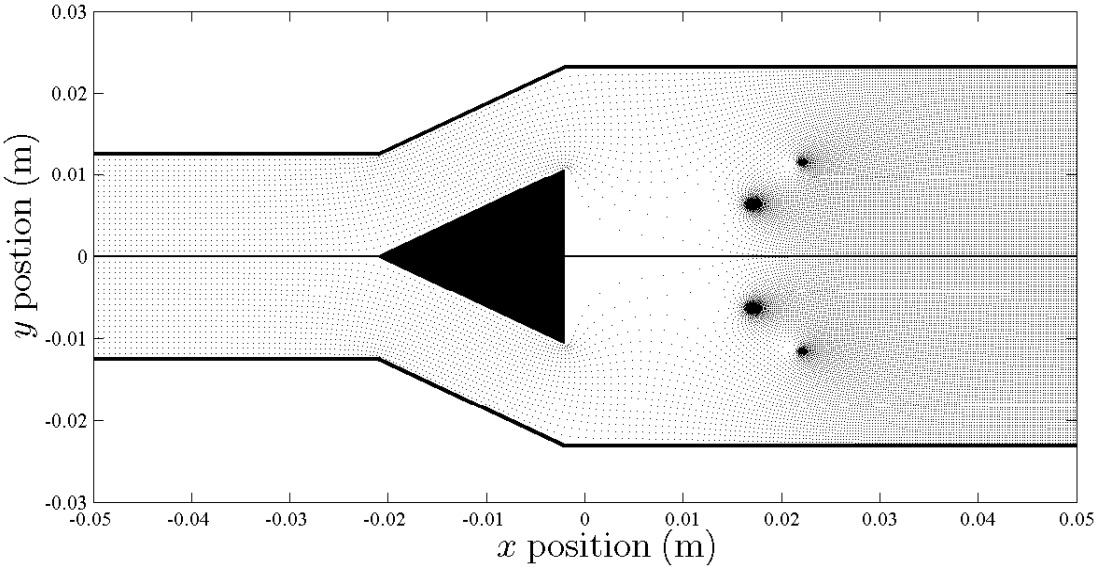

Figure 5.17: Illustration of hydrodynamic streamlines in burner Configuration I originating from sources located at $(-\infty, 0)$, $(0.017, \pm 0.006)$, and $(0.023, \pm 0.011)$, where The sources located at $(0.017, \pm 0.006)$ have three times the source strength as the other three.

5.6 The blockage length for the idealised combustor

The blockage length for the idealised burner Configuration III of Section 3.1 is determined analytically from the potential flow of unit speed $\varphi^* = \varphi^*(\mathbf{x})$ within the duct. We consider the symmetrical duct depicted in Figure 5.18 having width $2h$, as well as two flat plate constrictions of width ℓ_f, creating an aperture of width $\Delta = 2h - 2\ell_f$. The potential flow is determined by Schwarz-Christoffel transformation. The transformation from the z to ζ-plane takes the form

$$\frac{dz}{d\zeta} = K\frac{\zeta - \xi_4}{(\zeta - \xi_2)\sqrt{\zeta - \xi_3}\sqrt{\zeta - \xi_5}}. \tag{5.43}$$

The transformation points ξ_2 and ξ_4 are respectively chosen to coincide with $\zeta = 0$ and $\zeta = 1$.

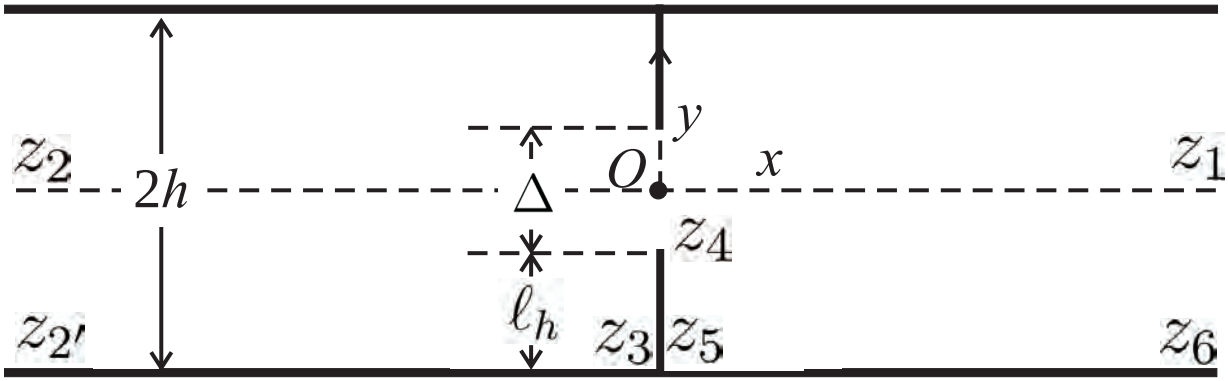

Figure 5.18: Schematic of the idealised Combustor III half-plane and its image across the x_1-axis.

Transformation points ξ_3 and ξ_5 are yet been determined but, from the symmetry of the problem, are to be respectively chosen to coincide with $\zeta = \alpha^2$ and $\zeta = 1/\alpha^2$. The transformation has the current form

$$dz = K\frac{\zeta - 1}{\zeta\sqrt{\zeta - \alpha^2}\sqrt{\zeta - 1/\alpha^2}}d\zeta. \tag{5.44}$$

The constant K is determined by equating the integral around the singularity $\zeta = \xi_2$ with the distance between z_2 and $z_{2'}$ in the z-plane; it is found to be $K = \frac{h}{\pi}$. Equation 5.44 is integrated on either side to take the form

$$z = \frac{h}{\pi} \ln \left(\frac{\sqrt{\zeta - \alpha^2} + \sqrt{\zeta - 1/\alpha^2}}{\sqrt{\frac{1}{\alpha^2} - \frac{1}{\zeta}} + \sqrt{\alpha^2 - \frac{1}{\zeta}}} \right), \tag{5.45}$$

where the constant α is determined by substituting $z = z_4 = 0 + i\ell_f$ on the left-hand side and the corresponding point $\zeta = \xi_4 = 1$ on the right-hand side. The constant is determined by the formula:

$$\alpha = \tan\left(\frac{\pi\Delta}{8h}\right). \tag{5.46}$$

The complex potential flow within the duct has the form $w = \varphi^* + i\psi^* = \frac{h}{\pi} \ln \zeta$. The blockage length $\bar{\ell}$ due to the constriction is the integral along the entire x_1-axis of the difference between the axial flow speeds $\partial\varphi^*/\partial x_1$ in the duct with the constriction and the duct without the constriction (where $\partial\varphi/\partial x_1 = 1$). Namely,

$$\begin{aligned} \bar{\ell} &= \int_{-\infty}^{\infty} \left(\tfrac{\partial\varphi^*}{\partial x} - 1\right) dx \\ &= \int_{-\infty}^{\infty} \left(\tfrac{\partial w}{\partial z} - 1\right) dz \\ &= [w - z]_{-\infty}^{\infty}, \end{aligned} \tag{5.47}$$

which is determined from the limits as $z \to \pm\infty$. In the upper limit as $z \to \infty$, $\zeta \to \infty$, the transformation takes the form

$$\begin{aligned} z &\simeq \tfrac{2h}{\pi} \ln\left(\tfrac{2\sqrt{\zeta}}{(\alpha + 1/\alpha)}\right) \\ &= \tfrac{h \ln\zeta}{\pi} - \tfrac{2h}{\pi} \ln\left(\tfrac{1}{2}(\alpha + 1/\alpha)\right), \end{aligned} \tag{5.48}$$

and $w - z$ therefore approaches

$$w - z \to \frac{2h}{\pi} \ln\left(\frac{1}{2}(\alpha + 1/\alpha)\right). \tag{5.49}$$

Similarly, in the lower limit as $z \to -\infty$, $\zeta \to 0$, and the transformation takes the form

$$\begin{aligned} z &\simeq \tfrac{2h}{\pi} \ln\left(\tfrac{\sqrt{\zeta} i(\alpha+1/\alpha)}{2i}\right) \\ &= \tfrac{h \ln\zeta}{\pi} + \tfrac{2h}{\pi} \ln\left(\tfrac{1}{2}(\alpha + 1/\alpha)\right), \end{aligned} \tag{5.50}$$

and $w - z$ subsequently approaches

$$w - z \to -\frac{2h}{\pi} \ln\left(\frac{1}{2}(\alpha + 1/\alpha)\right). \tag{5.51}$$

The blockage is obtained by substitution into Equation 5.47 and is determined to be

$$\bar{\ell} = [w - z]_{-\infty}^{\infty} = \frac{4h}{\pi} \ln\left[\frac{1}{2}\left(\tan\left(\frac{\pi}{4} - \frac{\pi\ell_f}{4h}\right) + \cot\left(\frac{\pi}{4} - \frac{\pi\ell_f}{4h}\right)\right)\right], \tag{5.52}$$

which we simplify to the following final expression for the blockage length:

$$\bar{\ell} = -\frac{4h}{\pi} \ln\left[\cos\left(\frac{\pi\ell_f}{2h}\right)\right]. \tag{5.53}$$

Chapter 6

The thermo-acoustic Fant equation

The principal sources of sound are unsteady heat release, vorticity, and accelerated entropy inhomogeneities, so called entropy noise. At high Reynolds number, heat and momentum transfer by molecular diffusion can be neglected, although it can be important in low velocity regions near the wall. The momentum equation can be taken in the form

$$\frac{\partial \mathbf{v}}{\partial t} + \nabla B = -\boldsymbol{\omega} \wedge \mathbf{v} + T\nabla s - \frac{\eta}{\rho} \operatorname{curl} \boldsymbol{\omega}, \tag{6.1}$$

where $\mathbf{v}$ is the velocity, $\boldsymbol{\omega} = \operatorname{curl} \mathbf{v}$ is the vorticity, ρ, T, s are the respective density, temperature, and specific entropy, η is the shear component of viscosity, and $B = c_p T + \frac{1}{2}v^2$ is the total enthalpy (c_p being the ratio of specific heats at constant pressure), which is constant throughout the flow for steady, irrotational, and homentropic conditions.

Outside the regions of vorticity and entropy inhomogeneities, variations in the total enthalpy B correspond to sound waves and are equal to $-\partial\varphi^*/\partial t$, where $\varphi^*(\mathbf{x}, t)$ is the velocity potential of the incompressible and irrotational flow. Sound production principally occurs in the region near the

flame-holder. We restrict interest to low frequency waves where acoustic disturbances propagate as plane waves in the duct, and where the mean flow Mach number M is small. Treating the fluid as an ideal gas, in Section 2.3 we cast the momentum equation into the acoustic analogy for the total enthalpy

$$\left(\frac{1}{c^2}\frac{\partial^2}{\partial t^2} - \frac{\partial^2}{\partial x_j x_j}\right) B = \operatorname{div}\left(\boldsymbol{\omega} \wedge \mathbf{v} - (T\nabla s)' + \nu \operatorname{curl} \boldsymbol{\omega}\right) + \frac{\partial}{\partial t}\left(\frac{1}{c_p}\frac{\partial s}{\partial t}\right), \tag{6.2}$$

where here and henceforth B denotes the perturbation from the mean value of the total enthalpy, $(T\nabla s)'$ denotes the corresponding perturbation, c is the local speed of sound, and $\nu = \eta/\rho$ is the kinematic shear component of viscosity. The repeated subscript j implies summation over all three spatial coordinates. The first term on the right-hand side of Equation 6.2 corresponds to the vortex and entropic sources, and the second term corresponds to the monopole flame source. In the low Mach number approximation, we can approximate the acoustic pressure to be $p' \simeq \rho B$ in the upstream and downstream sections.

We can express the solution $B(\mathbf{x}, t)$ of Equation 6.2 in terms of a Green's function $G = G(\mathbf{x}, \mathbf{y}, t, \tau)$ that satisfies

$$\left(\frac{1}{c^2}\frac{\partial^2}{\partial t^2} - \frac{\partial^2}{\partial y_j y_j}\right) G = \delta(\mathbf{x} - \mathbf{y})\delta(t - \tau), \quad G = 0 \text{ for } \tau > t, \tag{6.3}$$

where $\mathbf{y} = (y_1, y_2, y_3)$. The total enthalpy Green's function G is determined for the idealised duct (Configuration III) in Section 4.2. Green's theorem, causality, and the momentum equation 6.1 give the solution of the aerodynamic sound equation 6.2 in the form [28, 53, 55, 82]

$$\begin{aligned} B(\mathbf{x}, t) = &\int_{-\infty}^{\infty} \oint_S G \frac{\partial \mathbf{v}}{\partial \tau} \cdot d\mathbf{S}(\mathbf{y}) d\tau - \int_{-\infty}^{\infty} \int_V \frac{\partial G}{\partial \mathbf{y}} \cdot \left(\boldsymbol{\omega} \wedge \mathbf{v} - (T\nabla s)' + \nu \operatorname{curl} \boldsymbol{\omega}\right) d^3\mathbf{y} d\tau \\ &- \int_{-\infty}^{\infty} \int_V \frac{\partial G}{\partial \tau} \frac{1}{c_p} \frac{\partial s}{\partial \tau} d^3\mathbf{y} d\tau, \end{aligned} \tag{6.4}$$

where the vector surface element $d\mathbf{S}$ on S is directed into the fluid and V denotes the spatial region occupied by the fluid. The surface integral term $\partial\mathbf{v}/d\tau$ corresponds to the mean inflow at the upstream end. In the volume integral, the viscous term $\nu\,\mathrm{curl}\,\boldsymbol{\omega}$ is a dipole concentrated near the duct boundary layer, and is small relative to other terms at high Reynolds number. The vortex source term $\boldsymbol{\omega}\wedge\mathbf{v}$ is also a dipole and together with the entropic terms $\partial s/\partial\mathbf{y}$ corresponds to the effect of momentum and thermal mixing downstream of the flame. The final integral is a monopole and corresponds to the entropic production from the flame.

We present two methods for solving Equation 6.4: the first is the 'direct' method which involves equating two independent equations for the total enthalpy; the second is the 'adjoint-equation' method which involves determining an equation for the Green's function component β and subsequently proving the Fant equation in terms of Q as the adjoint of the β-equation. In this chapter, we derive the Fant equation for Configuration III; we then extend it to application to Configuration II in Chapter 9.

6.1 The direct method

The dominant source of sound in the duct is the heat release flame monopole due to the flame. Let $Q_f(t)$ denote the flame source strength. The flame is assumed to occupy a compact region just downstream of the flame-holder. An observer in the downstream duct at $\mathbf{x}$ will detect source strength $Q(t)+Q_f(t)$, where $Q(t)$ is the component strictly due to the upstream volume source Q_o past the constriction. A schematic of the idealised burner configuration is depicted in Figure 6.1, where we define control surfaces $\Sigma=\Sigma_-+\Sigma_+$, and Σ_o which are defined as follows: Σ_+ is a plane cross-section downstream of the constriction, where the steady and unsteady flows are nominally parallel to the

x_1-axis and of infinitesimal Mach number. Σ_- is upstream from Σ_+ and consists of the constriction at $x_1 = 0$, two vortex sheets originating at the edges of the constriction (defining the edge of the separated flows), and a short vertical section just downstream of the constriction where jet velocities have become uniform and parallel to the wall.

We initially consider a special case of Equation 6.4 where the duct is closed at the constriction $x_1 = 0$. We determine the total enthalpy B from the special Green's function G_o, defined by Equation 4.25. Substituting the unknown combined source strength $Q(t) + Q_f(t)$ into Equation 6.4, where only the surface integral is retained, with viscous contributions discarded, and with S extended to include the control surface Σ enclosing the flame, we can express the total enthalpy as

$$B = B(x_1, t) = \int_{-\infty}^{\infty} \frac{\partial}{\partial \tau}(Q_f + Q)(\tau) G_o(x_1, 0, t, \tau) d\tau, \qquad x_1 > \sqrt{\mathcal{A}}, \tag{6.5}$$

which is strictly a formal representation as both the volume velocity $Q(t)$ and the flame heat release rate $Q_f(t)$ are unknown at this point.

An interchange in dummy variable and integration by parts permits the left-hand side of Equation 4.27 to be used to express Equation 6.5 in terms of $\beta(\tau, x_1, t)$ in the form

$$\begin{aligned} B = B(x_1, t) = \int_{-\infty}^{\infty} \beta(\tau, x_1, t) \Bigg[& \bar{\ell} \frac{\partial}{\partial \tau}(Q + Q_f)(\tau) \\ & + \frac{i}{2\pi} \int \int_{-\infty}^{\infty} (Q + Q_f)(\xi) \left(\frac{c_1 \cos(k_1 L_1)}{\sin(k_1 L_1)} - \frac{c_2 \sin(k_2 L_2)}{\cos(k_2 L_2)} \right) \mathrm{e}^{i\omega(\xi - \tau)} d\omega d\xi \Bigg] d\tau, \end{aligned} \tag{6.6}$$

where $\bar{\ell}$ is defined for Configuration III in Equation 5.53.

The sound in the downstream duct can alternatively be formulated in terms of the thermo-acoustic sources in Equation 6.4. In this alternative formulation, we assume viscous contributions

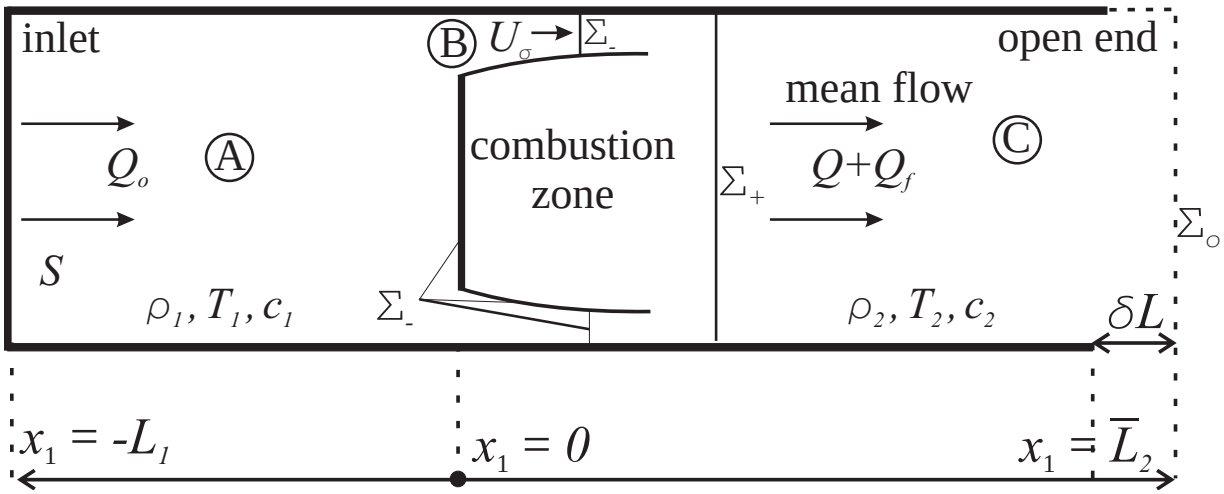

Figure 6.1: Schematic of the idealised Combustor III depicting source configurations and control surfaces.

are negligible in high Reynolds number. It is convenient to express $B = B(\mathbf{x}, t)$ in the separated form

$$B = B_o + B_\sigma + B_f, \tag{6.7}$$

where B_o, B_σ, and B_f respectively correspond to the total enthalpy contribution from the inlet volume velocity Q_o, from the momentum and thermal mixing over the combustion zone, and from the heat release from the flame. Vorticity and entropy sources in the flow beyond the flame are ignored.

The enthalpy component corresponding to the inlet volume velocity is calculated by substituting the Green's function 4.24 into the surface integral term in Equation 6.4 for a source located at $x_1 = -L_1$ having strength Q_o. Integrating by parts and re-naming the dummy variable of integration we have

$$B_o = B_o(x_1, t) = -\int_{-\infty}^{\infty} Q_o(\xi)\frac{\partial G}{\partial \xi}(x_1, -L_1, t, \xi)d\xi = \frac{ic_1}{2\pi}\int\int\int_{-\infty}^{\infty}\frac{\beta(\tau, x_1, t)Q_o(\xi)}{\sin(k_1 L_1)}\mathrm{e}^{i\omega(\xi-\tau)}d\omega d\xi d\tau. \tag{6.8}$$

The vorticity, entropy, and viscous component corresponding to the mixing region is calculated by substituting the Green's function 4.24 into the first volume integral of Equation 6.4 which yields

$$B_\sigma = B_\sigma(x_1,t) = -\int_{-\infty}^{\infty}\int_V \beta(\tau,x_1,t)\left(\nabla Y\cdot[\boldsymbol{\omega}\wedge\mathbf{v}-(T\nabla s)'+\nu\,\mathrm{curl}\,\boldsymbol{\omega}]\right)(\mathbf{y},\tau)d^3\mathbf{y}d\tau, \tag{6.9}$$

where the integral is confined to combustion zone and Y is the Kirchoff vector defined in Equation 4.22. Although turbulent sources exist also downstream of the combustion zone, they are essentially weak quadrupoles and make negligible contribution to the sound.

The enthalpy production term corresponding to the flame is also calculated in [82]. The heat release per unit flame volume is $q = \rho T\partial s/\partial t$ so the total volume production from the flame is

$$Q_f(t) = \int_V \frac{q(\mathbf{y},t)}{c_p\rho T}d^3\mathbf{y}. \tag{6.10}$$

In the heat release component of the total enthalpy

$$B_f = B_f(x_1,t) = -\int_{-\infty}^{\infty}\int_V \frac{\partial G}{\partial\tau}\frac{1}{c_p}\frac{\partial s}{\partial\tau}d^3\mathbf{y}d\tau, \tag{6.11}$$

the Green's function can be cast as simply $G = \alpha(\tau,x_1,t)$ because terms β in Equation 4.21 are $O(k_2y_1)$ smaller in the downstream duct. It follows that

$$B_f(x_1,t) = -\int_{-\infty}^{\infty} Q_f(\tau)\frac{\partial\alpha}{\partial\tau}d\tau, \tag{6.12}$$

which can be recast into the following form using Equation 4.26:

$$B_f(x_1,t) = \int_{-\infty}^{\infty} \beta(\tau,x_1,t)\left[\bar{\ell}\,\frac{\partial Q_f}{\partial \tau}(\tau) + \frac{ic_1}{2\pi}\int\int_{-\infty}^{\infty} \frac{Q_f(\xi)\cos(k_1L_1)}{\sin(k_1L_1)} \mathrm{e}^{i\omega(\xi-\tau)} d\omega d\xi\right] d\tau. \tag{6.13}$$

From Equation 6.7, the net acoustic field is given by

$$\begin{aligned} B(x_1,t) = \int_{-\infty}^{\infty} \beta(\tau,x_1,t)\Bigg[\bar{\ell}\,\frac{\partial Q_f}{\partial \tau}(\tau) + \frac{ic_1}{2\pi}\int\int_{-\infty}^{\infty} (Q_f(\xi)\cos(k_1L_1) + Q_o(\xi))\frac{\mathrm{e}^{i\omega(\xi-\tau)}}{\sin(k_1L_1)} d\omega d\xi \\ - \int_V \left(\nabla Y \cdot [\boldsymbol{\omega}\wedge\mathbf{v} - T\nabla s + \nu\,\mathrm{curl}\,\boldsymbol{\omega}]\right)(\mathbf{y},\tau) d^3\mathbf{y}\Bigg] d\tau. \end{aligned} \tag{6.14}$$

Equating the total enthalpies given in Equations 6.6 and 6.13 yields the thermo-acoustic Fant equation for the idealised burner

$$\begin{aligned} \bar{\ell}\,\frac{dQ}{dt} + \frac{i}{2\pi}\int\int_{-\infty}^{\infty} Q(\xi)\left(\frac{c_1\cos(k_1L_1)}{\sin(k_1L_1)} - \frac{c_2\sin(k_2L_2)}{\cos(k_2L_2)}\right)\mathrm{e}^{i\omega(\xi-t)} d\omega d\xi \\ = \frac{i}{2\pi}\int\int_{-\infty}^{\infty}\left(\frac{c_1Q_o(\xi)}{\sin(k_1L_1)} + \frac{c_2Q_f(\xi)\sin(k_2L_2)}{\cos(k_2L_2)}\right)\mathrm{e}^{i\omega(\xi-t)d\omega} d\xi \\ - \int_V \left(\nabla Y \cdot [\boldsymbol{\omega}\wedge\mathbf{v} - (T\nabla s)' + \nu\,\mathrm{curl}\,\boldsymbol{\omega}]\right)(\mathbf{y},t) d^3\mathbf{y}, \end{aligned} \tag{6.15}$$

which determines $Q(t)$ in terms of $Q_o(t)$ and $Q_f(t)$ and mixing sources in the combustion zone. Although volume velocity $Q(t)$ occurs linearly on the left of Equation 6.15, the equation is actually nonlinear as both the heat release source $Q_f(t)$ and the mixing region source in the final integral exhibits nonlinearity.

Thus far it has been assumed that only plane waves propagate in the burner, that the flame region is acoustically compact, and that the upstream and downstream Mach number $M \ll 1$. Proceeding further, application of the Fant equation 6.15 requires the final integral on right-hand side to be expressed in terms of Q. In order to do this we assume the combustion zone is quasi-static, which is

equivalent to assuming it is acoustically compact. In other words, $\partial \mathbf{v}/\partial t$ on the left of Equation 6.1 can be neglected across the combustion zone provided $\ell_{cz} \ll \lambda$, where $\ell_{cz} \sim O(h)$ is the axial extent of the combustion zone and $\lambda = c/f$ (f being the characteristic frequency) is the characteristic wavelength. Namely, the combustion zone is acoustically compact provided $fh/c \ll 1$, which for Configuration III requires the frequencies of interest $f \ll 3000\,\mathrm{Hz}$. In Figure 6.1, we show that the combustion zone is bounded by the control surface $\Sigma = \Sigma_- + \Sigma_+$, where in the quasi-static approximation the pressure in the jet must be equal to p' on the interface portion of the control surface Σ_- on which the flow speed is uniform and equal to $U_\sigma(t)$.

Neglecting $\partial \mathbf{v}/\partial t$ on the left of Equation 6.1, the final integral on the right of Equation 6.15 can be replaced by

$$-\int_V \nabla Y \cdot \nabla B d^3\mathbf{y} = -\int_V \mathrm{div}\,(B\nabla Y) d^3\mathbf{y}$$

because $\nabla^2 Y = 0$. It follows from the divergence theorem that

$$-\int_V \mathrm{div}\,(B\nabla Y) d^3\mathbf{y} = \oint_{\Sigma_- + \Sigma_+} B\nabla Y \cdot d\mathbf{S} \simeq (B_+ - B-)\mathcal{A}, \tag{6.16}$$

noting that $-\oint_{\Sigma_-} \nabla Y \cdot d\mathbf{S} = \oint_{\Sigma_+} \nabla Y \cdot d\mathbf{S} = \mathcal{A}$, and where $B_\pm$ are the respective values of B on $\Sigma_\pm$. In formula 6.16 we can take $B_+ = p'/\rho_2$, where the mean flow velocity is negligible and the unsteady pressure p' is the uniform quasi-static pressure in the combustion region. Over the interface portions of Σ_- the velocity is uniform and equal to $U_\sigma(t)$ so that $B_- = p'/\rho_1 + \frac{1}{2}U_\sigma^2$. The volume flux Q through the constriction is initially carried by the jets so $Q = \sigma \mathcal{A}_\sigma U_\sigma$, where $\sigma \simeq 0.6$ is the

jet contraction ratio and A_c is the cross-sectional area of the constriction. Therefore,

$$\begin{aligned}\mathcal{A}(B_+ - B_-) &= \mathcal{A}p'\left(\frac{1}{\rho_2} - \frac{1}{\rho_1}\right) - \frac{1}{2}\mathcal{A}U_\sigma^2 \\ &= -\mathcal{A}B_+\left(\frac{\rho_2}{\rho_1} - 1\right) - \frac{\mathcal{A}Q^2}{2\sigma^2\mathcal{A}_\sigma^2} \\ &= \frac{ic_2}{2\pi}\left(\frac{\rho_2}{\rho_1} - 1\right)\int\int_{-\infty}^{\infty}(Q_f + Q)(\xi)\frac{\sin(k_2L_2)}{\cos(k_2L_2)}\mathrm{e}^{i\omega(\xi-t)}d\omega d\xi - \frac{\mathcal{A}Q^2}{2\sigma^2\mathcal{A}_\sigma^2},\end{aligned} \tag{6.17}$$

where B_+ has been calculated in terms of Q and Q_f from Equation 6.5.

Substitution of Equations 6.16 and 6.17 into Equation 6.15 yields the quasi-static Fant equation approximation

$$\begin{aligned}\rho_1\bar{\ell}\,\frac{dQ}{dt} + \frac{i}{2\pi}\int\int_{-\infty}^{\infty}Q(\xi)\left(\frac{\rho_1c_1\cos(k_1L_1)}{\sin(k_1L_1)} - \frac{\rho_2c_2\sin(k_2L_2)}{\cos(k_2L_2)}\right)\mathrm{e}^{i\omega(\xi-t)}d\omega d\xi \\ = \frac{i}{2\pi}\int\int_{-\infty}^{\infty}\left(\frac{\rho_1c_2Q_o(\xi)}{\sin(k_1L_1)} + \frac{\rho_2c_2Q_f(\xi)\sin(k_2L_2)}{\cos(k_2L_2)}\right)\mathrm{e}^{i\omega(\xi-t)} - \frac{\rho_1\mathcal{A}Q^2}{2\sigma^2\mathcal{A}_\sigma^2}.\end{aligned} \tag{6.18}$$

This equation has been derived strictly under the assumption that flow past the flame-holder is unidirectional, in the positive x_1 direction; however, reverse flow is know to occur at high-amplitude oscillations, although these are typically small. We generalise for the reverse flow case by replacing Q^2 on the right hand side with $Q|Q|$. Similarly, limit cycle and other 'steady state' motions in the burner are usually considered for constant value inflow volume velocities $Q_o = \bar{Q}_o$ so solutions of Equation 6.18 are sought that are valid long after transients arising from starting flow have vanished. So we put $Q_o(\xi) = \bar{Q}_o$ where $\int_{-\infty}^{\infty}\bar{Q}_o\mathrm{e}^{i\omega\xi}d\xi = 2\pi\bar{Q}_o\delta(\omega)$. Taking account of the above generalisation and assumption, we cast the quasi-static approximation of the thermo-acoustic Fant equation into

the following final form

$$\rho_1 \bar{\ell}\,\frac{dQ}{dt} + \frac{i}{2\pi}\int\int_{-\infty}^{\infty}(Q(\xi)-\bar{Q}_o)\left(\frac{\rho_1 c_1\cos(k_1L_1)}{\sin(k_1L_1)} - \frac{\rho_2 c_2\sin(k_2L_2)}{\cos(k_2L_2)}\right)\mathrm{e}^{i\omega(\xi-t)}d\omega d\xi \\ = \frac{i\rho_2 c_2}{2\pi}\int\int_{-\infty}^{\infty}\frac{Q_f(\xi)\sin(k_2L_2)}{\cos(k_2L_2)}\mathrm{e}^{i\omega(\xi-t)} - \frac{\rho_1\mathcal{A}Q|Q|}{2\sigma^2\mathcal{A}_\sigma^2}. \tag{6.19}$$

This approximation of the Fant equation is the most significant equation of this thesis. It will be used extensively in Chapters 7, 8 to obtain respective linear and nonlinear results for Configuration III. It will be extended in Chapter 9 to account for the Limousine burner Configuration II. It is interesting to note that we can derive the thermo-acoustic Fant Equation using both a 'direct' method described above but also using an 'adjoint-equation' method which is described in the following section, and serves to justify the equating the acoustic fields of Equations 6.6 and 6.14.

6.2 The adjoint-equation method

In both the direct and adjoint-equation methods, the net acoustic field is determined from summation of its components. We cast Equation 6.14 in the form

$$B(x_1,t) = \int_{-\infty}^{\infty}\beta(\tau,x_1,t)\mathcal{F}(\tau)d\tau, \tag{6.20}$$

where $\mathcal{F}=\mathcal{F}(\tau)$ can be described as a 'Fant equation source' and is defined as

$$\mathcal{F}(\tau) = \bar{\ell}\,\frac{\partial Q_f}{\partial\tau}(\tau) + \frac{ic_1}{2\pi}\int\int_{-\infty}^{\infty}(Q_f(\xi)\cos(k_1L_1)+Q_o(\xi))\frac{\mathrm{e}^{i\omega(\xi-\tau)}}{\sin(k_1L_1)}d\omega d\xi \\ - \int_V\left(\nabla Y\cdot[\boldsymbol{\omega}\wedge\mathbf{v} - T\nabla s + \nu\,\mathrm{curl}\,\boldsymbol{\omega}]\right)(\mathbf{y},\tau)d^3\mathbf{y}. \tag{6.21}$$

In order to obtain the Fant equation we differentiate Equation 4.27 with respect to τ to yield

$$\begin{aligned}\bar{\ell}\,\frac{\partial\beta}{\partial\tau} - \frac{i}{2\pi}\int\int_{\infty}^{\infty}\beta(\xi,x_1,t)\left(\frac{c_1\cos(k_1L_1)}{\sin(k_1L_1)} - \frac{c_2\sin(k_2L_2)}{k_2\cos(k_2L_2)}\right)\mathrm{e}^{-i\omega(\xi-\tau)}d\omega d\xi \\ = \frac{\partial G_o}{\partial\tau} \equiv -\frac{ic_2}{2\pi\mathcal{A}}\int_{-\infty}^{\infty}\frac{\sin[k_2(x_1-L_2)]}{\cos(k_2L_2)}\mathrm{e}^{-i\omega(\xi-\tau)}d\omega,\end{aligned} \tag{6.22}$$

which we call the β equation and denote it as

$$\mathcal{L}\beta = \frac{\partial G_o}{\partial\tau},$$

where $\mathcal{L}$ is the operator acting on β. We similarly define the thermo-acoustic Fant equation as

$$\hat{\mathcal{L}}(Q+Q_f) = -\mathcal{F}(\tau), \tag{6.23}$$

where $\hat{\mathcal{L}}$ is the adjoint to $\mathcal{L}$. Namely, the Fant equation is

$$\bar{\ell}\,\frac{\partial}{\partial\tau}(Q+Q_f) + \frac{i}{2\pi}\int\int_{\infty}^{\infty}(Q+Q_f)(\xi)\left(\frac{c_1\cos(k_1L_1)}{\sin(k_1L_1)} - \frac{c_2\sin(k_2L_2)}{k_2\cos(k_2L_2)}\right)\mathrm{e}^{-i\omega(\xi-\tau)}d\omega d\xi = \mathcal{F}(\tau), \tag{6.24}$$

where substitution of $\mathcal{F}(\tau)$ in Equation 6.21 and an interchange of variables yields the thermo-acoustic Fant equation 6.15. We prove the adjoint relationship by taking the product of Equation 6.24 with

$\beta(\tau)$ to obtain

$$\bar{\ell}\,\frac{\partial}{\partial\tau}\left[\beta(Q+Q_f)\right]+\frac{i}{2\pi}\int\int_{\infty}^{\infty}\left[\beta(\xi)(Q+Q_f)(\xi)\right]\left(\frac{c_1\cos(k_1L_1)}{\sin(k_1L_1)}-\frac{c_2\sin(k_2L_2)}{k_2\cos(k_2L_2)}\right)\mathrm{e}^{-i\omega(\xi-\tau)}d\omega d\xi$$
$$=\beta(\tau)\mathcal{F}(\tau). \tag{6.25}$$

Similarly, we take the product of Equation 6.22 with $(Q+Q_f)(\tau)$ to obtain

$$\bar{\ell}\,\frac{\partial}{\partial\tau}\left[\beta(Q+Q_f)\right]-\frac{i}{2\pi}\int\int_{\infty}^{\infty}\left[\beta(\xi)(Q+Q_f)(\xi)\right]\left(\frac{c_1\cos(k_1L_1)}{\sin(k_1L_1)}-\frac{c_2\sin(k_2L_2)}{k_2\cos(k_2L_2)}\right)\mathrm{e}^{-i\omega(\xi-\tau)}d\omega d\xi$$
$$=(Q+Q_f)(\tau)\frac{\partial G_o}{\partial\tau}. \tag{6.26}$$

Integrating the sum of Equations 6.25 and 6.26 yields

$$B=\int_{-\infty}^{\infty}\beta(\tau)\mathcal{F}(\tau)d\tau=-\int_{-\infty}^{\infty}(Q+Q_f)(\tau)\frac{\partial G_o}{\partial\tau}d\tau, \tag{6.27}$$

which has left and right sides identical to Equation 6.5 after an interchange of variables and integration by parts. Substituting the potential flow approximation for the total enthalpy $B\approx-\partial\varphi^*/\partial t$ and differentiating with respect to spatial variable x_1 yields

$$-\frac{\partial}{\partial t}\left[\frac{\partial\varphi^*}{\partial x_1}\right]\equiv-\frac{\partial}{\partial t}\left[\frac{Q+Q_f}{\mathcal{A}}\right]=-\frac{\partial}{\partial x_1}\int_{-\infty}^{\infty}(Q+Q_f)(\tau)\frac{\partial G_o}{\partial\tau}d\tau. \tag{6.28}$$

Substitution of the right-hand side of Equation 6.22 for $\partial G_o/\partial\tau$, we can write the above equation into the form

$$\frac{i}{2\pi\mathcal{A}}\int_{-\infty}^{\infty}\omega(Q+Q_f)(\tau)\mathrm{e}^{-i\omega(t-\tau)}d\omega=\frac{1}{2\pi\mathcal{A}}\frac{\partial}{\partial t}\int_{-\infty}^{\infty}(Q+Q_f)(\tau)\mathrm{e}^{-i\omega(t-\tau)}d\omega=-\frac{\partial}{\partial t}\left[\frac{Q+Q_f}{\mathcal{A}}\right], \quad (6.29)$$

which is equivalent to the left-hand side of Equation 6.28. Thus, proving the 'adjoint-equation' method and justifying Equation 6.5. The following chapters determine the solution of Equation 6.19 and provide linear and nonlinear example results.

Chapter 7

Application of the linear Fant equation

Initially we limit the application of the Fant equation 6.19 to illustrative calculations of the resonant modes of the idealised burner Configuration III in Figure 3.3 with the characteristic parameters listed in Table 7.1.

In the linearised approximation let $\bar{Q}$, $\bar{Q}_f$ denote the mean values of $Q(t)$, $Q_f(t)$, and set

$$Q(t) = \bar{Q} + \mathrm{Re}\left(\hat{Q}\mathrm{e}^{-i\omega t}\right), \qquad Q_f(t) = \bar{Q}_f + \mathrm{Re}\left(\hat{Q}_f\mathrm{e}^{-i\omega t}\right), \tag{7.1}$$

where $\hat{Q}$, $\hat{Q}_f$ are the corresponding complex amplitudes of time-harmonic oscillations of frequency ω of the perturbation volume velocities through the constrictions and from the flame. In the steady limit $Q(t) \to \bar{Q}$ the Fant equation 6.19 becomes

$$\frac{\rho_1 c_1 - \rho_2 c_2}{\rho_1}\frac{\bar{Q} - \bar{Q}_o}{\mathcal{A}} - \frac{1}{2}\frac{Q_o}{\sigma^2\mathcal{A}_\sigma^2} = \frac{\bar{p}}{\rho_1} - \frac{1}{2}\bar{U}_\sigma^2 = 0, \tag{7.2}$$

where $\bar{p}$ is the steady excess pressure within the upstream duct and $\bar{U}_\sigma$ is the corresponding asymp-

Table 7.1: Idealised duct combustor (Configuration III) parameters

Description	Value
Duct cross-sectional area $\mathcal{A}$	0.011 m^2
Steady upstream source volume velocity $\bar{Q}_o$	0.022 m^3/s
Constriction cross-sectional area $\mathcal{A}_\sigma$	0.0055 m^2
Distance from aperture to duct entrance L_1	0.322 m
Distance from aperture to effective duct exit $\bar{L}_2$	1.142 m
Effective length of burner 'blockage' $\bar{\ell}$	0.022 m
Upstream mean temperature T_1	288 K
Downstream mean temperature T_2	1200 K
Upstream mean density ρ_1	1.214 kg/m^3
Downstream mean density ρ_2	0.292 kg/m^3
Maximum flame power Π_{max}	50 kW/m^3

totic speed of the jets exhausting through the constrictions. Subtracting steady Equation 7.2 from the full Fant equation 6.19, and linearising by taking terms $\hat{Q}^2$ to be negligible, we obtain the characteristic equation for the burner eigenfrequencies [82]

$$k_1\bar{\ell} - \cot(k_1 L_1) + \mathcal{Z}\left(1 + \frac{\hat{Q}_f(\omega)}{\hat{Q}(\omega)}\right)\tan(k_2 L_2) + iM_o\left(\frac{\mathcal{A}}{\sigma\mathcal{A}_\sigma}\right)^2 = 0, \tag{7.3}$$

where $\mathcal{Z} = \rho_2 c_2/\rho_1 c_2$, $k_1 = \omega/c_1$ and $k_2 = \omega/c_2$ are the respective upstream and downstream wave number, and $M_o = U_o/c_1$ is the mean flow Mach number in the upstream duct.

The first term on the left of Equation 7.3 corresponds to an effective increase in the duct length caused by the flame-holder. The second and third terms correspond to acoustic propagation in the respective upstream and downstream duct, as well as acoustic energy production in the third term. The final term arises from unsteady motions of the jet emerging by production of vorticity at the edges of the flame-holder. The magnitude of this effect can be gauged, considering the case of no unsteady heat release.

The characteristic frequencies are real when $M_o = 0$ and when the unsteady heat release from the

flame $\hat{Q}_f = 0$ due to the absence of mean flow dampening and unsteady combustion destabilisation, which would give an imaginary part to the frequency. In the absence of a mean flow and unsteady heat release, the equation governing the characteristic frequencies reduces to

$$\frac{\omega\bar{\ell}}{c_1} - \cot(k_1 L_1) + \mathcal{Z}\tan(k_2 L_2) = 0,$$

which can be solved using the Newton-Raphson method. The lowest order modes have frequency $f = \omega/2\pi \simeq 114,\ 273,\ 473,\ 683\,\text{Hz}$ for the burner of Table 7.1.

7.1 The effect of mean flow

In order to show the damping effect of the mean flow we consider the burner absent of unsteady heat release. The frequency $\omega = \omega(U_o)$ is strictly a function of the inlet flow speed. Taking the derivative of Equation 7.3 with respect to U_o and solving for $d\omega/dU_o$, we find

$$\frac{\partial\omega}{\partial U_o} = \frac{-i}{c_1}\frac{1}{F(\omega)}\left(\frac{\mathcal{A}}{\sigma\mathcal{A}_\sigma}\right)^2, \tag{7.4}$$

where

$$F(\omega) = \frac{\bar{\ell}}{c_1} + \csc^2(k_1 L_1)\frac{L_1}{c_1} + \mathcal{Z}\sec^2(k_2 L_2)\frac{L_2}{c_2}. \tag{7.5}$$

Starting with the characteristic frequencies above having zero imaginary part, we find complex resonance frequencies for successive U_o steps by Runge-Kutta [79,83] four-step integration of Equation 7.4. Figure 7.1 depicts the dependence of low order complex resonance frequencies on the mean inlet flow speed in the absence of unsteady heat input. In each of the four present complex acoustic frequencies,

increasing the mean flow speed in the upstream duct has a stabilising effect as the imaginary part of the frequency becomes increasingly negative with increasing U_o. We also wish to investigate the effect of increasing unsteady power.

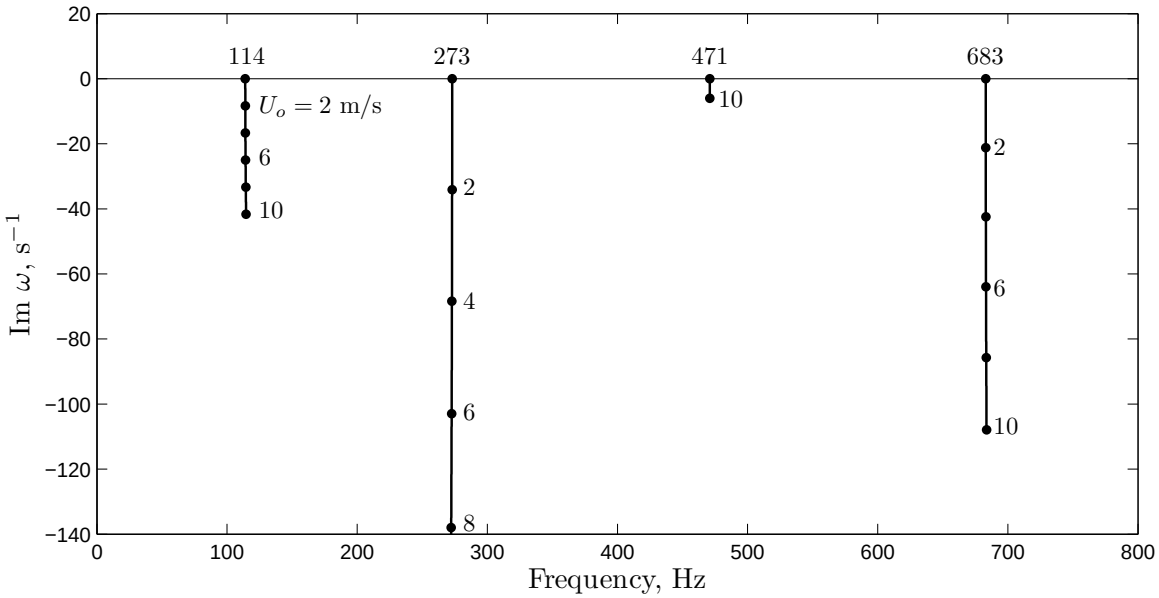

Figure 7.1: Dependence of the low order, linear theory complex resonance frequencies on the mean inlet flow speed $U_o = c_1 M_o$ for the burner of Table 7.1 when there is no unsteady heat input from the flame.

7.2 The effect of unsteady heat release

The influence of unsteady heat release from the flame depends on the modulation of the heat release rate by acoustic fluctuations near the flame-holder. These fluctuations modify the heat release rate of the flame by producing variations in the flame surface area, vortex shedding from the flame-holder, variations in the flame attachment point, *etc* [4,36,40,44,64,84]. In this chapter attention is confined to the first of these mechanisms in the simplest possible manner, sufficient to illustrate its principal influence on the characteristic equation 7.3. The approach is similar to that used in [33].

Let $\bar{q}(x_1)$, $q'(x_1,t)$ respectively denote the mean and unsteady components of heat release per unit length downstream of the flame-holder, so from Equation 6.10 we have

$$\bar{Q}_f = \int_0^{X_f} \frac{\bar{q}(x_1)}{c_p \rho T} dx_1, \qquad Q'_f(t) = \int_0^{X_f} \frac{q'(x_1,t)}{c_p \rho T} dx_1, \tag{7.6}$$

where the region of heat release extends over the interval $0 < x_1 < X_f$.

The heat release fluctuations occur because of changes in the flame front area produced by the unsteady component of the volume velocity $Q(t)$ through the constrictions. For this simple model, suppose that an element of the *steady* flame front, within the interval dx_1, has length $ds(x_1)$. Let small amplitude variations in Q change ds to $ds + d\zeta$, where $\zeta = \zeta(x_1,t)$, therefore

$$q'(x_1,t) = \bar{q}(x_1) \frac{\partial \zeta / \partial x_1}{ds/dx_1}. \tag{7.7}$$

In the simplest approximation we put $ds/dx_1 = 1$, and assume that perturbations in the flame area propagate along the flame at the local mean flow speed $\bar{U}_\sigma$, i.e. $\zeta = \zeta(t - x_1/\bar{U}_\sigma)$. Thus

$$q'(x_1,t) = -\bar{q}(x_1) \frac{1}{\bar{U}_\sigma} \frac{\partial \zeta}{\partial t}(t - x_1/\bar{U}_\sigma) = -\bar{q}(x_1) \frac{Q'}{\bar{Q}_o}(t - x_1/\bar{U}_\sigma), \tag{7.8}$$

where $Q'(t)$ is the unsteady component of the volume velocity.

The overall unsteady volume production rate of the flame $Q'_f(t)$ can now be determined by substitution into the second of Equation 7.6. The resulting integral is approximated by assuming that the main contribution is from within the vicinity of the centroid $x_1 = \ell_q$, say, of the mean heat

release rate, so that $\int_0^{X_f} \bar{q}(x_1) Q'(t - x_1/\bar{U}_\sigma) dx_1 \simeq Q'(t - \ell_q/\bar{U}_\sigma) \int_0^{X_f} \bar{q}(x_1) dx_1$, and therefore

$$\frac{Q'_f(t)}{\bar{Q}_f} \simeq -\frac{Q'(t - \tau_q)}{\bar{Q}_o}, \qquad \tau_q = \frac{\ell_q}{\bar{U}_\sigma}. \tag{7.9}$$

According to this model the heat release ratio $\hat{Q}_f(\omega)/\bar{Q}(\omega)$ in the characteristic equation 7.3 can be replaced by

$$\frac{\hat{Q}_f(\omega)}{\bar{Q}(\omega)} \simeq -\frac{\bar{Q}_f}{\bar{Q}_o} \mathrm{e}^{i\omega\tau_q}. \tag{7.10}$$

The mean volume flow rate of the flame $\bar{Q}_f$ is calculated from Equation 7.6 in terms of the mean flame power $\Pi = \int_0^{X_f} \bar{q}(x_1) dx_1$. The phase lag τ_q is responsible for the destabilisation of the natural acoustic modes of the burner and for the appearance of forced, combustion-driven modes.

In terms of these definitions the characteristic equation 7.3 takes the form

$$k_1 \bar{\ell} - \cot(k_1 L_1) + \mathcal{Z} \left(1 - \frac{\Pi \mathrm{e}^{i\omega\tau_q}}{c_p \rho T \bar{Q}_o} \right) \tan(k_2 L_2) + i M_o \left(\frac{\mathcal{A}}{\sigma \mathcal{A}_\sigma} \right)^2 = 0, \tag{7.11}$$

which we solve taking the derivative with respect to U_o and Π and then solving for $\partial\omega/\partial U_o$ and $\partial\omega/\partial\Pi$ to respectively find

$$\frac{\partial \omega}{\partial U_o} = \frac{-i}{c_1 F(\omega, U_o, \Pi)} \left(\frac{\mathcal{A}}{\sigma \mathcal{A}_\sigma} \right)^2, \tag{7.12}$$

and

$$\frac{\partial \omega}{\partial \Pi} = \frac{\mathcal{Z}}{F(\omega, U_o, \Pi)} \frac{\mathrm{e}^{i\omega\tau_q}}{c_p \rho T Q_o} \tan\left(\omega \frac{L_2}{c_2} \right), \tag{7.13}$$

where

$$F(\omega, U_o, \Pi) = \frac{\bar{\ell}}{c_1} + \csc^2\left(\omega\frac{L_1}{c_1}\right)\frac{L_1}{c_1} + \mathcal{Z}\left(1 - \frac{\Pi e^{i\omega\tau_q}}{c_p\rho T Q_o}\right)\sec^2\left(\omega\frac{L_2}{c_2}\right)\frac{L_2}{c_2} - \mathcal{Z}\left(\frac{i\Pi\tau_q e^{i\omega\tau_q}}{c_p\rho T Q_o}\right)\tan\left(\omega\frac{L_2}{c_2}\right). \tag{7.14}$$

We are interested in determining ω for a range of values Π at several fixed values of U_o. Integrating Equations 7.12 and 7.13 in order to determine ω is path-independent so we integrate first with respect to U_o with fixed power $\Pi = 0$ and then for increasing power between $0 < \Pi < \Pi_{max}$, namely,

$$\omega_1 = \omega_0 + \int_{(U_{o,0},\Pi_0)}^{(U_{o,1},\Pi_0)} \frac{\partial\omega}{\partial U_o} dU_o + \int_{(U_{o,1},\Pi_0)}^{(U_{o,1},\Pi_1)} \frac{\partial\omega}{\partial\Pi} d\Pi, \tag{7.15}$$

Figures 7.2, 7.3, 7.4 respectively depict both the complex natural acoustic (————) and forced combustion (- - - - -) frequencies for the burner of Table 7.1 for the following three configurations

$$U_o = 2.0\,\text{m/s}, \quad \ell_q = 0.8h = 0.04\,\text{m}, \quad \bar{U}_q \approx 6.7\,\text{m/s},$$
$$U_o = 4.0\,\text{m/s}, \quad \ell_q = 1.6h = 0.08\,\text{m}, \quad \bar{U}_q \approx 13.4\,\text{m/s},$$
$$U_o = 6.0\,\text{m/s}, \quad \ell_q = 2.4h = 0.12\,\text{m}, \quad \bar{U}_q \approx 20.1\,\text{m/s}.$$

In each case $\tau_q \simeq 5.97\,\text{ms}$. At $\Pi = 0$ each frequency takes the complex value indicated in Figure 7.1, with negative imaginary part. Each mode is ultimately destabilised (Im $\omega > 0$) by unsteady heating as Π/Π_{max} increases, and the growth rate Im ω is seen to increase rapidly with frequency. It is also clear that the frequency $f = \text{Re}\ \omega/2\pi$ can change significantly. In particular, at $U_o = 2\,\text{m/s}$, the frequency of the lowest order mode initially at $f = 114\,\text{Hz}$ is reduced to 70 Hz when $\Pi = \Pi_{max}$. The same qualitative effects of heating are evident when the mean flow speed is $U_o = 4\,\text{m/s}$ and

$U_o = 6\,\mathrm{m/s}$.

The natural acoustic modes of the burner are unstable when the delay time τ_q between successive peaks in flame heat output is equal to an integral multiple n/f $(n = 1, 2, \ldots)$ of the period $1/f$ of successive acoustic pressure peaks at the flame. More precisely, instability will actually occur provided the heat release rate of the flame has a component in phase with the peak acoustic pressure, which yields the condition $n - \frac{1}{4} < \tau_q f < n + \frac{1}{4}$ [1, 4]. This weakened condition is sufficient to ensure that all of the natural acoustic modes of the burner are ultimately destabilised by unsteady heat release from the flame provided the flame power is large enough.

The delayed response in flame heat release due to forcing by the sound can result in the appearance of an additional set of *forced* combustion modes, which satisfy $\tau_q f = n$ to a good approximation [4, 33, 36]. These modes are absent when $\Pi = 0$ and become rapidly evanescent when $\Pi \to 0$. The forced combustion modes which acquire positive growth are depicted in Figures 7.2-7.4 (- - - - -) (all others are evanescent). The presence of these instabilities implies the existence of an acoustic loop within the burner of the same frequency: $f = 165, 335\,\mathrm{Hz}$, in the first case in Figure 7.2. In Figures 7.3 and 7.4, only the first combustion mode is excited. The rest are evanescent.

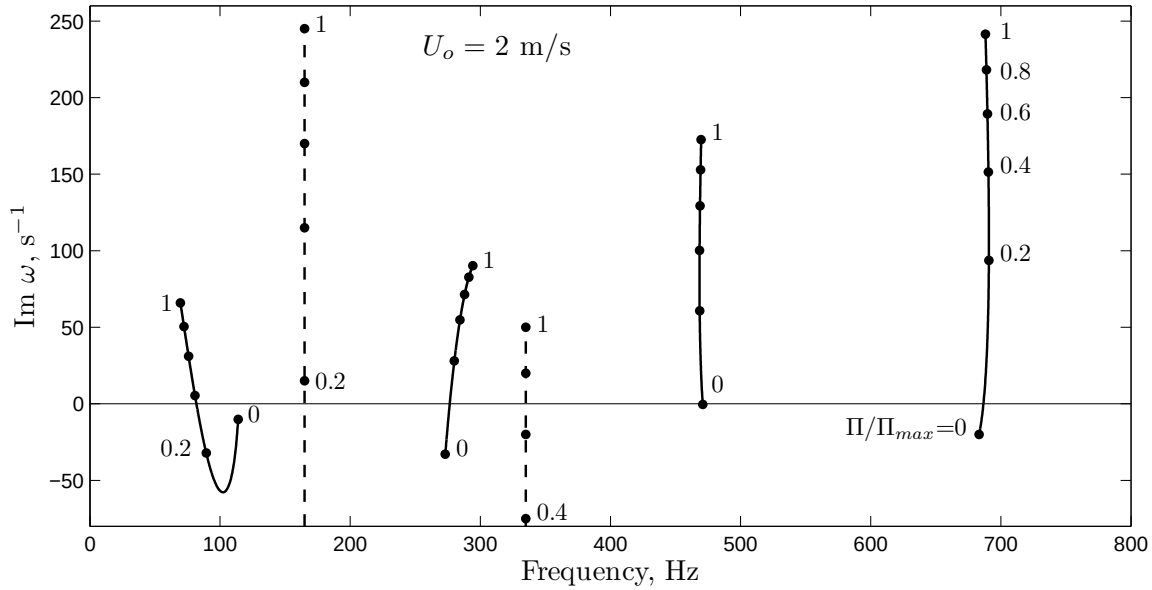

Figure 7.2: Dependence of the low order, linear theory complex resonance frequencies for the burner of Table 7.1 on operating power $\Pi(0 < \Pi < \Pi_{max})$ for $U_o = 2\,\mathrm{m/s}$ and $\ell_q/h = 0.8$: ———— , natural acoustic modes; - - - - - , combustion modes.

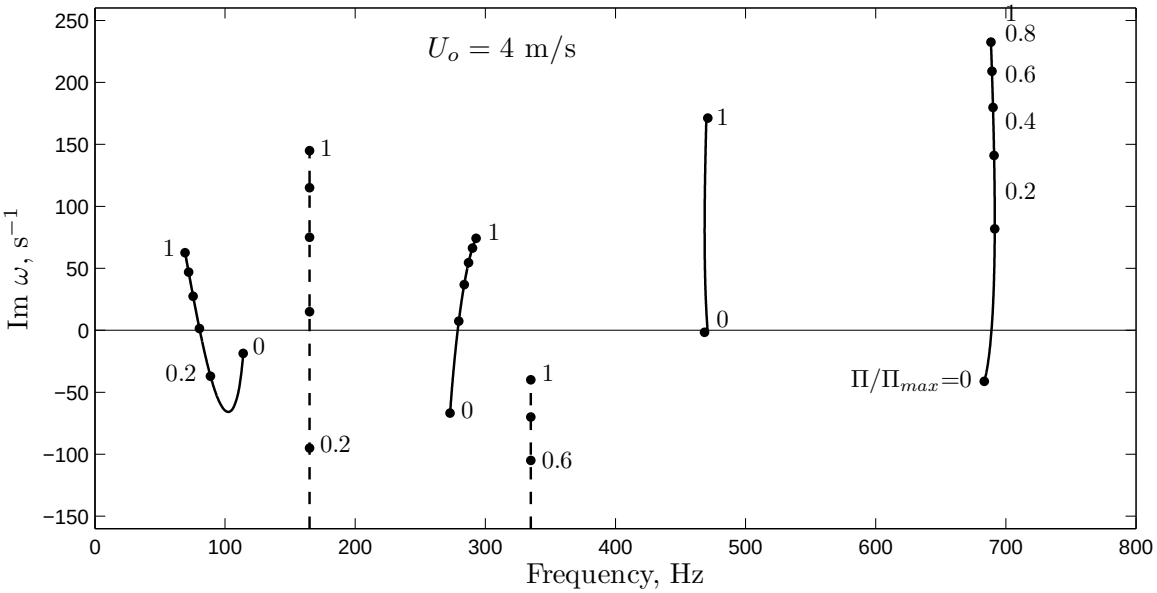

Figure 7.3: Dependence of the low order, linear theory complex resonance frequencies for the burner of Table 7.1 on operating power $\Pi(0 < \Pi < \Pi_{max})$ for $U_o = 4\,\mathrm{m/s}$ and $\ell_q/h = 1.6$: ———— , natural acoustic modes; - - - - - , combustion modes.

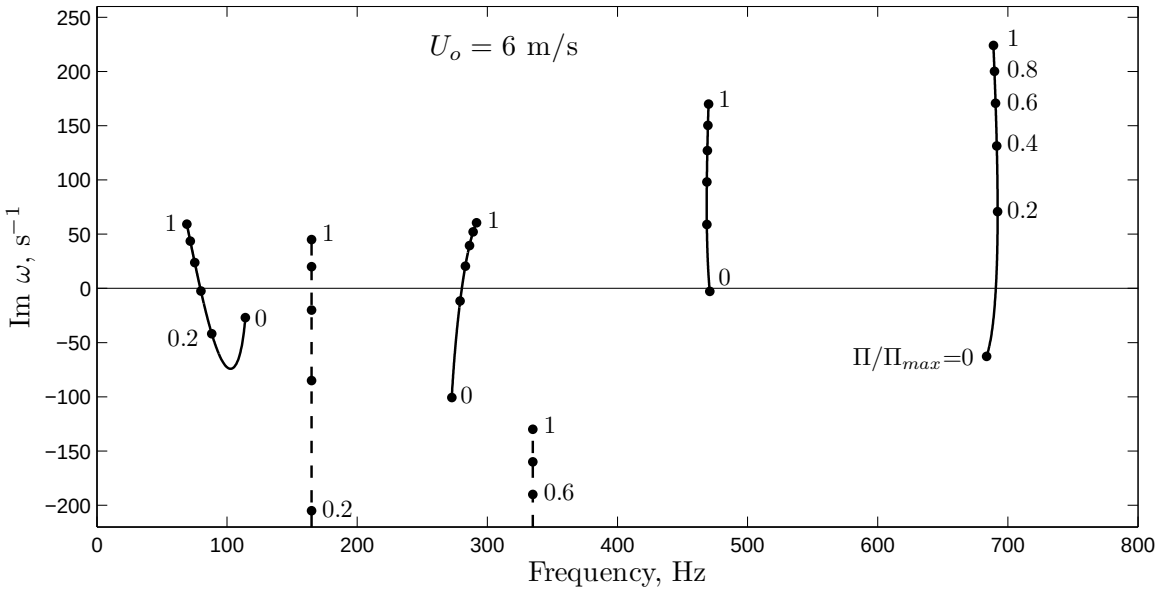

Figure 7.4: Dependence of the low order, linear theory complex resonance frequencies for the burner of Table 7.1 on operating power $\Pi(0 < \Pi < \Pi_{max})$ for $U_o = 6\,\mathrm{m/s}$ and $\ell_q/h = 2.4$: ———— , natural acoustic modes; - - - - - , combustion modes.

Chapter 8

Application of the nonlinear Fant equation

We now consider Fant equation solutions for the downstream limit-cycle volume velocity $Q(t)$ in Configuration III; this can only be observed in nonlinear solutions. Characteristic parameters are listed in Table 8.1.

8.1 The nonlinear heat source

Flame heat release is discussed in detail for for several geometric configurations in [35]; however, the purpose of the present discussion is not necessarily to accurately describe the burner's flame heat release but rather to describe a new model for describing limit-cycle volume velocity oscillations. Dowling [31] describes a nonlinear heat release formulation introduced in Section 2.3 which predicts well when the heat release $Q_f(t)$ and downstream non-flame volume velocity $Q(t)$ make only small-amplitude perturbations about a their mean or 'steady-state' values $\bar{Q}_f$ and $\bar{Q}_o$, respectively.

Table 8.1: Idealised duct combustor (Configuration III) parameters

Description	Value
Duct cross-sectional area $\mathcal{A}$	0.011 m^2
Steady upstream source volume velocity $\bar{Q}_o$	0.022 m^3/s
Constriction cross-sectional area $\mathcal{A}_\sigma$	0.0055 m^2
Distance from aperture to duct entrance L_1	0.322 m
Distance from aperture to effective duct exit $\bar{L}_2$	1.142 m
Effective length of burner 'blockage' $\bar{\ell}$	0.022 m
Upstream mean temperature T_1	288 K
Downstream mean temperature T_2	1200 K
Upstream mean density ρ_1	1.214 kg/m^3
Downstream mean density ρ_2	0.292 kg/m^3
Maximum flame power Π_{max}	50 kW/m^3

Transformation of Equation 2.47 into the frequency domain yields

$$\tau_1 \frac{dQ_f}{dt} + Q_f(t) = -\tilde{Q}_f(Q(t-\tau_2)), \tag{8.1}$$

where time delays τ_1 and τ_2 respectively correspond to dynamic and convective time delays. $\tau_2 = \ell_q/\bar{U}_\sigma$ corresponds to the time delay τ_q in the linear calculations of Chapter 7 and is physically well-understood. The dynamic time delay τ_1 is not very well-understood and is analysed to determine an appropriate value below. $\tilde{Q}_f(t)$ denotes the steady-state value of $Q_f(t)$ and is defined as follows:

$$\tilde{Q}_f(Q(t)) = \begin{cases} 0 & \text{for} \quad Q(t) < 0 \\ \frac{\Pi Q(t)}{c_p \rho T Q_o} & \text{for} \quad 0 < Q(t) < 2\bar{Q}_o \\ \frac{2\Pi}{c_p \rho T} & \text{for} \quad 2\bar{Q}_o < Q(t) \end{cases} \tag{8.2}$$

From our linear calculations [82, 85], we initially predict the oscillations will have frequency $f_o \sim 100$ Hz and use this value to non-dimensionalise time t. In order to understand the effect of the dynamic time delay τ_1 we investigate its behaviour after long time well in to the limit cycle

$tf_o \gg 100$ ($f_o \sim 100$ Hz being an estimated low-order resonant frequency), $Q_f(t)$ is periodic and can be characterised by three parameters: the frequency amplitude of the oscillations, and the mean value about which it oscillates. Although we are concerned with the frequencies constituting the periodic behaviour of volume velocity through the constriction $Q(t)$, we are not so concerned with these frequencies for the heat release volume flux $Q_f(t)$. We are, however, interested in the mean value and amplitude of $Q_f(t)$ at fixed convective time delay τ_2. Figures 8.1 and 8.2 respectively depict the mean value and amplitude of the non-dimensionalised volume velocity of the flame source Q_f at times $tf_o \gg 100$ plotted against the dynamic time delay τ_1 for fixed convective time delay $t_2 = 6\,\text{ms}$, which is approximately the same value used in Chapter 7. We depict these values for four power settings $\Pi = 30,\ 40,\ 50,\ 60\,\text{kW}$. We see that smaller values of τ_1 yield larger mean values of $Q_f(t)$ as well as larger amplitudes.

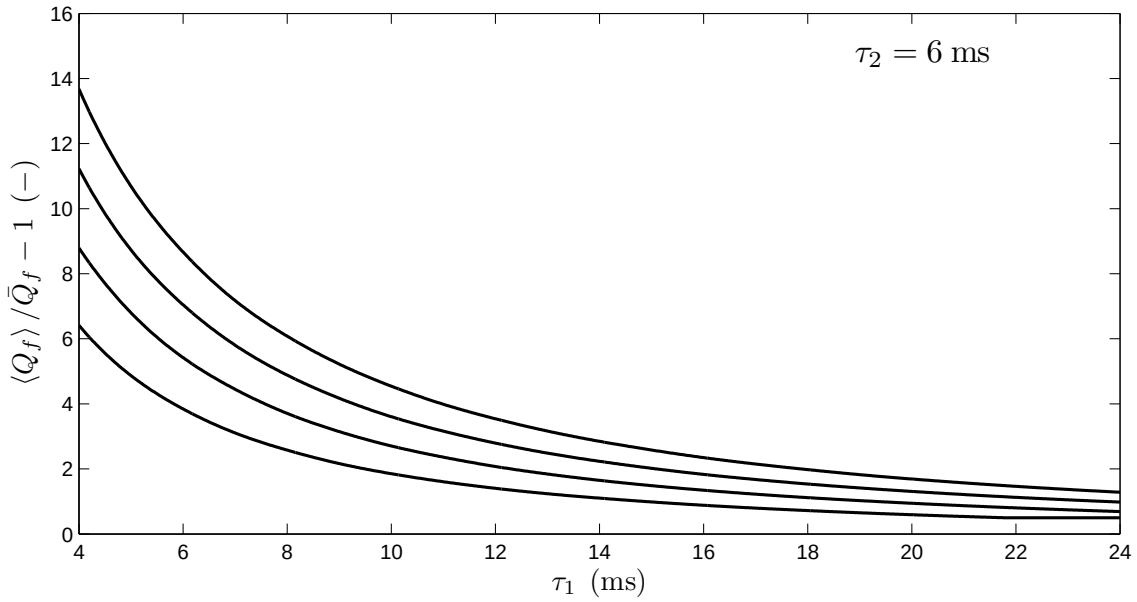

Figure 8.1: Mean value of the non-dimensionalised flame-source volume velocity Q_f plotted against dynamic time delay τ_1 at time $tf_o \gg 100$ for convective time delay $\tau_2 = 6\,\text{ms}$ and power $\Pi = 30,\ 40,\ 50,\ 60\,\text{kW}$.

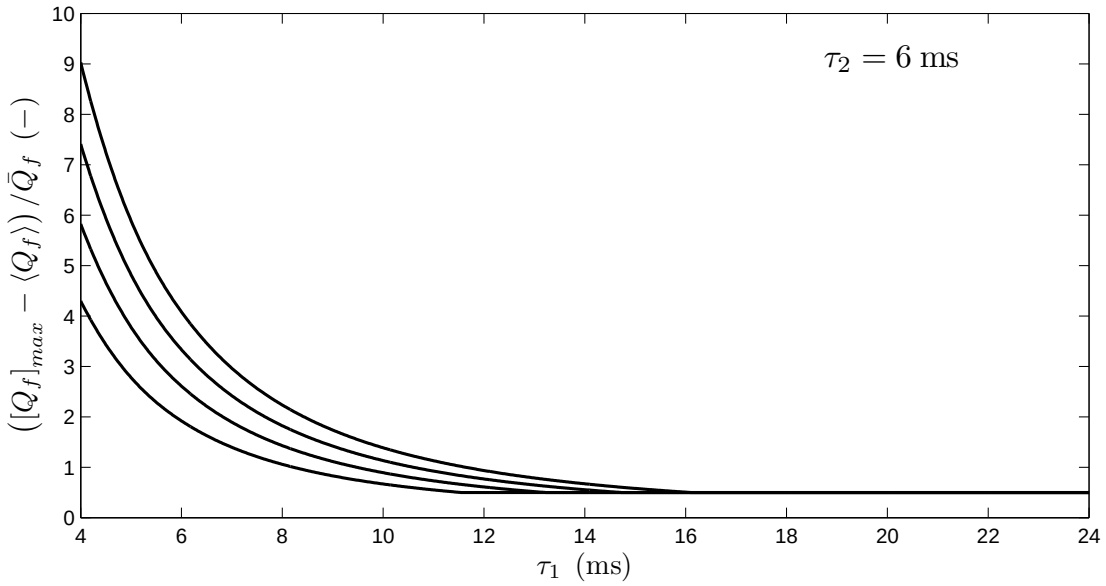

Figure 8.2: Amplitude of oscillations of the non-dimensionalised flame-source volume velocity Q_f plotted against dynamic time delay τ_1 at time $tf_o \gg 100$ for convective time delay $\tau_2 = 6$ ms and power $\Pi = 30,\ 40,\ 50,\ 60$ kW.

8.2 The solution of the nonlinear thermo-acoustic Fant equation

In order to numerically determine the nonlinear solution of the Fant Equation 6.19 having the heat release formulation above, we define a series of first-order differential equations with which we solve for the volume using fourth-order Runge-Kutta integration. We rewrite the Fant Equation 6.19 with

integral terms being on the left-hand side

$$\begin{aligned}\bar{\ell}\,\frac{dQ}{dt} &+ \frac{i}{2\pi}\int\int_{-\infty}^{\infty}(Q(\xi)-\bar{Q}_o)\frac{c_1\cos(k_1L_1)}{\sin(k_1L_1)}\mathrm{e}^{i\omega(\xi-t)}d\omega d\xi \\ &- \frac{i}{2\pi}\int\int_{-\infty}^{\infty}(Q(\xi)-\bar{Q}_o)\frac{\rho_2}{\rho_1}\frac{c_2\sin(k_2L_2)}{\cos(k_2L_2)}\mathrm{e}^{i\omega(\xi-t)}d\omega d\xi \\ &- \frac{i}{2\pi}\int\int_{-\infty}^{\infty}Q_f(\xi)\frac{\rho_2}{\rho_1}\frac{c_2\sin(k_2L_2)}{\cos(k_2L_2)}\mathrm{e}^{i\omega(\xi-t)}d\omega d\xi = -\frac{\mathcal{A}Q|Q|}{2\sigma^2\mathcal{A}_\sigma^2}.\end{aligned} \tag{8.3}$$

Integrals with respect to ω are evaluated by defining a contour in the lower-half ω-plane which is anti-clockwise and passes under all first-order singularities, occurring at modal frequencies $\Omega_n' = n\pi\frac{c_1}{L_1}$ and $\Omega_n = \left(n-\frac{1}{2}\right)\pi\frac{c_2}{L_2}$. We evaluate the residues to find

$$\begin{aligned}\bar{\ell}\,\frac{dQ}{dt} &+ 2\int_{-\infty}^{t}(Q(\xi)-\bar{Q}_o)\frac{c_1^2}{L_1}\left[\sum_{n=1}^{\infty}\cos(\Omega_n'(\xi-t))+\frac{1}{2}\right]d\xi \\ &+ 2\int_{-\infty}^{t}(Q(\xi)-\bar{Q}_o)\frac{\rho_2}{\rho_1}\frac{c_2^2}{L_2}\sum_{n=1}^{\infty}\cos(\Omega_n(\xi-t))d\xi \\ &+ 2\int_{-\infty}^{t}Q_f(\xi)\frac{\rho_2}{\rho_1}\frac{c_2^2}{L_2}\sum_{n=1}^{\infty}\cos(\Omega_n(\xi-t))d\xi = -\frac{\mathcal{A}Q|Q|}{2\sigma^2\mathcal{A}_\sigma^2}.\end{aligned} \tag{8.4}$$

Due to the effect of higher order modes Ω_n' and Ω_n being negligible, we can restrict the modes of interest to a fixed number N. We can rewrite Equation 8.4 in the more compact form

$$\bar{\ell}\,\frac{d\Xi_o}{dt} + X_0 + \sum_{n=1}^{N}(X_n(t)+Y_n(t)) = -\frac{\mathcal{A}Q|Q|}{2\sigma^2\mathcal{A}_\sigma^2}, \tag{8.5}$$

where $\Xi_o(t)$, $X_o(t)$, $X_n(t)$, $Y_n(t)$ are functions respectively defined as follows

$$\begin{aligned}
\Xi_o(t) &= Q(t) - Q_0 \\
X_0(t) &= \int_{-\infty}^{t} (Q(\xi) - \bar{Q}_o)\frac{c_1^2}{L_1} d\xi, \\
X_n(t) &= 2\int_{-\infty}^{t} (Q(\xi) - \bar{Q}_o)\frac{c_1^2}{L_1}\cos(\Omega_n'(\xi - t)) d\xi, \\
Y_n(t) &= 2\int_{-\infty}^{t} (Q(\xi) + Q_f(\xi) - \bar{Q}_o)\frac{\rho_2}{\rho_1}\frac{c_2^2}{L_2}\cos(\Omega_n(\xi - t)) d\xi.
\end{aligned} \tag{8.6}$$

We can collect Equations 8.3, 8.4, 8.5 and 8.6 to define a system of $4N + 3$ differential equations

$$\begin{aligned}
\frac{dX_0}{dt} &= \frac{c_1^2}{L_1}\Xi_o(t), \\
\frac{dX_n}{dt} &= 2\frac{c_1^2}{L_1}\Xi_o(t) + \Omega_n' X_n'(t), \\
\frac{dY_n}{dt} &= 2\frac{\rho_2}{\rho_1}\frac{c_2^2}{L_2}(\Xi_o(t) + Q_f(t)) + \Omega_n Y_n'(t), \\
\frac{dX_n'}{dt} &= -\Omega_n' X_n(t), \\
\frac{dY_n'}{dt} &= -\Omega_n Y_n(t), \\
\frac{d\Xi_o}{dt} &= -\frac{1}{\bar{\ell}}\left(X_0 + \sum_{n=1}^{N}(X_n(t) + Y_n(t)) + \frac{\mathcal{A}}{2\sigma^2\mathcal{A}_\sigma^2}(\Xi_o(t) + \bar{Q}_o)|\Xi_o(t) + \bar{Q}_o|\right), \\
\frac{dQ_f}{dt} &= -\frac{1}{\tau_1}\left(Q_f(t) - \tilde{Q}_f(\Xi_o(t - \tau_2))\right)
\end{aligned} \tag{8.7}$$

where

$$\begin{aligned}
X_n'(t) &= 2\int_{-\infty}^{t} (Q(\xi) - \bar{Q}_o)\frac{c_1^2}{L_1}\sin(\Omega_n'(\xi - t)) d\xi, \\
Y_n'(t) &= 2\int_{-\infty}^{t} (Q(\xi) + Q_f(\xi) - \bar{Q}_o)\frac{\rho_2}{\rho_1}\frac{c_2^2}{L_2}\sin(\Omega_n(\xi - t)) d\xi,
\end{aligned} \tag{8.8}$$

and

$$\tilde{Q}_f(\Xi_o) = \begin{cases} 0 & \text{for} \quad \Xi_o < -\bar{Q}_o \\ \frac{\Pi}{c_{p,1}\rho_1 T_1}\left(\frac{\Xi_o}{\bar{Q}_o}+1\right) & \text{for} \quad -\bar{Q}_o < \Xi_o < \bar{Q}_o \\ \frac{2\Pi}{c_{p,1}\rho_1 T_1} & \text{for} \quad \bar{Q}_o < \Xi_o \end{cases}, \tag{8.9}$$

$$\Omega_n' = n\pi\frac{c_1}{L_1}, \qquad \Omega_n = \left(n-\frac{1}{2}\right)\pi\frac{c_2}{L_2}. \tag{8.10}$$

We choose to restrict the number of mode to $N = 6$. The system of equations is solved using fourth-order Runge-Kutta integration.

We solve the system of equations 8.7, 8.8 numerically using the parameters listed in Table 7.1 and assigning each variable initial value 0. We consider the flame power Π, and the respective dynamic and convective time delays τ_1 and τ_2 to be variable parameters and are chosen for each configuration. In our initial configuration, we chose $\Pi = 25$kW, $\tau_1 = 18$ ms, $\tau_2 = 6$ ms. Initial amplitude oscillations are depicted in Figure 8.3, showing the first ~ 30 periods as the amplitudes approach the limit cycle.

The limit cycle is not fully realised until the number of periods exceeds several hundred ($tf_o \gg 100$). The limit cycle oscillations for the configuration is depicted in Figure 8.4 where the non-dimensionalised time has the range $798 < tf_o < 800$. The amplitude of the oscillations is $Q/Q_o - 1 \approx 3.1$. The oscillations depicted in phase space in Figure 8.5 correspond to the same non-dimensionalised time and demonstrate that the oscillations have reached dynamic stability, i.e. limit cycle oscillations.

The Fourier transform of the non-dimensionalised downstream volume velocity is plotted against frequency in Figure 8.6. We observe the dominating frequencies of the limit cycle are $f \sim 111, 336$ Hz.

Increasing the flame power to the combustor's maximum $\Pi = \Pi_{max}$, we expect to increase the

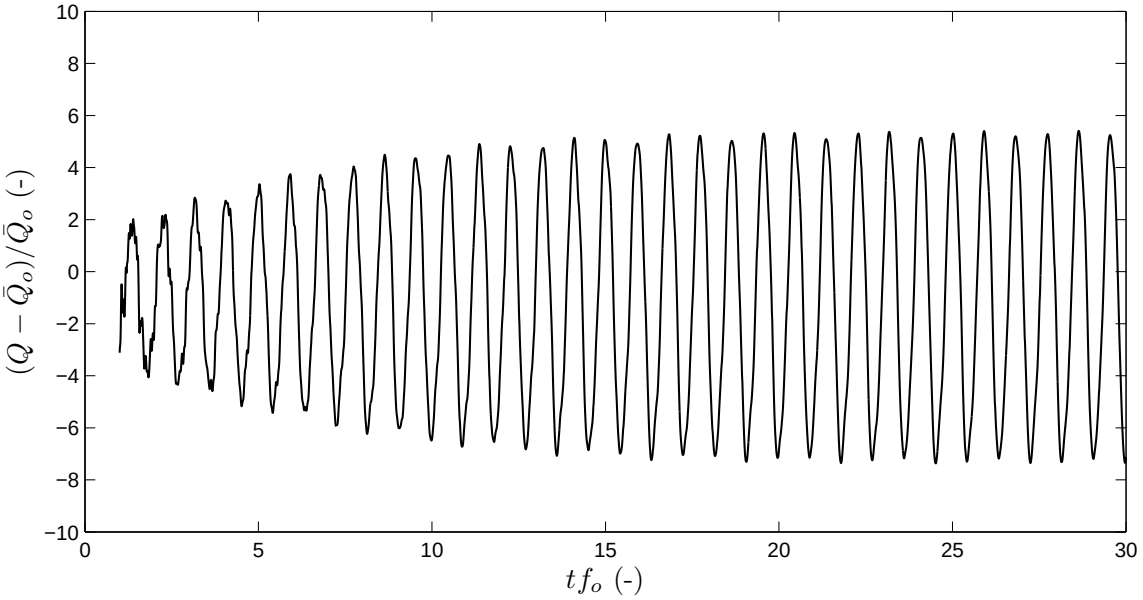

Figure 8.3: Non-dimensionalised volumetric flux plotted against non-dimensionalised time showing the approach to limit cycle oscillations for Configuration III, $\Pi = 25$ kW, $\tau_1 = 18$ ms, $\tau_2 = 6$ ms.

nonlinear behaviour in the limit cycle. We depict in Figure 8.7 the limit cycle oscillations for about two periods for the configuration $\Pi = 50$ kW, $\tau_1 = 18$ ms, $\tau_2 = 6$ ms. The amplitude of the oscillations has effectively doubled, increasing linearly in response to the power increase. The wave shape is also less sinusoidal, also indicative of nonlinearity.

In Figure 8.8 we similarly depict the oscillations in phase space for the configuration with increased effective heat release. The phase lines are thin, indicating dynamic stability and thus limit cycle oscillations. The rate of decay and growth of the oscillations $(1/Q_0 f_o)dQ/dt$ has effectively doubled compared with the previous configuration.

We also depict the Fourier transform of the volumetric flux for the higher heat-release configuration in Figure 8.9. The dominating frequencies have remained effectively unchanged and are $f \sim 110$, 220 Hz

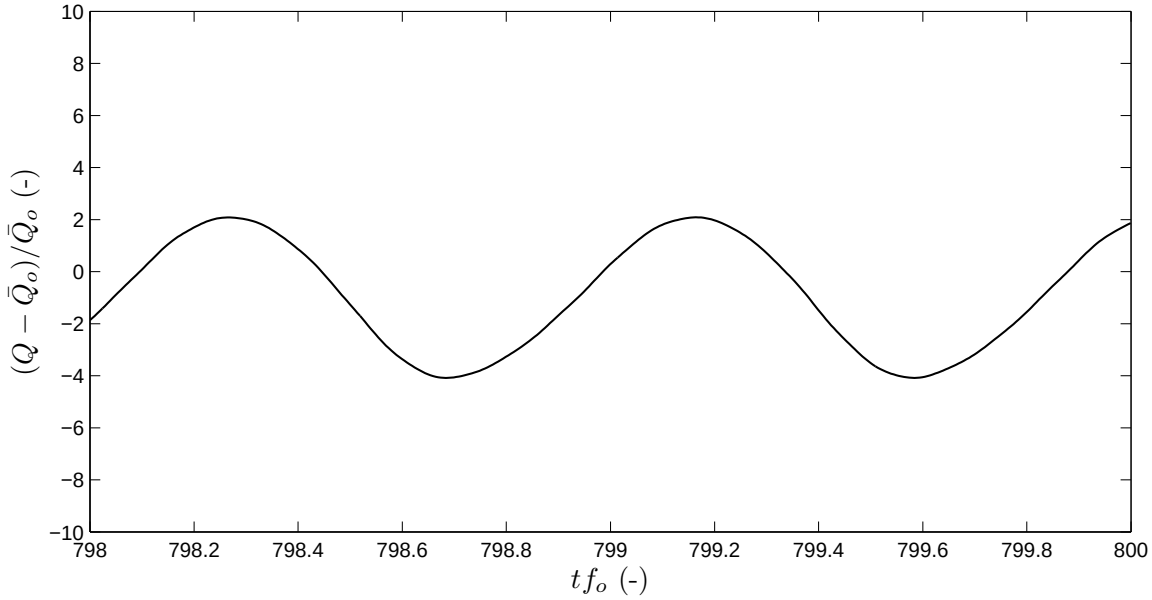

Figure 8.4: Non-dimensionalised volumetric flux plotted against non-dimensionalised time during limit cycle ($tf_o \gg 100$) for Configuration III, $\Pi = 25$ kW, $\tau_1 = 18$ ms, $\tau_2 = 6$ ms.

We are also interested in the effect of reducing the dynamic time delay τ_1. Keeping $\Pi = 50$ kW and $\tau_2 = 6$ ms fixed, we reduced the convective time delay by a third of its original value so that $\tau_1 = 12$ ms. Figure 8.10 depicts the limit cycle oscillations for about two periods. The amplitude of the oscillations have increased by a third compared to the previous configuration, with the longer dynamic time delay. The wave shape is again not as sinusoidal. Figure 8.11 similarly depicts the oscillations in phase space for the reduced convective time delay configuration, showing the rate of growth and decay of the amplitudes has increased by a factor of ~ 2 compared with the previous configuration. Figure 8.12 depicts the Fourier transform of the volume flux. We again observe a slight change in dominating frequencies to $f \sim 108$, 215, 325 Hz.

Investigating the effect of further reducing the dynamic time delay we again keep $\Pi = 50$ kW and $\tau_2 = 6$ ms fixed while reducing the dynamic time delay to $\tau_1 = 6$ ms. Figure 8.13 depicts

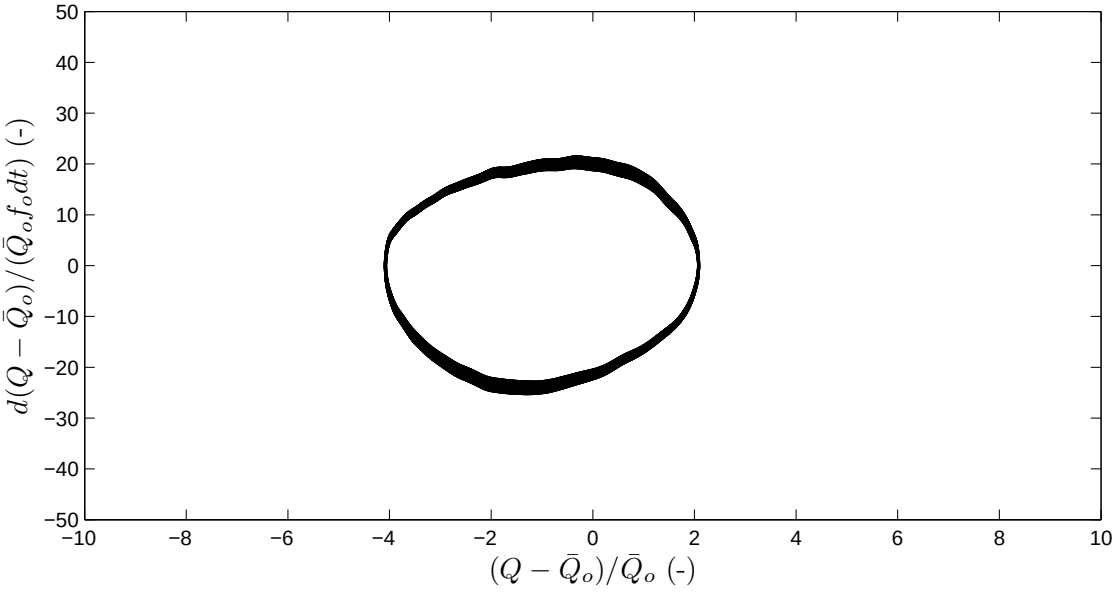

Figure 8.5: Limit cycle oscillations depicted in phase space for the non-dimensionalised volumetric flux during limit cycle ($tf_o \gg 100$) for Configuration III, $\Pi = 25$ kW, $\tau_1 = 18$ ms, $\tau_2 = 6$ ms.

the limit cycle oscillations for about two periods. The amplitude of the oscillations increased by a factor of ~ 2 compared to the previous configuration, with the longer dynamic time delay. The wave shape is again not as sinusoidal. Figure 8.14 similarly depicts the oscillations in phase space for this configuration, showing the rate of growth and decay of the amplitudes has increased by a factor of ~ 2.6 compared with the previous configuration. Figure 8.15 depicts the Fourier transform of the volume flux. We observe the limit cycle frequencies $f \sim$ 105, 209, 315 Hz, which have reduced slightly compared to the previous configuration.

Wanting to observe the effects of increasing the convective time delay τ_2, we keep $\Pi = 50$ kW and $\tau_1 = 6$ ms fixed while increasing the convective time delay by a factor of two so that $\tau_2 = 12$ ms. Figure 8.16 depicts the limit cycle oscillations for about two periods. The amplitude of the oscillations have increased by a factor of ~ 2 compared to the previous configuration, with the shorter combustion

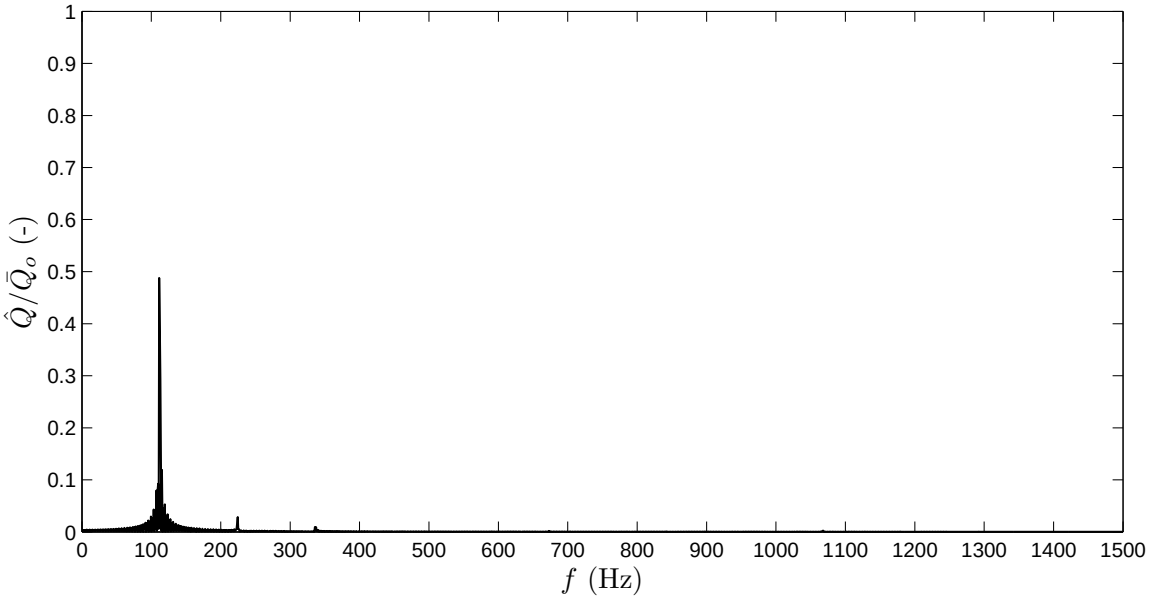

Figure 8.6: Fourier transform of the volume flux plotted against frequency during limit cycle ($tf_o \gg 100$) for Configuration III, $\Pi = 25$ kW, $\tau_1 = 18$ ms, $\tau_2 = 6$ ms.

time delay. Figure 8.17 similarly depicts the oscillations in phase space for the configuration with the reduced dynamic time delay, showing the rate of growth and decay of the amplitudes has increased by a factor of ~ 2 compared with the previous configuration. The phase-plot lines are also significantly thinner compared with the smaller convective time delay configuration, indicating the limit cycle has reached a more refined dynamic stability. Figure 8.18 depicts the Fourier transform of the volume flux. We observe the limit cycle frequencies have changed significantly and are $f \sim 121$, 244, 365 Hz, where the presence of the second harmonic is very small.

We thought it would also be interesting to show the harmonics for the configuration when the dynamic time lag is increased for the higher convective time lag configuration, namely, where $\Pi = 50$ kW, $\tau_1 = 12$ ms, $\tau_2 = 12$ ms. The Fourier transform of the volume flux is depicted in Figure 8.19. We observe the limit cycle frequencies have changed slightly and are now given by

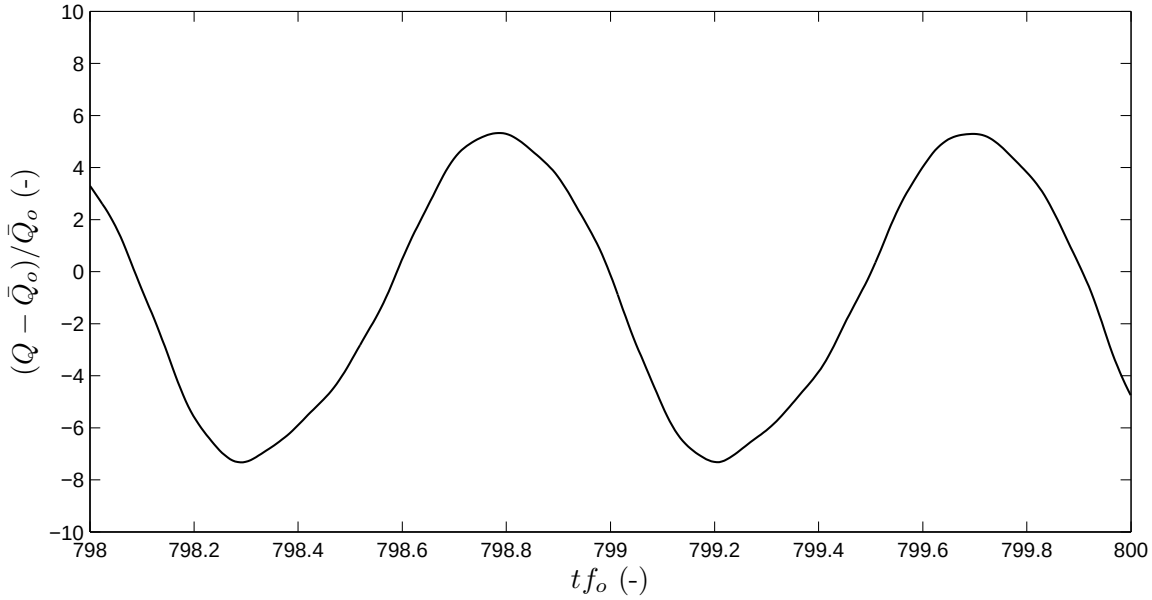

Figure 8.7: Non-dimensionalised volumetric flux plotted against non-dimensionalised time during limit cycle ($tf_o \gg 100$) for Configuration III, $\Pi = 50$ kW, $\tau_1 = 18$ ms, $\tau_2 = 6$ ms.

$f \sim$ 119, 240, 360, 480 Hz.

We conclude that decreasing τ_1 has the effect of significantly increasing the amplitude of limit cycle Q and dQ/dt oscillations while have a small effect on the frequencies of oscillation f. Increasing τ_2 has the effect of significantly increasing the amplitude of limit cycle oscillations, and also on their frequency. The power Π has a linear effect on the amplitude of oscillations.

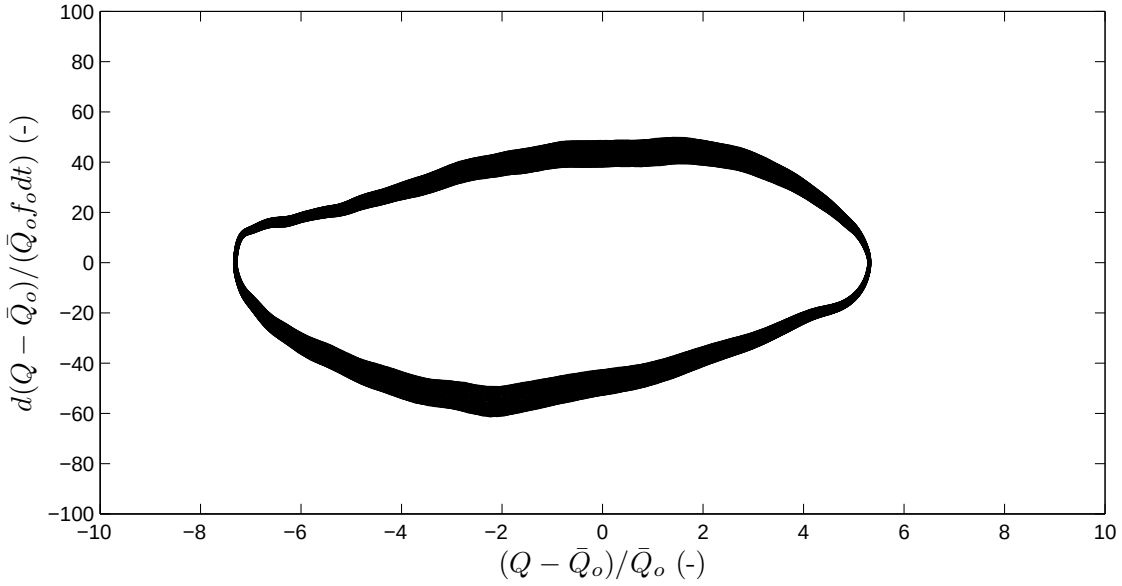

Figure 8.8: Limit cycle oscillations depicted in phase space for the non-dimensionalised volumetric flux during limit cycle ($tf_o \gg 100$) for Configuration III, $\Pi = 50$ kW, $\tau_1 = 18$ ms, $\tau_2 = 6$ ms.

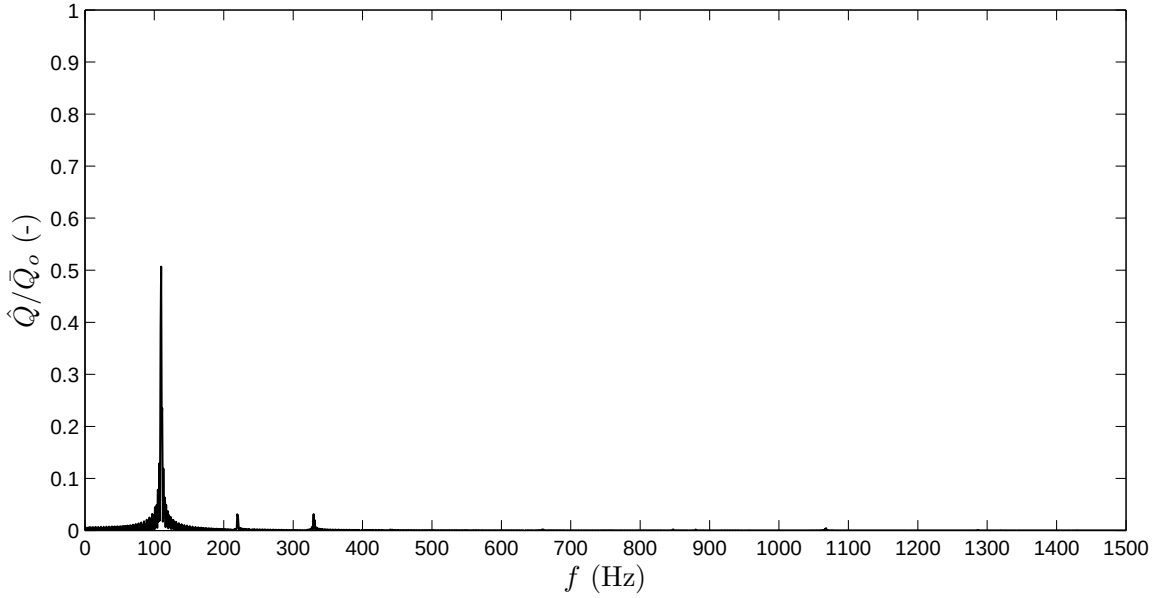

Figure 8.9: Fourier transform of the volume flux plotted against frequency during limit cycle ($tf_o \gg 100$) for Configuration III, $\Pi = 50$ kW, $\tau_1 = 18$ ms, $\tau_2 = 6$ ms.

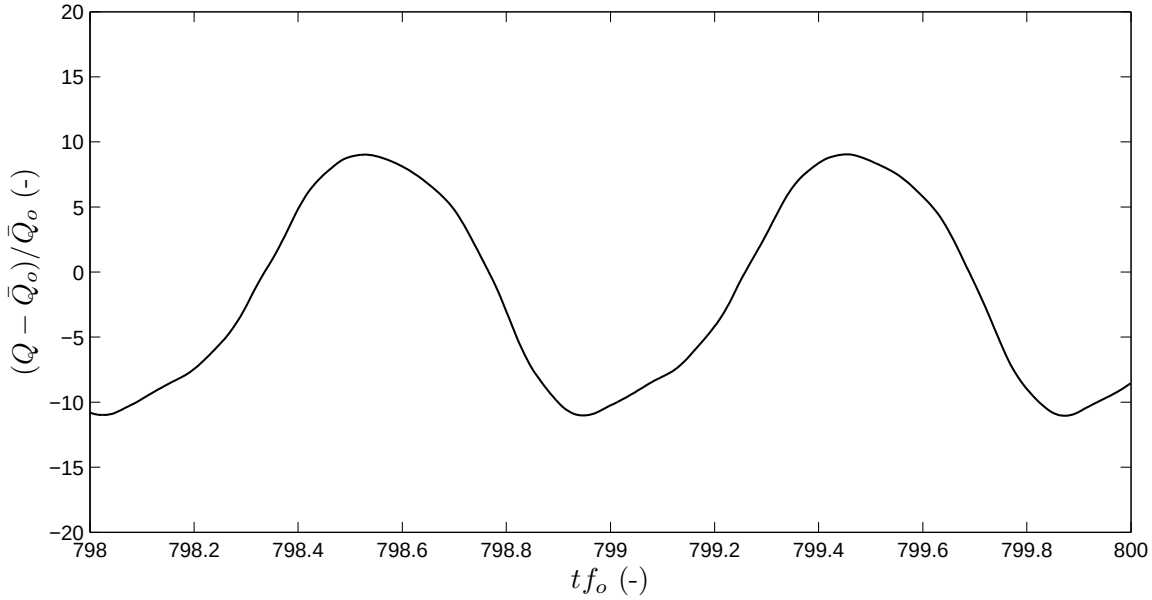

Figure 8.10: Non-dimensionalised volumetric flux plotted against non-dimensionalised time during limit cycle ($tf_o \gg 100$) for Configuration III, $\Pi = 50$ kW, $\tau_1 = 12$ ms, $\tau_2 = 6$ ms.

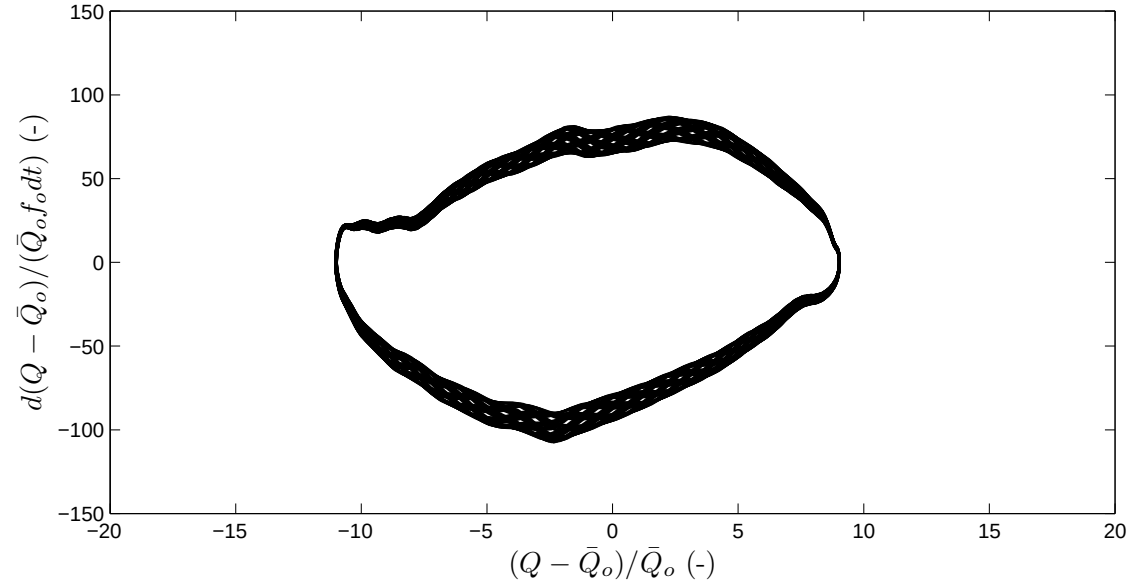

Figure 8.11: Limit cycle oscillations depicted in phase space for the non-dimensionalised volumetric flux during limit cycle ($tf_o \gg 100$) for Configuration III, $\Pi = 50$ kW, $\tau_1 = 12$ ms, $\tau_2 = 6$ ms.

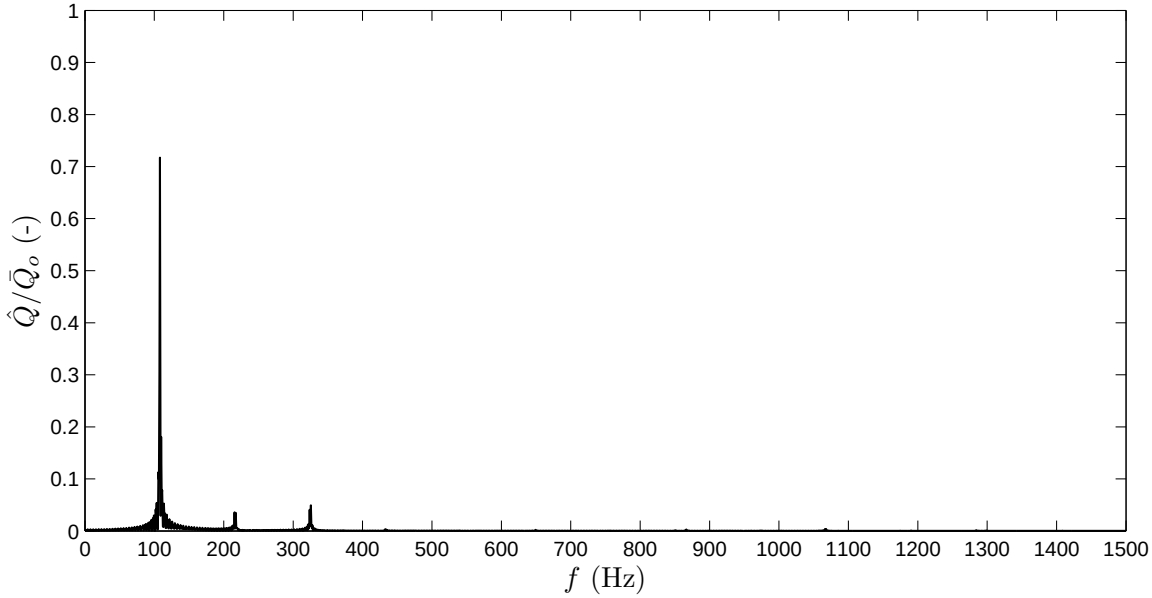

Figure 8.12: Fourier transform of the volume flux plotted against frequency during limit cycle ($tf_o \gg 100$) for Configuration III, $\Pi = 50$ kW, $\tau_1 = 12$ ms, $\tau_2 = 6$ ms.

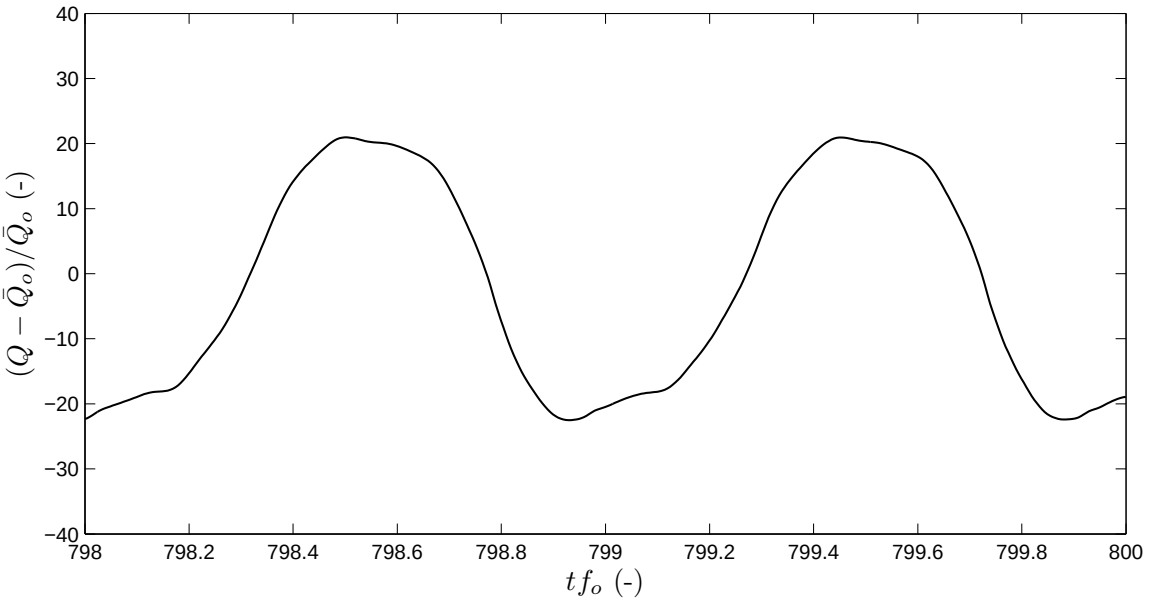

Figure 8.13: Non-dimensionalised volumetric flux plotted against non-dimensionalised time during limit cycle ($tf_o \gg 100$) for Configuration III, $\Pi = 50$ kW, $\tau_1 = 6$ ms, $\tau_2 = 6$ ms.

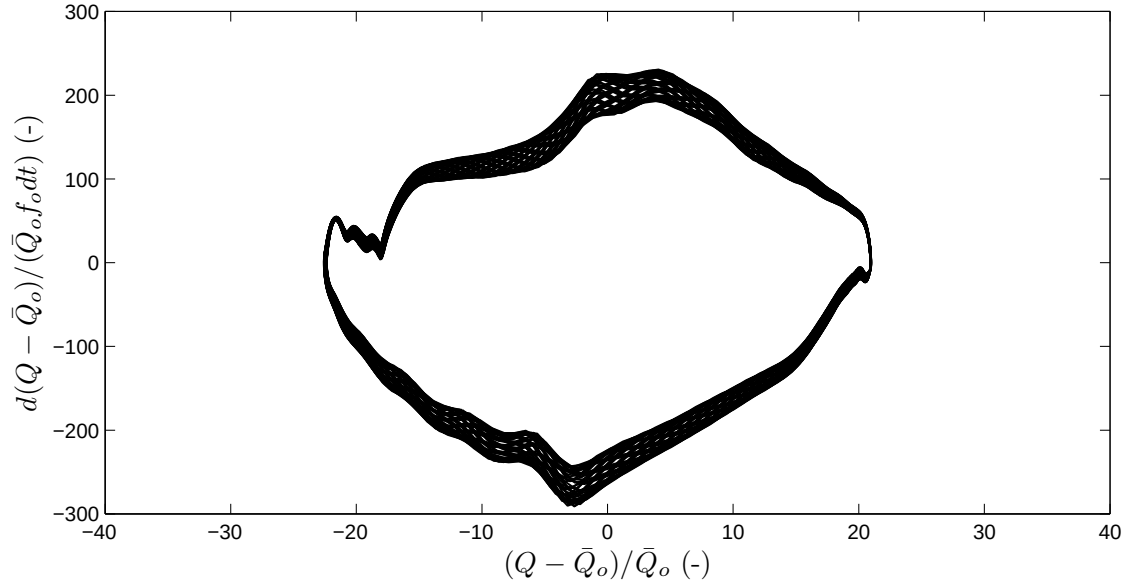

Figure 8.14: Limit cycle oscillations depicted in phase space for the non-dimensionalised volumetric flux during limit cycle ($tf_o \gg 100$) for Configuration III, $\Pi = 50$ kW, $\tau_1 = 6$ ms, $\tau_2 = 6$ ms.

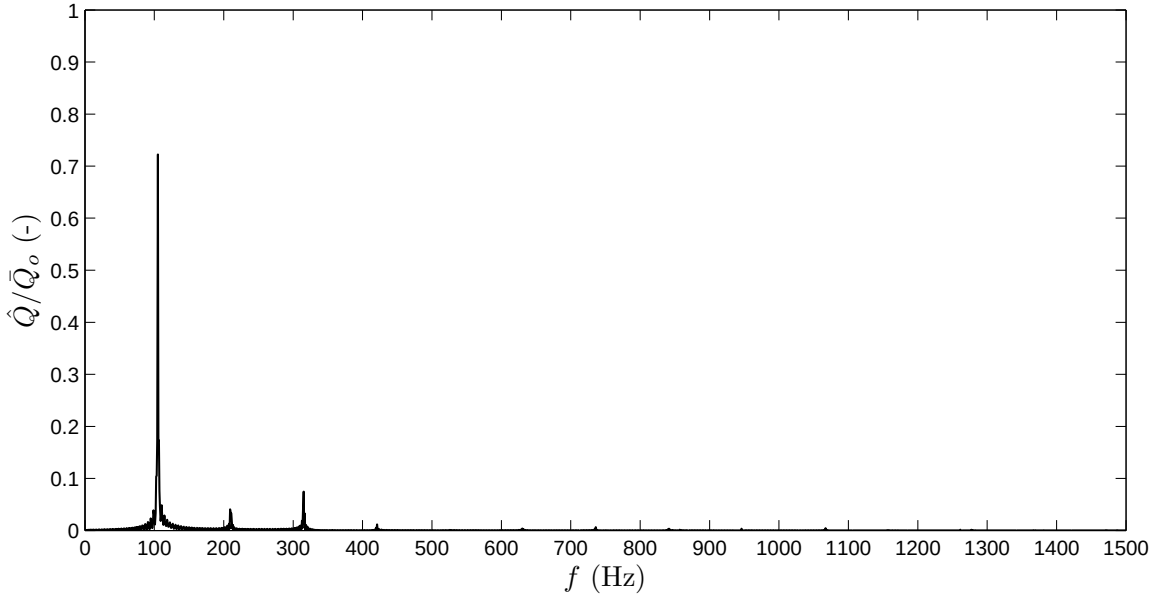

Figure 8.15: Fourier transform of the volume flux plotted against frequency during limit cycle ($tf_o \gg 100$) for Configuration III, $\Pi = 50$ kW, $\tau_1 = 6$ ms, $\tau_2 = 6$ ms.

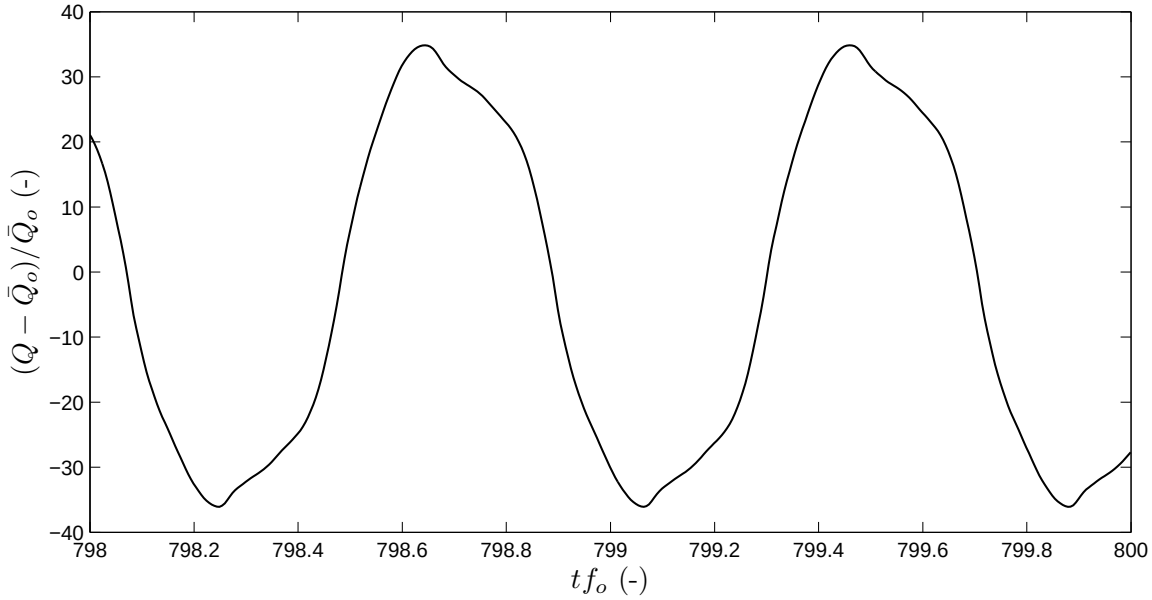

Figure 8.16: Non-dimensionalised volumetric flux plotted against non-dimensionalised time during limit cycle ($tf_o \gg 100$) for Configuration III, $\Pi = 50$ kW, $\tau_1 = 6$ ms, $\tau_2 = 12$ ms.

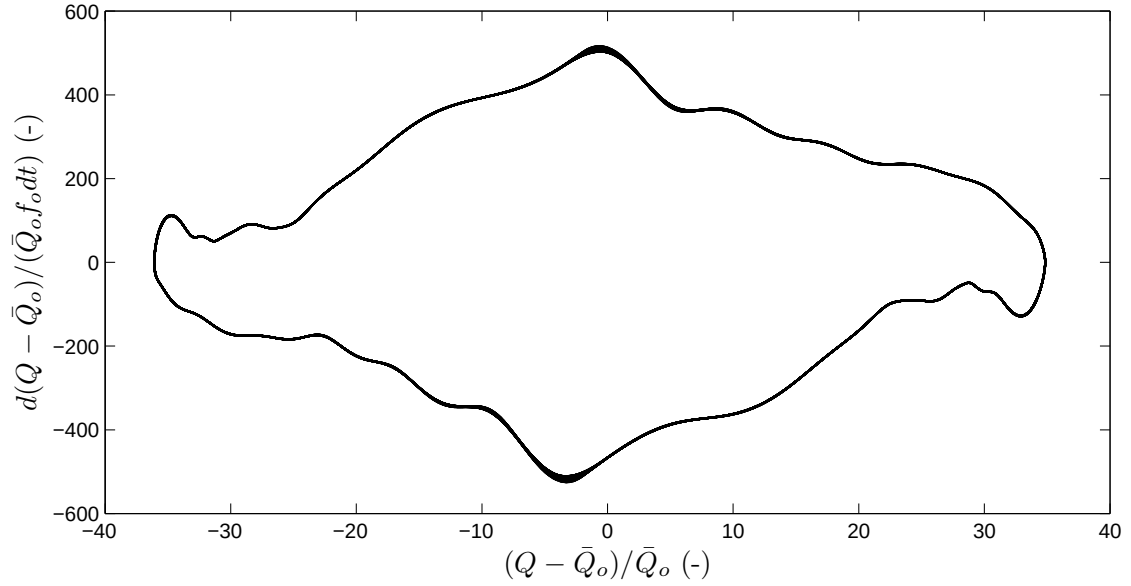

Figure 8.17: Limit cycle oscillations depicted in phase space for the non-dimensionalised volumetric flux during limit cycle ($tf_o \gg 100$) for Configuration III, $\Pi = 50$ kW, $\tau_1 = 6$ ms, $\tau_2 = 12$ ms.

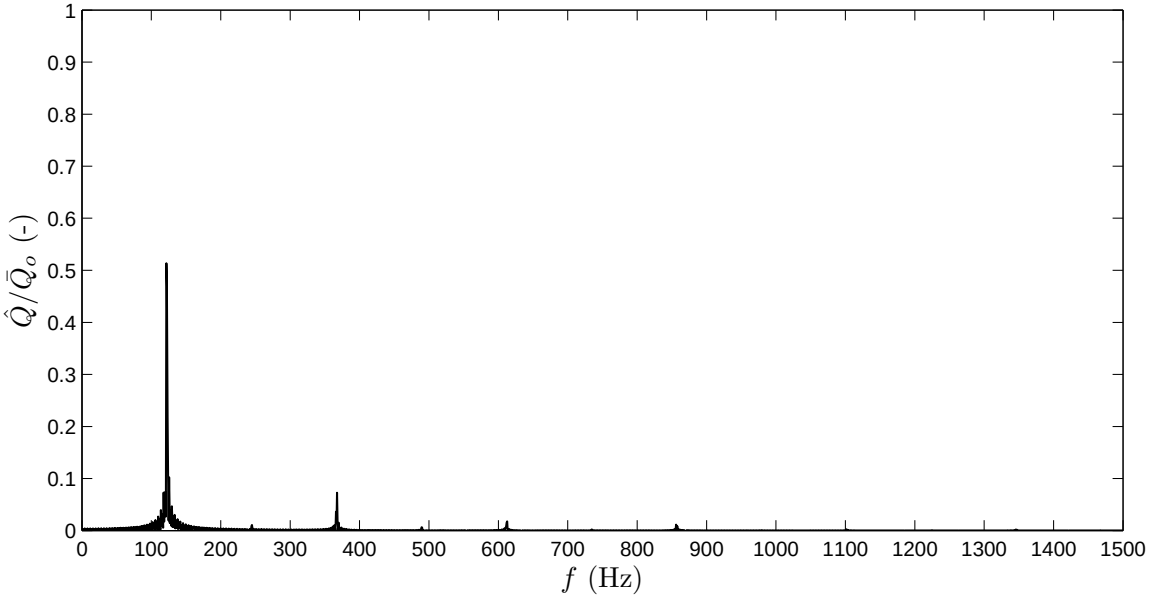

Figure 8.18: Fourier transform of the volume flux plotted against frequency during limit cycle ($tf_o \gg 100$) for Configuration III, $\Pi = 50$ kW, $\tau_1 = 6$ ms, $\tau_2 = 12$ ms.

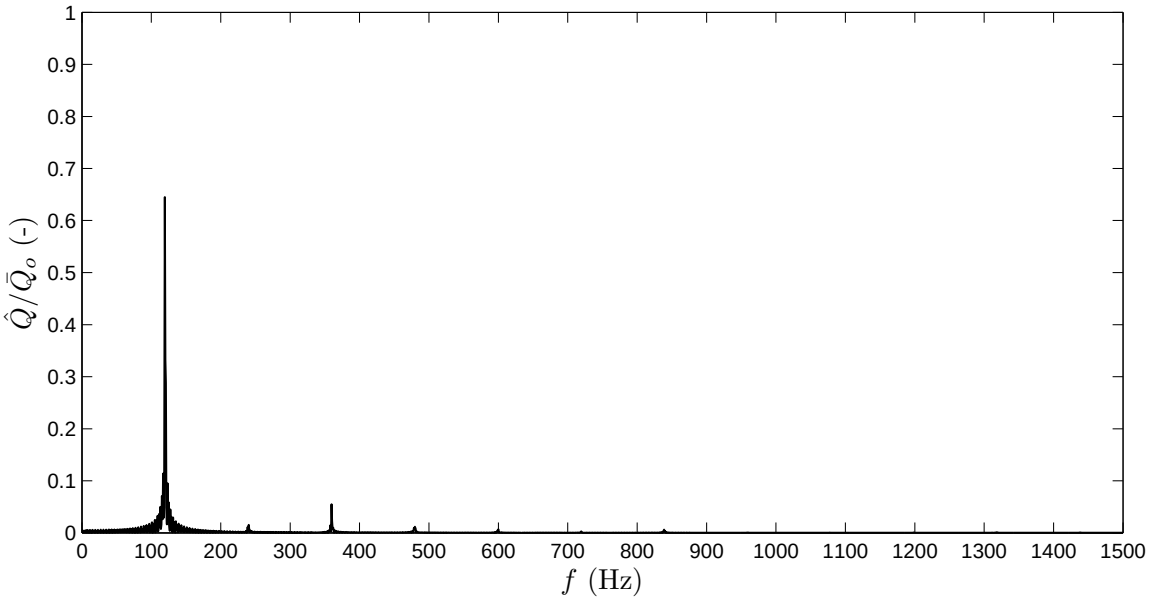

Figure 8.19: Fourier transform of the volume flux plotted against frequency during limit cycle ($tf_o \gg 100$) for Configuration III, $\Pi = 50$ kW, $\tau_1 = 12$ ms, $\tau_2 = 12$ ms.

Chapter 9

Application to the Limousine burner

Application of the Fant equation to the Limousine burner depicted in Figure 3.1 requires modification of the Green's function derived in Section 4.2 in order to take account of the larger cross-sectional area in the downstream section. We also must substitute the blockage length for the idealised combustor calculated analytically in Section 5.6 with that for the Limousine combustor calculated in Section 5.5. The modified Green's function must then be substituted into Equations 6.8-6.12 in order to formulate a modified Fant equation. In this chapter we formulate the modified Green's function and Fant equation and present nonlinear prediction of the downstream volume flux for the Limousine burner.

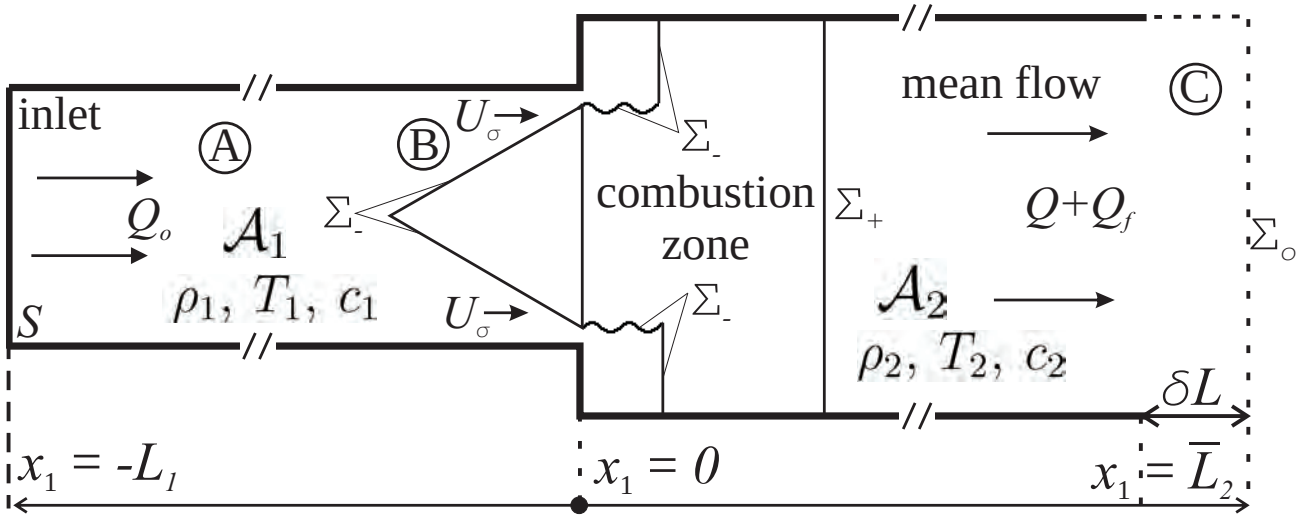

Figure 9.1: Schematic of the Limousine Combustor II depicting source configurations and control surfaces.

9.1 The modified Green's function

The formulation of the Green's function for the Limousine burner Configuration II is similar to that for the idealised combustor. The Green's function takes the same form, as in Equation 4.21,

$$G(\mathbf{x}, \mathbf{y}, t, \tau) = \alpha(\tau, x_1, t) + \beta(\tau, x_1, t) Y(\mathbf{y}),$$

where $\alpha(\tau, x_1, t)$, $\beta(\tau, x_1, t)$ are to be determined. $Y(\mathbf{y})$ satisfies Laplace's equation and $\partial Y / \partial y_n = 0$ on the duct walls. The functional form of Y varies from Equation 4.22 in order to account for the larger cross-sectional area in the downstream section. Y may be assumed to satisfy

$$Y(\mathbf{y}) \sim \begin{cases} y_1, & y_1 > \sqrt{\mathcal{A}_2} \text{ in C}, \\ \frac{\mathcal{A}_2}{\mathcal{A}_1} y_1 - \bar{\ell}, & y_1 < -\sqrt{\mathcal{A}_1} \text{ in A}, \end{cases} \tag{9.1}$$

where $\bar{\ell}$ is the blockage length defined by Equation 5.7 and is given by

$$\bar{\ell} = \int_{X_2}^{\infty} \left(\frac{\partial \varphi^*}{\partial \xi} - 1 \right) d\xi + \int_{-\infty}^{X_2} \left(\frac{\partial \varphi^*}{\partial \xi} - \frac{\mathcal{A}_2}{\mathcal{A}_1} \right) d\xi + \frac{\mathcal{A}_2}{\mathcal{A}_1}(X_2 - X_1).$$

These imply that $G \equiv G(x_1, y_1, t, \tau)$ has the following functional form when $\mathbf{y}$ lies in regions A and C

$$\left.\begin{array}{lll} G = \frac{\mathcal{A}_2}{\mathcal{A}_1}\alpha - \bar{\ell}, & \partial G/\partial y_1 = \frac{\mathcal{A}_2}{\mathcal{A}_1}\beta, & y_1 \to -0 \\ G = \alpha, & \partial G/\partial y_1 = \beta & y_1 \to +0 \end{array}\right\}. \tag{9.2}$$

Therefore, we can put

$$\begin{array}{ll} G(x_1, y_1, t, \tau) = -\frac{1}{2\pi}\frac{\mathcal{A}_2}{\mathcal{A}_1} \int \int_{\infty}^{\infty} \frac{\beta(\xi, x_1, t)\cos[k_1(y_1 + L_1)]}{k_1 \sin(k_1 L_1)} \mathrm{e}^{i\omega(\tau - \xi)} d\omega d\xi & \text{for } \mathbf{y} \text{ in A,} \\ G(x_1, y_1, t, \tau) = G_o(x_1, y_1, t, \tau) + \frac{1}{2\pi} \int \int_{\infty}^{\infty} \frac{\beta(\xi, x_1, t)\sin[k_2(y_1 + L_2)]}{k_2 \sin(k_2 L_2)} \mathrm{e}^{i\omega(\tau - \xi)} d\omega d\xi & \text{for } \mathbf{y} \text{ in C,} \end{array} \tag{9.3}$$

where

$$\begin{array}{rl} G_o(x_1, y_1, t, \tau) = & -\frac{1}{2\pi\mathcal{A}_2} \int_{-\infty}^{\infty} \{H(x_1 - y_1)\cos(k_2 y_1)\sin[k_2(x_1 - L_2)] \\ & + H(y_1 - x_1)\cos(k_2 x_1)\sin[k_2(y_1 - L_2)]\} \frac{\mathrm{e}^{-i\omega(t-\tau)}}{k_2 \cos(k_2 L_2)} d\omega, \end{array} \tag{9.4}$$

which is again the Green's function corresponding to a source located at the flame-holder with the constriction assumed to be closed. The implied Green's function condition above $G \to \frac{\mathcal{A}_2}{\mathcal{A}_1}\alpha - \bar{\ell}$, α respectively as $y_1 \to \mp 0$ yield consistency conditions which can be used to determine the following functional forms of α and β:

$$\alpha(\tau, x_1, t) = \bar{\ell}\,\beta(\tau, x_1, t) - \frac{1}{2\pi}\frac{\mathcal{A}_2}{\mathcal{A}_1} \int \int_{\infty}^{\infty} \beta(\tau, x_1, t) \frac{\cos(k_1 L_1)}{k_1 \sin(k_1 L_1)} \mathrm{e}^{-i\omega(\xi - \tau)} d\omega d\xi, \tag{9.5}$$

$$\begin{aligned}\bar{\ell}\,\beta(\tau,x_1,t) - \frac{1}{2\pi}\int\int_{\infty}^{\infty}\beta(\tau,x_1,t)\left(\frac{\mathcal{A}_2}{\mathcal{A}_1}\frac{\cos(k_1L_1)}{k_1\sin(k_1L_1)} - \frac{\sin(k_2L_2)}{k_2\cos(k_2L_2)}\right)\mathrm{e}^{-i\omega(\xi-\tau)}d\omega d\xi \\ = G_o(x_1,0,t,\tau) \equiv -\frac{1}{2\pi\mathcal{A}_2}\int_{-\infty}^{\infty}\frac{\sin[k_2(x_1-L_2)]}{k_2\cos(k_2L_2)}\mathrm{e}^{-i\omega(\xi-\tau)}d\omega.\end{aligned} \tag{9.6}$$

9.2 The modified Fant equation

We derive the Fant equation for the Limousine combustor using the same methodology as in Section 6.1. We substitute G_o from Equation 9.6 into Equation 6.5,

$$B(x_1,t) = \int_{-\infty}^{\infty}\frac{\partial}{\partial\tau}(Q_f+Q)(\tau)G_o(x_1,0,t,\tau)d\tau, \qquad x_1 > \sqrt{\mathcal{A}_2},$$

to yield

$$\begin{aligned}B(x_1,t) = \int_{-\infty}^{\infty}\beta(\tau,x_1,t)\Bigg[\bar{\ell}\,\frac{\partial}{\partial\tau}(Q+Q_f)(\tau) \\ +\frac{i}{2\pi}\int\int_{-\infty}^{\infty}(Q+Q_f)(\xi)\left(\frac{\mathcal{A}_2}{\mathcal{A}_1}\frac{c_1\cos(k_1L_1)}{\sin(k_1L_1)} - \frac{c_2\sin(k_2L_2)}{\cos(k_2L_2)}\right)\mathrm{e}^{i\omega(\xi-\tau)}d\omega d\xi\Bigg]d\tau.\end{aligned} \tag{9.7}$$

We can again assume the total enthalpy $B = B_o + B_\sigma + B_f$ is the sum of three component enthalpies originating from the respective inlet volume velocity Q_o, the momentum and thermal mixing over the combustion zone, and from the flame heat release.

The enthalpy contributions from the inlet volume velocity B_o, the momentum and thermal mixing B_σ, and the flame heat source B_f are respectively reformulated using the Limousine burner Green's function in Section 9.1; these are found to be

$$B_o(x_1,t) = \frac{ic_1}{2\pi}\frac{\mathcal{A}_2}{\mathcal{A}_1}\int\int\int_{-\infty}^{\infty}\frac{\beta(\tau,x_1,t)Q_o(\xi)}{\sin(k_1L_1)}\mathrm{e}^{i\omega(\xi-\tau)}d\omega d\xi d\tau, \tag{9.8}$$

$$B_\sigma(x_1,t) = -\int_{-\infty}^{\infty}\int_V \beta(\tau,x_1,t)\left(\nabla Y\cdot[\boldsymbol{\omega}\wedge\mathbf{v}-(T\nabla s)'+\nu\,\mathrm{curl}\,\boldsymbol{\omega}]\right)(\mathbf{y},\tau)d^3\mathbf{y}d\tau, \tag{9.9}$$

$$B_f(x_1,t) = \int_{-\infty}^{\infty}\beta(\tau,x_1,t)\left[\bar{\ell}\,\frac{\partial Q_f}{\partial\tau}(\tau)+\frac{ic_1}{2\pi}\frac{\mathcal{A}_2}{\mathcal{A}_1}\int\int_{-\infty}^{\infty}\frac{Q_f(\xi)\cos(k_1L_1)}{\sin(k_1L_1)}\mathrm{e}^{i\omega(\xi-\tau)}d\omega d\xi\right]d\tau. \tag{9.10}$$

We find that the net acoustic field is given by

$$\begin{aligned}B(x_1,t) = \int_{-\infty}^{\infty}\beta(\tau,x_1,t)\Bigg[&\bar{\ell}\,\frac{\partial Q_f}{\partial\tau}(\tau)+\frac{ic_1}{2\pi}\frac{\mathcal{A}_2}{\mathcal{A}_1}\int\int_{-\infty}^{\infty}(Q_f(\xi)\cos(k_1L_1)+Q_o(\xi))\frac{\mathrm{e}^{i\omega(\xi-\tau)}}{\sin(k_1L_1)}d\omega d\xi\\ &-\int_V\left(\nabla Y\cdot[\boldsymbol{\omega}\wedge\mathbf{v}-T\nabla s+\nu\,\mathrm{curl}\,\boldsymbol{\omega}]\right)(\mathbf{y},\tau)d^3\mathbf{y}\Bigg]d\tau.\end{aligned} \tag{9.11}$$

Equating the total enthalpies in Equations 9.7 and 9.11 yields the thermo-acoustic Fant equation for the Limousine burner

$$\begin{aligned}\bar{\ell}\,\frac{dQ}{dt}+\frac{i}{2\pi}\int\int_{-\infty}^{\infty}Q(\xi)\left(\frac{\mathcal{A}_2}{\mathcal{A}_1}\frac{c_1\cos(k_1L_1)}{\sin(k_1L_1)}-\frac{c_2\sin(k_2L_2)}{\cos(k_2L_2)}\right)\mathrm{e}^{i\omega(\xi-t)}d\omega d\xi&\\ =\frac{i}{2\pi}\int\int_{-\infty}^{\infty}\left(\frac{\mathcal{A}_2}{\mathcal{A}_1}\frac{c_1Q_o(\xi)}{\sin(k_1L_1)}+\frac{c_2Q_f(\xi)\sin(k_2L_2)}{\cos(k_2L_2)}\right)\mathrm{e}^{i\omega(\xi-t)}d\omega d\xi&\\ -\int_V\left(\nabla Y\cdot[\boldsymbol{\omega}\wedge\mathbf{v}-(T\nabla s)'+\nu\,\mathrm{curl}\,\boldsymbol{\omega}]\right)(\mathbf{y},t)d^3\mathbf{y}.&\end{aligned} \tag{9.12}$$

Proceeding further, we assume the combustion zone in the Limousine burner is quasi-static, equivalent to assuming it is acoustically compact ($f \ll c_1\ell_s/\mathcal{A}_2 \approx 6800\,\mathrm{Hz}$). In Figure 9.1, we show that the combustion zone is bounded by the control surface $\Sigma = \Sigma_- + \Sigma_+$. Σ_+ is a plane cross-section downstream of the constriction, where the steady and unsteady flows are nominally parallel to the x_1-axis and of infinitesimal Mach number. Σ_- is upstream from Σ_+ and consists of the two upstream edges of the flame-holder, two vortex sheets originating at the edges of the flame-holder and defining the edge of the separated flows, and a vertical section just downstream of the flame-holder where jet

velocities have become uniform and parallel to the wall. The pressure in the jet varies significantly but in the quasi-static approximation, it must be equal to p' on the interface portion of the control surface Σ_- on which the flow speed is uniform and equal to $U_\sigma(t)$.

Neglecting $\partial\mathbf{v}/\partial t$ on the left of linearised enthalpic momentum equation 6.1, and noting the divergence theorem, the final integral on the right of Equation 9.12 can be replaced by

$$-\int_V \nabla Y \cdot \nabla B d^3\mathbf{y} = \oint_{\Sigma_- + \Sigma_+} B\nabla Y \cdot d\mathbf{S} = (B_+ - B-)\mathcal{A}_2, \tag{9.13}$$

noting that $-\oint_{\Sigma_-} \nabla Y \cdot d\mathbf{S} = \oint_{\Sigma_+} \nabla Y \cdot d\mathbf{S} = \mathcal{A}_2$, and where $B_\pm$ are the respective values of B on $\Sigma_\pm$. In formula 9.13 we can take $B_+ = p'/\rho_2$, where the mean flow velocity is negligible and the unsteady pressure p' is the uniform quasi-static pressure in the combustion region. Over the interface portions of Σ_- the velocity is constant in magnitude and equal to $U_\sigma(t)$ so that $B_- = p'/\rho_1 + \frac{1}{2}U_\sigma^2$. The volume flux Q through the constriction is initially carried by the jets so $Q = \sigma\mathcal{A}_\sigma U_\sigma$, where $\sigma \simeq 0.6$. Therefore,

$$\mathcal{A}_2(B_+ - B_-) = \frac{ic_2}{2\pi}\left(\frac{\rho_2}{\rho_1} - 1\right)\int\int_{-\infty}^{\infty}(Q_f + Q)(\xi)\frac{\sin(k_2 L_2)}{\cos(k_2 L_2)}\mathrm{e}^{i\omega(\xi - t)}d\omega d\xi - \frac{\mathcal{A}_2 Q^2}{2\sigma^2\mathcal{A}_\sigma^2}, \tag{9.14}$$

where B_+ has been calculated in terms of Q and Q_f from Equation 6.5 (using expression 9.6 for G_o).

Substitution of Equation 9.14 into Equation 9.12 yields the quasi-static Fant equation approxi-

mation

$$\rho_1 \bar{\ell}\,\frac{dQ}{dt} + \frac{i}{2\pi}\int\int_{-\infty}^{\infty} Q(\xi)\left(\frac{\mathcal{A}_2}{\mathcal{A}_1}\frac{\rho_1 c_1\cos(k_1L_1)}{\sin(k_1L_1)} - \frac{\rho_2 c_2\sin(k_2L_2)}{\cos(k_2L_2)}\right)\mathrm{e}^{i\omega(\xi-t)}d\omega d\xi$$
$$= \frac{i}{2\pi}\int\int_{-\infty}^{\infty}\left(\frac{\mathcal{A}_2}{\mathcal{A}_1}\frac{\rho_1 c_2 Q_o(\xi)}{\sin(k_1L_1)} + \frac{\rho_2 c_2 Q_f(\xi)\sin(k_2L_2)}{\cos(k_2L_2)}\right)\mathrm{e}^{i\omega(\xi-t)}d\omega d\xi - \frac{\rho_1\mathcal{A}_2Q^2}{2\sigma^2\mathcal{A}_\sigma^2}. \tag{9.15}$$

Taking account of the same generalisation and assumption discussed in Section 6.1, about reverse flow and constant inflow, respectively, we cast the quasi-static approximation of the thermo-acoustic Fant equation for the Limousine burner into the following final form

$$\bar{\ell}\,\frac{dQ}{dt} + \frac{i}{2\pi}\int\int_{-\infty}^{\infty}(Q(\xi)-\bar{Q}_o)\left(\frac{\mathcal{A}_2}{\mathcal{A}_1}\frac{c_1\cos(k_1L_1)}{\sin(k_1L_1)} - \frac{\rho_2}{\rho_1}\frac{c_2\sin(k_2L_2)}{\cos(k_2L_2)}\right)\mathrm{e}^{i\omega(\xi-t)}d\omega d\xi$$
$$= \frac{i}{2\pi}\int\int_{-\infty}^{\infty} Q_f(\xi)\frac{\rho_2}{\rho_1}\frac{c_2\sin(k_2L_2)}{\cos(k_2L_2)}\mathrm{e}^{i\omega(\xi-t)}d\omega d\xi - \frac{\mathcal{A}_2Q|Q|}{2\sigma^2\mathcal{A}_\sigma^2}. \tag{9.16}$$

In the rest of this chapter we show numerical predictions similar to those in Chapter 8 in order to obtain nonlinear results for the Limousine burner.

9.3 Thermo-acoustic Fant equation predictions for the Limousine burner

We present numerical predictions for burner Configuration II, having the parameters shown in Table 9.1. The value for the blockage length $\bar{\ell}$ is determined in Chapter 5. We determine the nonlinear solution of the Fant equation 9.16 using the fourth-order Runge-Kutta method described in Section 8.2. The convective time delay $\tau_2 = X_2/U_o \approx 10.5$ ms and power $\Pi = \Pi_{max}$ are known and fixed in this configuration; however, the dynamic time delay τ_1 is unknown and so we try two. Figures 9.2

Table 9.1: Limousine combustor (Configuration II) parameters

Description	Value
Upstream duct cross-sectional area $\mathcal{A}_1$	0.011 m^2
Downstream duct cross-sectional area $\mathcal{A}_2$	0.006 m^2
Steady upstream source volume velocity $\bar{Q}_o$	0.012 m^3/s
Constriction cross-sectional area $\mathcal{A}_\sigma$	0.0007 m^2
Distance from flame-holder edge to duct entrance L_1	0.322 m
Distance from flame-holder edge to effective duct exit $\bar{L}_2$	1.142 m
Effective length of burner 'blockage' $\bar{\ell}$	0.138 m
Upstream mean temperature T_1	288 K
Downstream mean temperature T_2	1200 K
Upstream mean density ρ_1	1.214 kg/m^3
Downstream mean density ρ_2	0.292 kg/m^3
Maximum flame power Π_{max}	50 kW/m^3

and 9.3 depict the limit cycle oscillations for approximately two periods for Configuration II, where $\tau_1 = 6$ ms and $\tau_1 = 12$ ms, respectively. Oscillations are ~ 3.5 greater in amplitude in the smaller dynamic time delay case, compared to the larger one.

Figures 9.4 and 9.5 similarly depict the limit cycle oscillations in phase space for Configuration II, where $\tau_1 = 6$ ms and $\tau_1 = 12$ ms, respectively. In both cases, the lines are thin indicating dynamic stability. The rate of change of the oscillations is ~ 4 greater in the smaller dynamic time delay case, compared to the larger one.

Figures 9.6 and 9.7 depict the Fourier transform of the limit cycle oscillations for Configuration II where $\tau_1 = 6$ ms and $\tau_1 = 12$ ms, respectively. We observe the limit cycle frequencies vary only slightly for the two configurations; they are $f \sim 139, 277, 416$ Hz for when $\tau_1 = 6$ ms and $f \sim 135, 271, 407$ Hz when $\tau_1 = 12$ ms. In both cases, the frequencies compare very well with those obtained in the experimental configuration [37].

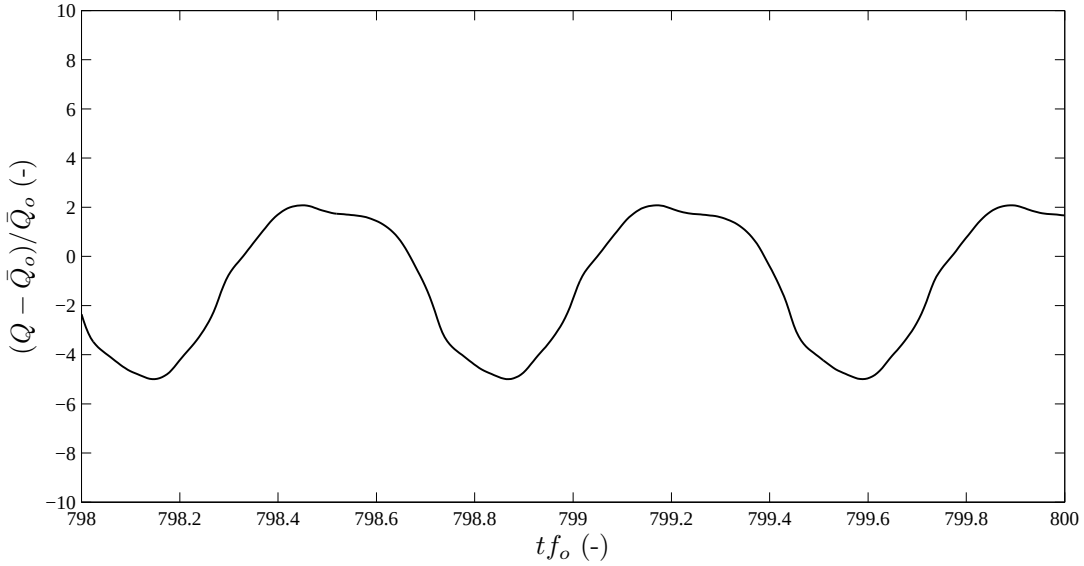

Figure 9.2: Non-dimensionalised volumetric flux plotted against non-dimensionalised time during limit cycle ($tf_o \gg 100$) for Configuration II, $\Pi = 50$ kW, $\tau_1 = 6$ ms, $\tau_2 = 10.5$ ms.

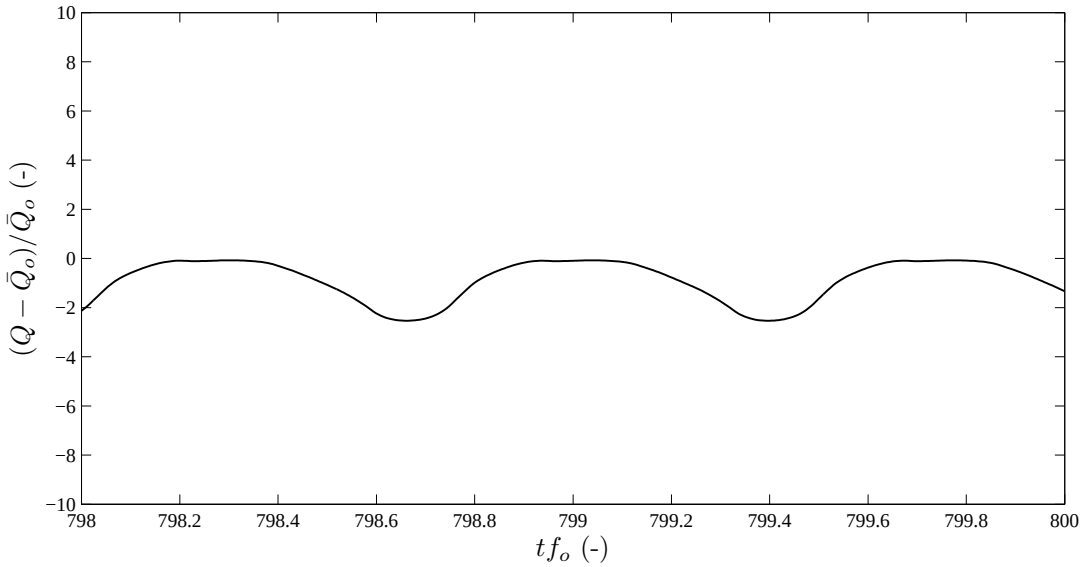

Figure 9.3: Non-dimensionalised volumetric flux plotted against non-dimensionalised time during limit cycle ($tf_o \gg 100$) for Configuration II, $\Pi = 50$ kW, $\tau_1 = 12$ ms, $\tau_2 = 10.5$ ms.

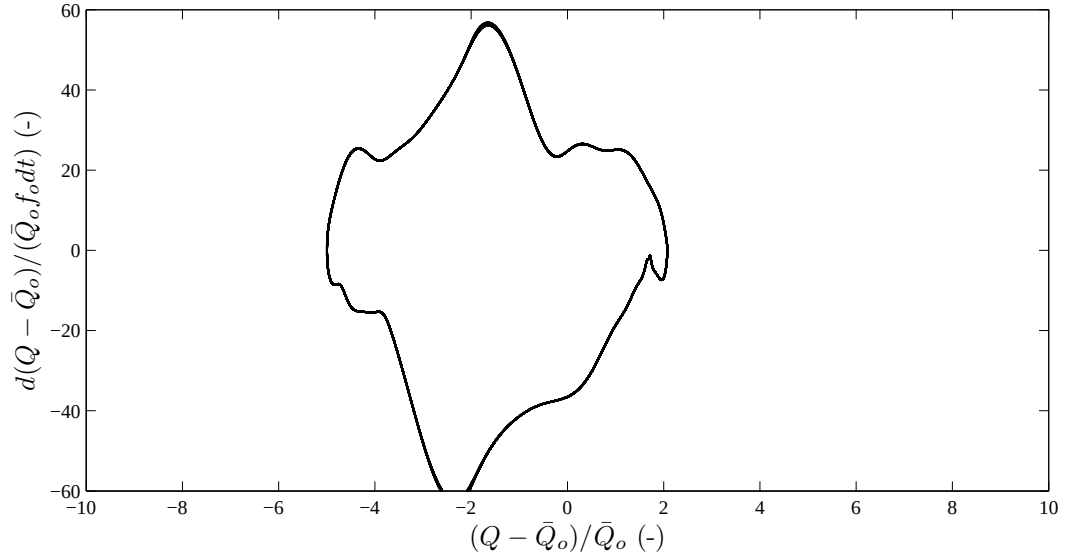

Figure 9.4: Limit cycle oscillations depicted in phase space for the non-dimensionalised volumetric flux during limit cycle ($tf_o \gg 100$) for Configuration II, $\Pi = 50$ kW, $\tau_1 = 6$ ms, $\tau_2 = 10.5$ ms.

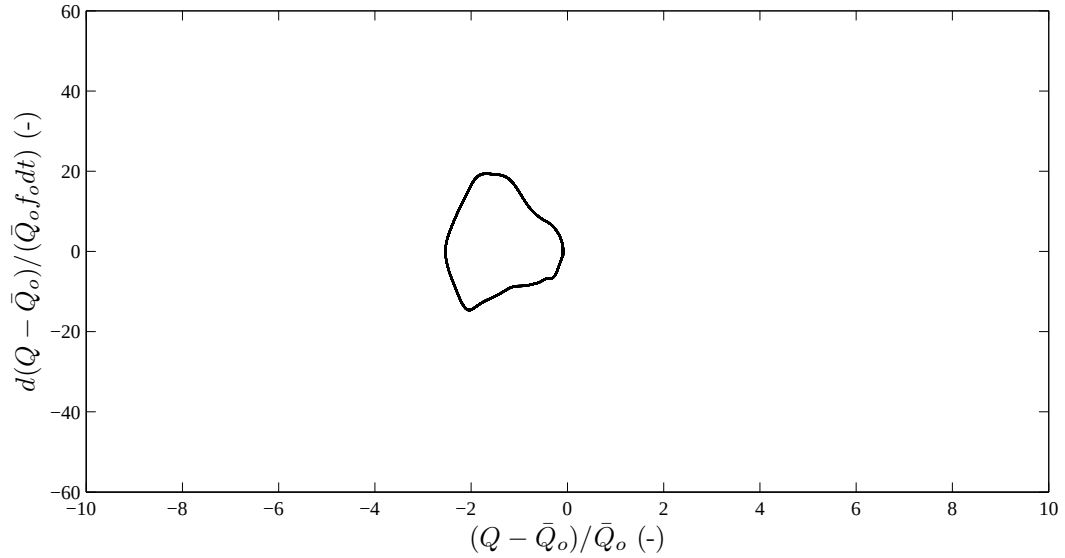

Figure 9.5: Limit cycle oscillations depicted in phase space for the non-dimensionalised volumetric flux during limit cycle ($tf_o \gg 100$) for Configuration II, $\Pi = 50$ kW, $\tau_1 = 12$ ms, $\tau_2 = 10.5$ ms.

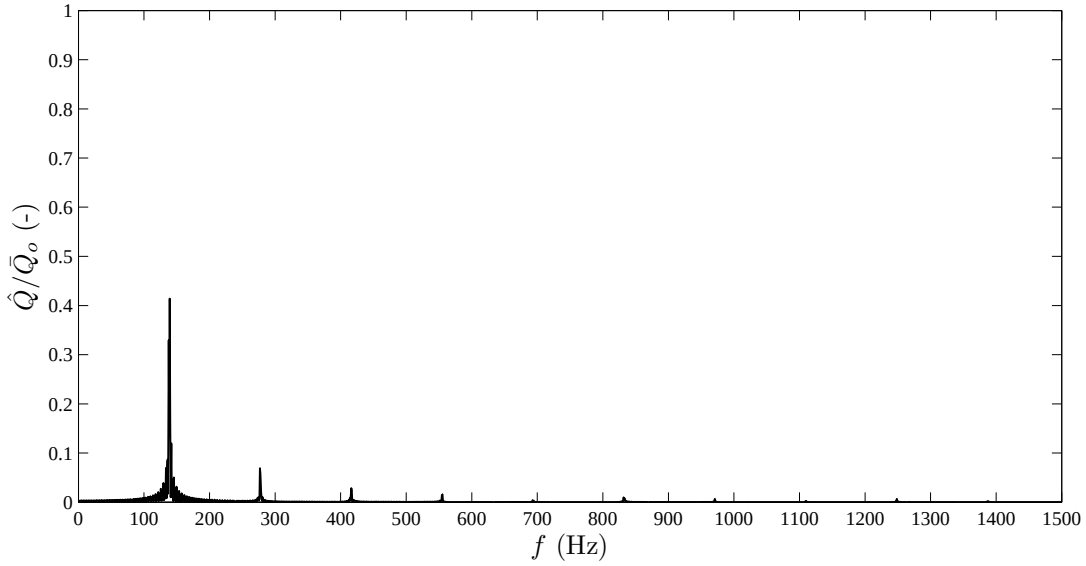

Figure 9.6: Fourier transform of the volume flux plotted against frequency during limit cycle ($tf_o \gg 100$) for Configuration II, $\Pi = 50$ kW, $\tau_1 = 6$ ms, $\tau_2 = 10.5$ ms.

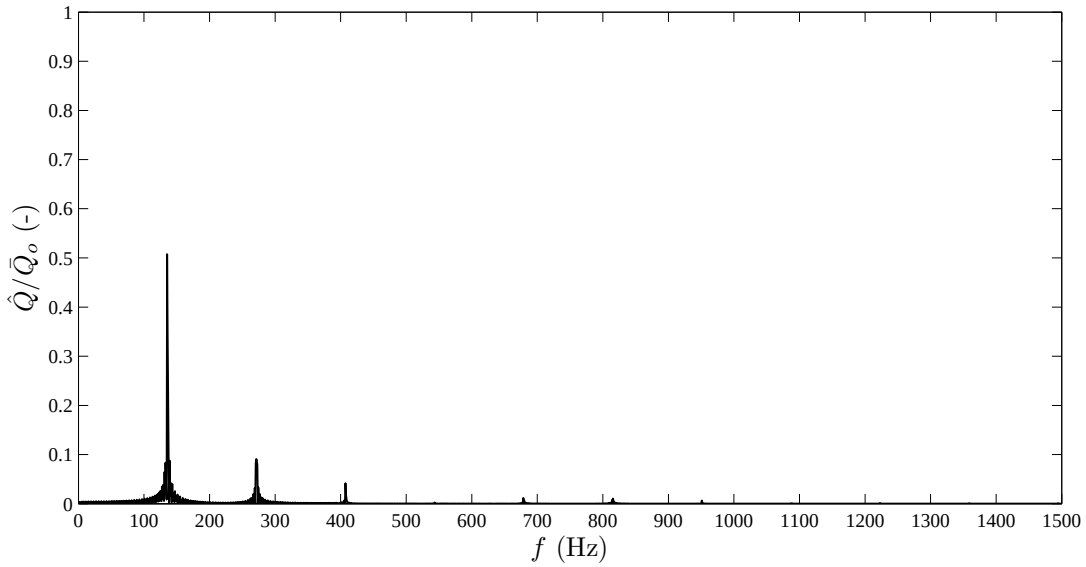

Figure 9.7: Fourier transform of the volume flux plotted against frequency during limit cycle ($tf_o \gg 100$) for Configuration II, $\Pi = 50$ kW, $\tau_1 = 12$ ms, $\tau_2 = 10.5$ ms.

Chapter 10

Conclusion

The Fant equation provides in a single equation a 'reduced complexity' representation of the instabilities of a thermo-acoustic device such as a combustor. The equation contains well defined terms that depend only on the geometry of the system, which correspond to its behaviour as a classical linear acoustic resonator. In addition, it includes nominally exact, nonlinear contributions involving spatial integrals of the thermo-aerodynamic sources, such as the flame, entropy and vortex sound sources. These integrals provide a clear indication of what must be known to obtain a proper understanding of the thermo-acoustic system, and can be evaluated to the desired level of approximation necessary to treat the problem at hand.

The equation is nonlinear and can supply limit cycle solutions for finite amplitude burner modes in terms of a specified nonlinear heat release rate of the flame. The illustrative numerical results presented are for both the linear and nonlinear equations. The linearised equation discussed in Chapter 7 governs the growth rate of the natural acoustic modes, which are excited into instability by unsteady heat release from the flame and damped by large scale vorticity production and radiation losses into the environment. Additionally, the equation supplies information about the 'forced combustion

modes' excited by the local time-delay feedback dynamics of the flame. The full nonlinear equation discussed in Chapters 8 and 9, however, governs the 'limit cycle' formation when absorption of sound by vortex shedding at trailing edges equally opposes sound generation by the flame. Alternative analysis involves modal representation of the Green's function which is discussed in Section 4.1 and cannot possibly take account of forced combustion modes nor limit-cycle formation.

The thermo-acoustic Fant equation offers a significant advance in combustion-noise predictions. A few example calculations are presented in this thesis; however, the possible applications of the equation are far greater, including arbitrary geometric and combustion configurations. The Fant equation predictions compare very well with experiment but are determined with only a fraction of the computational time required for numerical simulations. Future publications related to this work include nonlinear predictions for various combustion models and combustion-zone configurations. Although its applications are currently vast, we do not know completely the extent of the equation's application due to its inherent novelty.

References

[1] Lord Rayleigh. *The Theory of Sound*, volume 2. Dover, New York, 1945.

[2] L Crocco and S -I Cheng. *Theory of combustion instability in liquid propellant rocket motors*. Butterworths Scientific Publications, London, 1956.

[3] W C Strahle. On combustion generated noise. *Journal of Fluid Mechanics*, 49:399–414, 1971.

[4] A A Putnam. *Combustion driven oscillations in industry*. Elsevier, New York, 1971.

[5] S M Candel. *Analytical studies of some acoustic problems of jet engines*. PhD thesis, California Institute of Technology, Pasadena, 1972.

[6] M Muthukrishnan, W Strahle, and D Neale. Separation of hydrodynamic, entropy, and combustion noise in a gas turbine combustor. *AIAA Journal*, 16:320–327, 1978.

[7] W C Strahle. Combustion noise. *Progress in Energy Combustion Science*, 4:157–176, 1978.

[8] D G Crighton, A P Dowling, J E Ffowcs Williams, M Heckl, and F G Leppington. *Modern Methods in Analytical Acoustics*. Springer, London, 1992. (Lecture Notes).

[9] M S Howe. *Acoustics of Fluid-Structure Interactions*. Cambridge University Press, Cambridge, 1998.

[10] T Poinsot and D Veynante. *Theoretical and Numerical Combustion*. R.T. Edwards, Flourtown, PA, 2nd edition, 2005.

[11] C L Morfey. Amplification of aerodynamic noise by convected flow inhomogeneities. *Journal of Sound and Vibration*, 31:391–397, 1973.

[12] F E Marble. Acoustic disturbances from gas non-uniformities convected through a nozzle. In *Interagency Symposium on University Research in Transportation Noise*, Stanford, 1973. Stanford University.

[13] J E Ffowcs Williams and M S Howe. The generation of sound by density inhomogeneities in low mach number nozzle flows. *Journal of Fluid Mechanics*, 70:605–622, 1975.

[14] M S Howe. Contribution to the theory of aerodynamic sound, with application to excess jet noise and the theory of the flute. *Journal of Fluid Mechanics*, 71:625–673, 1975.

[15] F E Marble and S M Candel. Acoustic disturbances from gas non-uniformities convected through a nozzle. *Journal of Sound and Vibration*, 55:225–243, 1977.

[16] H Y Lu. An analytical model for entropy noise of subsonic nozzle flow. In *Aeroacoustics Conference*, Atlanta, 1977. AIAA.

[17] M S Bohn. Response of a subsonic nozzle to acoustic and entropy disturbances. *Journal of Sound and Vibration*, 52:283–297, 1977.

[18] N A Cumpsty and F E Marble. Core noise from gas turbine exhaust. *Journal of Sound and Vibration*, 54:297–309, 1977.

[19] N A Cumpsty and F E Marble. The interaction of entropy fluctuations with turbine blade rows; a mechanism of turbojet engine noise. *Proceedings of the Royal Society of London*, 357:323–344, 1977.

[20] A W Bloy. The pressure wave produced by the convection of temperature disturbances in high subsonic nozzle flows. *Journal of Fluid Mechanics*, 94:465–475, 1979.

[21] N A Cumpsty. Jet engine combustion noise: pressure, entropy and vorticity perturbations produced by unsteady combustion or heat addition. *Journal of Sound and Vibration*, 66:527–544, 1979.

[22] F Bake, U Michel, and I Rohle. Investigations of entropy noise in aeroengine combustors. *Journal of Engineering for Gas Turbine and Power*, 129:370–376, 2007.

[23] F Bake, C Richter, B Muhlbauer, N Kings, I Rohle, F Thiele, and B Noll. The entropy wave generator (EWG): a reference case on entropy noise. *Journal of Sound and Vibration*, 326:574–598, 2009.

[24] F Bake, N Kings, A Fischer, and I Rohle. Experimental investigation of the entropy noise mechanism in aero-engines. *International Journal of Aeroacoustics*, 8:125–141, 2009.

[25] B Muhlbauer, B Noll, and M Aigner. Numerical investigation of the fundamental mechanism for entropy noise generation in aero-engines. *Acta Acustica united with Acustica*, 95:470–478, 2009.

[26] M Leyko, F Nicoud, and T Poinsot. Comparison of direct and indirect combustion noise mechanisms in a model combustor. *AIAA Journal*, 47:2709–2716, 2009.

[27] M Leyko, F Nicoud, S Moreau, and T Poinsot. Numerical and analytical investigation of the indirect combustion noise in a nozzle. *Compres Rendus Mecanique*, 337:415–425, 2009.

[28] M S Howe. Indirect combustion noise. *Journal of Fluid Mechanics*, 659:267–288, 2010.

[29] A Pozarlik and J Kok. An analytical model for entropy noise of subsonic nozzle flow. In *International Congress on Sound and Vibration*, Cairo, 2010. IIAV.

[30] M Leyko, F Nicoud, S Moreau, and T Poinsot. Numerical and analytical modeling of entropy noise in a supersonic nozzle with a shock. *Journal of Sound and Vibration*, 330:3944–3958, 2011.

[31] A P Dowling. Nonlinear self-excited oscillations of a ducted flame. *Journal of Fluid Mechanics*, 346:271–290, 1997.

[32] A P Dowling. A kinematic model of a ducted flame. *Journal of Fluid Mechanics*, 394:51–72, 1999.

[33] A P Dowling and S R Stow. Acoustic analysis of gas turbine combustors. *Journal of Propulsion and Power*, 19:751–764, 2003.

[34] S Ducruix, T Schuller, T Durox, and S Candel. Elementary coupling and driving mechanisms. *Journal of Propulsion and Power*, 19:722–734, 2003.

[35] T Lieuwen. Modeling premixed combustion-acoustic wave interactions: a review. *Journal of Propulsion and Power*, 19:765–781, 2003.

[36] G A Richards, D L Straub, and E H Robey. Passive control of combustion dynamics in a stationary gas turbine. *Journal of Propulsion and Power*, 19:795–810, 2003.

[37] J C Ramon Casado, R Almela, and J Kok. Combustion dynamics coupled to structural vibration. In *International Congress on Sound and Vibration*, Cairo, 2010. IIAV.

[38] N Curle. The influence of solid boundaries on aerodynamic sound. *Proceedings of the Royal Society of London*, A231:505–514, 1955.

[39] W K Blake. *Mechanics of Flow-induced Sounds and Vibration*. Academic Press, New York, 1986.

[40] J Kok, S Matarazzo, and A Pozarlik. The bluff body stabilized premixed flame in an acoustically resonating tube: combustion CFD and measured pressure field. In *International Congress on Sound and Vibration*, Krakow, 2009. IIAV.

[41] P Rijke. Notiz über eine neue art, die luft in einer an beiden enden offenen röhre in schwingungen zu versetzen. *Annalen der Physik*, 107:339–343, 1859.

[42] G J Bloxsidge, A P Dowling, and PJ Langhorne. Reheat buzz: an acoustically coupled combustion instability. Part 2. Theory. *Journal of Fluid Mechanics*, 193:445–473, 1988.

[43] D -H Lee and T C Lieuwen. Premixed flame kinematics in a longitudinal acoustic field. *Journal of Propulsion and Power*, 19:837–846, 2003.

[44] M A Heckl and M S Howe. Stability analysis of the Rijke tube with a Green's function approach. *Journal of Sound and Vibration*, 305:672–688, 2007.

[45] G Fant. *Acoustic Theory of Speech Production*. Mouton, The Hague, 1960.

[46] J L Flanagan. *Speech Analysis, Synthesis and Perception*. Springer-Verlag, New York, 2nd edition, 1972.

[47] K N Stevens. *Acoustic Phonetics*. MIT Press, Cambridge, MA, 1998.

[48] M S Howe and R S McGowan. On the generalised fant equation. *Journal of Sound and Vibration*, 330:3123–3140, 2011.

[49] M S Howe and R S McGowan. Production of sound by unsteady throttling of flow into a resonant cavity with application to voiced speech. *Journal of Fluid Mechanics*, 672:428–450, 2011.

[50] M J Lighthill. On sound generated aerodynamically. Part I: General theory. *Proceedings of the Royal Society of London*, A211:564–587, 1952.

[51] G K Batchelor. *An Introduction to Fluid Dynamics*. Cambridge University Press, Cambridge, 1967.

[52] R Aris. *Vectors, Tensors, and the Basic Equations of Fluid Mechanics*. Dover, New York, 1962.

[53] P M Morse and H Feshbach. *Methods of Theoretical Physics, Part II*. McGraw-Hill, New York, 1953.

[54] Lord Rayleigh. The explanation of certain acoustic phenomena. *Nature*, 18:319–321, 1878.

[55] M S Howe. *Theory of Vortex Sound*. Cambridge University Press, Cambridge, 2003.

[56] M J Lighthill. *Waves in Fluids*. Cambridge University Press, Cambridge, 1978.

[57] A C McIntosh and S Rylands. A model of heat transfer in Rijke tube burners. *Combustion Science and Technology*, 114:273–289, 1996.

[58] B D Bellows, M K Bobba, J M Seitzman, and T Lieuwen. Nonlinear flame transfer function characteristics in a swirl-stabilized combustor. *Journal of Engineering for Gas Turbine and Power*, 129:954–961, 2007.

[59] N Peters. Laminar flamelet concepts in turbulent combustion. *Proceedings of the Combustion Institute*, 21:1231–1250, 1986.

[60] G J Bloxsidge, A P Dowling, and PJ Langhorne. Active control of reheat buzz. *AIAA Journal*, 26:783–790, 1988.

[61] P R Murray and M A Heckl. Green's function model for a rectangular Rijke burner. In *International Workshop on Non-Normal and Nonlinear Effects in Aero- and Thermoacoustics*, Munich, 2010. Technical University Munich.

[62] P R Murray and M A Heckl. Green's function model for a rectangular Rijke burner. In *International Congress on Sound and Vibration*, Cairo, 2010. IIAV.

[63] P R Murray and M S Howe. Compact Green's function for a generic Rijke burner. *International Journal on Spray Combustion Dynamics*, 3:191–208, 2011.

[64] M A Heckl. Active control from the noise of a Rijke tube. *Journal of Sound and Vibration*, 124:117–133, 1988.

[65] P M Morse and K U Ingard. *Theoretical Acoustics*. McGraw-Hill, New York, 1968.

[66] M S Howe and R S McGowan. Sound generated by aerodynamic sources near a deformable body, with application to voiced speech. *Journal of Fluid Mechanics*, 592:367–392, 2007.

[67] H Lamb. *Hydrodynamics*. Cambridge University Press, Cambridge, 1932.

[68] L M Milne-Thomson. *Theoretical Hydrodynamics*. Macmillan, London, 1968.

[69] M S Howe. *Hydrodynamics and Sound*. Cambridge University Press, Cambridge, 2007.

[70] M S Howe. *Mathematical Methods for Mechanical Sciences*. Boston University, Boston, 2003.

[71] D Howe. The application of numerical methods to the conformal transformation of polygonal boundaries. *Journal of the Institute of Mathematics and its Applications*, 12:125–136, 1973.

[72] F Dias, A R Elcrat, and L N Trefethen. Ideal jet flow in two dimensions. *Journal of Fluid Mechanics*, 185:275–288, 1987.

[73] A H Stroud and D Secrest. *Gaussian Quadrature Formulas*. Pretence-Hall, Englewood Cliffs, NJ, 1966.

[74] P K Kythe and M R Schäferkotter. *Handbook of Computational Methods for Integration*. Chapman and Hall/CRC Press, London, 2005.

[75] V I Krylov. *Approximate Calculation of Integrals*. Macmillan, London, 1962.

[76] M J D Powell. A method for minimizing a sum of squares of non-linear functions without calculating derivatives. *The Computer Journal*, 7:303–307, 1965.

[77] G Peckham. A new method for minimising a sum of squares without calculating gradients. *The Computer Journal*, 13:418–420, 1970.

[78] W H Press, B P Flannery, S A Teukolsky, and W T Vetterling. *Numerical Recipes*. Cambridge University Press, Cambridge, 1986.

[79] J H Ferziger and M Perić. *Computational Methods for Fluid Dynamics*. Springer, New York, 1999.

[80] Numerical Algorithms Group Ltd. NAG Fortran Library. January 2009, Release Mark 22.

[81] A Nijenhuis and H S Wilf. *Combinatorial Algorithms for Computers and Calculators*. Academic Press, London, 1978.

[82] P R Murray and M S Howe. On the thermo-acoustic fant equation. *Journal of Sound and Vibration*, 2012. http://dx.doi.org/10.1016/j.jsv.2012.03.014.

[83] M Abramowitz and I A Stegun. *Handbook of Mathematical Functions*. Dover, New York, 1965.

[84] J M Cohen and A Banaszuk. Factors affecting the control of unstable combustors. *Journal of Propulsion and Power*, 19:811–821, 2003.

[85] P R Murray and M S Howe. Thermo-acoustic instabilities of a generic Rijke burner. In *International Congress on Sound and Vibration*, Rio de Janeiro, 2011. IIAV.